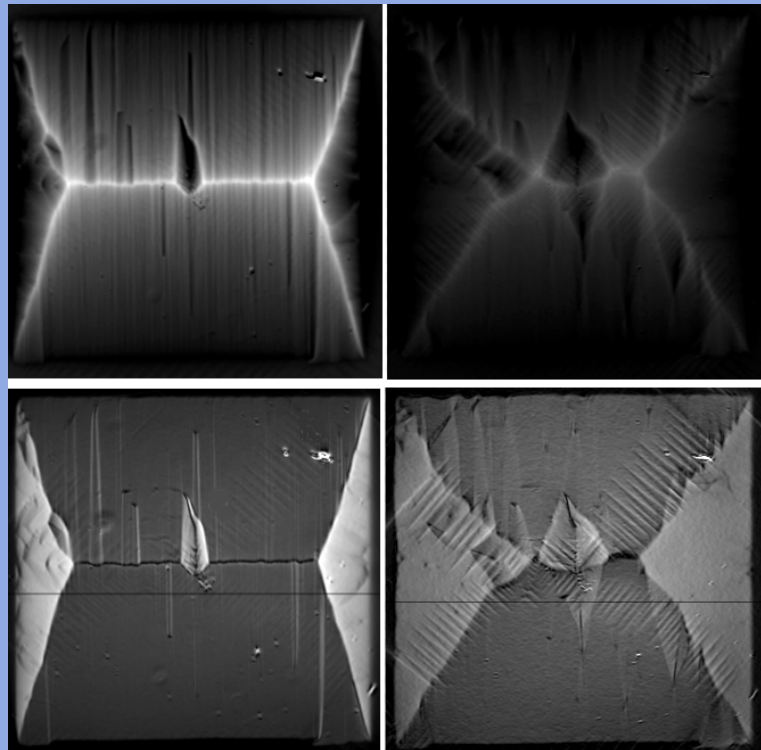**Märit Djupmyr**

The Role of Temperature for the Critical Current Density in High-Temperature Superconductors and Heterostructures

The Role of Temperature for the Critical Current Density in High-Temperature Superconductors and Heterostructures

Von der Fakultät Chemie der Universität Stuttgart zur
Erlangung der Würde eines Doktors der Naturwissenschaften
(Dr. rer. nat.) genehmigte Abhandlung

Vorgelegt von

Märit Djupmyr

aus Föllinge, Schweden

Abstract

Superconductivity and its characteristic property of zero resistance below a critical temperature T_c was discovered in 1911[1]. Through the years following since then, scientists and engineers have been striving to develop both an understanding of this phenomenon and the realization of practical applications.

Today, in the age of climate change and increasing energy costs, the interest in superconductivity is again increasing. It is important to find new solutions for energy production and to limit energy losses. This makes technical applications taking use of the special superconducting properties increasingly attractive. Products like low loss cables, highly effective motors and generators are already entering the market. Common for these is the need of superconducting materials with a high transition temperature, high critical fields and high critical currents. Since these properties are strongly connected to the prohibition of magnetic flux line motion this demands materials with optimized defect structure for flux line pinning[2]. In Fig. 1 three applications of superconductors are shown for which the control of critical currents and flux pinning properties is crucial. The first image shows a SQUID-

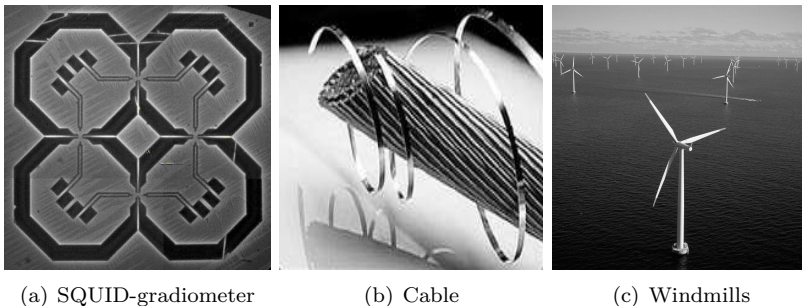(a) SQUID-gradiometer   (b) Cable   (c) Windmills

Figure 1: Possible applications of superconducting materials.

gradiometer which can be used to detect the smallest magnetic fields. To achieve the highest resolution possible, antenna structures are used in which the prohibitions of flux line motion is essential to reduce the signal-noise ratio[3]. Superconducting cables as seen in the second image have potential of playing a significant role in the future due to their ability to transport current with minimal power losses[4]. This is also important for large scale applications like superconducting motors and generators. An example is the use in superconducting windmills as depicted in Fig. 1(c). All these applications require materials with high critical temperatures and current densities. Most promising materials for the discussed applications are thin films of high temperature superconductors (HTSC) since they best fulfill the stated requirements. One promising material is YBa$_2$Cu$_3$O$_{7-\delta}$ (YBCO) which has a critical temperature of $T_c = 93$ K and as thin film can reach current densities of several 10^{11} A/m^2[5].

Although YBCO is one of the most investigated materials existing there is still missing a clear understanding of the current carrying properties which is a prerequisite for successful technological implementations. This thesis hopes to deepen the understanding of the mechanisms controlling critical currents in HTSC materials. Special emphasis will be put on the connection between microstructure, interfaces and critical currents in high-temperature superconductors.

For this purpose thin YBCO films are studied where different interfaces are produced influencing the the superconducting properties. Thereby especially the current carrying features are thoroughly investigated. By the use of different substrates on which the films are deposited, the microstructure of the superconductor can be strongly influenced. It is well known that although defects are needed as pinning centers, a too high density or too extended defects lead instead to a suppression of the critical current[6, 7]. One example for this is the appearance of growth induced grain boundaries, which strongly influence the current carrying properties and complicates the description of the current behavior. Therefore films with few inhomogeneities in the current path will be used as starting point to investigate the basic behavior of critical currents and their dependence on different pinning mechanisms.

Such YBCO thin films can be grown epitaxially on vicinal cut $SrTiO_3$ substrates with the use of Pulsed Laser Deposition (PLD). Thereby, the steps at the surface of the substrate generates a special type of homogeneous growth. These films are investigated with a quantitative magneto-optical method able to directly image the local current distribution in the films[8]. This method makes it possible to do a systematic analysis of the temperature dependence of the local critical current and to compare it to similar measurements made on films with different microstructure. The analysis of the temperature dependent critical currents presents a new method adequate of identifying pinning mechanisms. Until now mainly angular dependent measurements in high magnetic fields has been used for this purpose[7, 9]. The results of the present measurements reveal for the first time for YBCO thin films an universal description of the temperature dependence of the critical current. Different temperature regimes were identified in which different current limiting mechanisms are dominating.

By the creation of a second interface to a ferromagnetic layer further implications on the superconducting properties are expected. The ferromagnet induces magnetic pinning of the flux lines in the superconducting layer which make the system highly interesting for applications since it demonstrates a possibility to control superconducting currents via external magnetic fields. But not only new phenomena are expected to occur in the heterostructure, moreover the ferromagnetic layer can also be seen as a tool that can further help to explore the properties of the superconducting film. Comparable investigations of heterostructures of YBCO and ferromagnetic $La_{2/3}Ca_{1/3}MnO_3$ (LCMO) to the studies discussed above are presented. Thereby especially the influence of the ferromagnetic layer on the critical current is studied. Novel results are found proving that the ferromagnet influences the superconducting film through the whole thickness and not only at the interface. There is a re-

duction of the critical current for all temperatures but especially in the lower temperature regime there is a change in the temperature dependent behavior.

This work will deal with the connection between microstructure, interfaces and critical currents in YBCO thin films. Special emphasis will be put on the understanding of which pinning mechanisms might be limiting for the current transport in different temperature regimes.

With this goal in mind **Chapter 1** will give a brief introduction to superconductivity and especially to the properties of high temperature superconductors.

Chapter 2 defines the special case of superconducting thin films and deals with the special constraints geometry puts on superconducting properties.

Chapter 3 discusses the microstructure of thin films and introduces the high temperature superconductor YBCO. Further the growth processes will be described and how different substrates influence the microstructure.

In **Chapter 4** a second interface to the ferromagnet LCMO will be added to the YBCO thin film and interactions between the two competing phenomena will be discussed.

Chapter 5 describes the experimental methods, concentrating on the quantitative magneto-optical method, including explanation of the underlaying effect, setup and image processing.

In **Chapter 6** the results from magneto-optical measurements on a vicinal YBCO thin film will be presented. The main result will be the temperature dependent measurement of the critical current density distribution.

This is followed by **Chapter 7** which contains the results from a comparable study of the YBCO/LCMO bilayer. The strong influence of the ferromagnet on the superconducting film will be clearly seen.

Finally in **Chapter 8** the results will be discussed and comparisons made with films of different microstructure. An universal model will be developed explaining the temperature dependence of the local critical currents and the influence of the ferromagnetic layer will be discussed.

Zusammenfassung

Die Supraleitung mit der charakteristischen Eigenschaft eines verschwindenden elektrischen Widerstands unterhalb der Übergangstemperatur T_c wurde im Jahre 1911 entdeckt. Seitdem waren Forscher und Ingenieure bestrebt dieses Phänomen zu verstehen und praktische Anwendungen zu realisieren.

Heute, im Zeitalter des Klimawandels und steigender Energiepreise, nimmt das Interesse an Supraleitung erneut zu. Neue Lösungen zur Gewinnung von Energie und zur Verringerung von unnötigen Verlusten müssen gefunden werden. Dies macht technische Anwendungen, welche sich die supraleitenden Eigenschaften zunutze machen, zunehmend attraktiver. Produkte wie verlustarme Kabel, hocheffektive Motoren und Generatoren kommen bereits auf den Markt. Gemeinsam ist diesen Produkten die Notwendigkeit supraleitende Materialien zu nutzen die eine hohe Übergangstemperatur und hohe kritische Ströme vereinbaren. Da diese Eigenschaften mit der Verankerung von magnetischen Flusslinien fest verbunden sind, werden Materialien benötigt welche eine für die Flusslinienverankerung optimierte Defektstruktur besitzen.

Mögliche Materialen für oben genannte Anwendungen sind dünne Filme von Hochtemperatursupraleitern (HTSL), da diese die nötigen Anforderungen am besten erfüllen. Eines der vielversprechendsten Materialien ist $YBa_2Cu_3CO_{7-\delta}$ (YBCO) mit einer Übergangstemperatur T_c von 93 K welches als dünner Film Stromdichten von mehreren 10^{11} A/m^2 erreichen kann.

Obwohl YBCO eines der am intensivsten untersuchten Materialien überhaupt ist, fehlt immer noch ein klares Verständnis der stromtragenden Eigenschaften, was eine Voraussetzung für die erfolgreiche Anwendung ist. Diese Arbeit wurde in der Hoffnung geschrieben dieses Verständnis zu vertiefen. Betont wird hierbei der Zusammenhang zwischen Mikrostruktur, Grenzflächen und kritischen Strömen in Hochtemperatursupraleitern.

Zwei Ansätze zur Untersuchung der kritischen Ströme wurden verfolgt: Als erstes wurde ein ausgewähltes Substrat verwendet welches die Mikrostruktur der Ströme stark beeinflusst. Im nächsten Ansatz wurde eine zweite Grenzfläche zu einem Ferromagneten hinzugefügt welche weiteren Einfluss auf die supraleitenden Eigenschaften hat.

Optimal dotierte YBCO Dünnfilme wurden epitaktisch auf sogenannte vizinale SrTiO$_3$-Oberflächen aufgewachsen. Solche Filme zeichnen sich durch eine besonders wohldefinierte Mikrostruktur aus. Dies macht die vizinalen Filme zu einem idealen Modellsystem um das komplexe Verhalten der kritischen Ströme in Hochtemperatursupraleitern zu untersuchen. Die spezielle Stufen- und Terassenstruktur des vizinalen Substrates führt zu YBCO-Filmen welche entlang und quer zu den Stufen die Strompfade komplett unterschiedliche Mikrostrukturen besitzen. Entlang der Stufen des Substrats bildet der Film einen fast defektfreien Strompfad. Zwischen den Stufen bildet sich eine Ansammlung von ausgedehnten planaren Defekten welche Antiphasengrenzen genannt werden, und den Stromfluss stark stören. Um Zugang zum örtlichen Zusammenhang zwischen Defektstruktur und kritischer Stromdichte zu erhalten wird eine magnetooptische Methode verwendet, welche die direkte Abbildung der magnetischen Fluss- und Stromdichteverteilung ermöglicht. Die

Magnetooptik ist die Methode der Wahl da sie diese Größen sowohl lokal als auch quantitativ in kurzer Zeit zur Verfügung stellen kann.

Eine detaillierte Analyse der Temperaturabhängigkeit der lokalen kritischen Ströme zeigt dass eine gemeinsame Beschreibung für dünne YBCO Filme mit unterschiedlicher Mikrostruktur möglich ist. Die Stromdichte kann für alle Filme durch ein Potenzgesetz der reduzierten Temperatur beschrieben werden.

$$j_c(T) = j_c(0)(1 - \frac{T}{T_c})^s.$$ (1)

Dabei ist der Exponent s direkt abhängig von der Mikrostruktur und vom jeweiligen Temperaturbereich. Durch die systematische Analyse des longitudinalen kritischen Stroms, welcher entlang der Stufen des vizinalen Films fließt, war es möglich drei verschiedene Temperaturbereiche auszumachen in welchen der maximale kritische Strom von unterschiedlichen Verankerungsmechanismen begrenzt wird.

1. Der Bereich in welchem Quantenkriechen auftritt (QC), bei Temperaturen von bis zu $T = 15$ K.

2. Der Flusslinienkernverankerungsbereich (FLCP) für Temperaturen von $T = 15$ K bis zu einer Übergangstemperatur um $T = 40$ K.

3. Der Bereich der thermisch aktivierten Entankerung (TAD) für Temperaturen überhalb der Übergangstemperatur von $T = 40$ K.

Dieses Ergebnis wurde mit Messungen der temperaturabhängigen kritischen Ströme mit unterschiedlicher Mikrostruktur verglichen, dies zeigt die universelle Gültigkeit des Modells. Während über $T = 40$ K sämtliche Filme dieselbe Temperaturabhängigkeit zeigten konnte unterhalb dieser Temperatur eine starke Abhängigkeit des Exponenten s beobachtet werden. Im Bereich der FLCP wurde eine systematische Zunahme von s mit zunehmender Granularität des Films beobachtet.

Die universelle Beschreibung der kritischen Ströme in dünnen Filmen von YBCO ermöglicht eine Erweiterung der Untersuchungen auf kompliziertere Systeme. Der vizinale Film mit seiner wohldefinierten Mikrostruktur ist die ideale Grundlage für das Hinzufügen einer zweiten Grenzfläche zu einem Ferromagneten. Durch das Aufwachsen einer Schicht aus $La_{2/3}Ca_{1/3}MnO_3$ (LCMO) auf einen vizinalen dünnen Film aus YBCO wurde eine Supraleiter/Ferromagnet Heterostruktur hergestellt. In der entstehenden Doppelschicht wird keine Änderung der Mikrostruktur des supraleitenden Films erwartet.

Der starke Einfluss des Ferromagneten auf die supraleitenden Eigenschaften äußerte sich sowohl in einem verminderten kritischen Strom als auch einer kleineren Übergangstemperatur. Zudem wurde eine erhöhte Anisotropie der Ströme, welche in vizinalen Filmen auftreten, festgestellt. Dies zeigt den unterschiedlichen Einfluss des Ferromagneten auf die jeweilige Stromrichtung.

Eine Analyse der Temperaturabhängigkeit der longitudinalen kritischen Ströme in der Doppelschicht zeigte dass dieselbe Abhängigkeit wie in einer YBCO Einfachschicht besteht. Über $T = 40$ K wurde keine Änderung in der Temperaturabhängigkeit beobachtet. Dies bedeutet dass bei allen untersuchten Filmen, sowohl bei denen mit unterschiedlicher Mikrostruktur als auch

bei denjenigen mit einer zusätzlichen ferromagnetischen Schicht, die Ströme durch die thermisch aktivierte Entankerung der Flusslinien begrenzt sind. Das Verhalten im FLCP-Bereich unter $T = 40$ K unterscheidet sich davon stark. Hier wurde ein starker Einfluss des Ferromagneten auf die Temperaturabhängigkeit von j_c festgestellt. Dies führte zu einem größeren Exponenten s, dieser war vergleichbar zu den bei granularen YBCO Einfachschichten gefundenen Werten. Dies konnte durch das Eindringen von inhomogenen Streufeldern vom Ferromagneten in die YBCO-Schicht erklärt werden. Dieses Streufeld hat ähnliche Konsequenzen auf den Stromfluss wie strukturelle Inhomogenitäten. Zusätzlich konnte gezeigt werden dass die gesamte Dicke des supraleitenden Films und nicht nur die Grenzfläche beeinflusst wird.

Die Temperaturabhängigkeit des transversalen Stroms, welcher über die Antiphasengrenzen (APBs) im vizinalen Film fließt, wurde genauso detailliert analysiert. Die Temperaturabhängigkeit unterschied sich hierbei komplett von der longitudinalen Stromdichte $j_{c,L}$. Dabei war die Verwendung einer Ambegaokar-Baratoff-Funktion mit unterdrücktem Ordnungsparameter zur Beschreibung von sowohl des vizinalen YBCO Films und der Doppelschicht möglich. In diesem Modell wurden die APBs als Josephson-Kontakte mit unterdrücktem Ordnungsparameter beschrieben.

Im weiteren wurde festgestellt dass der transversale kritische Strom durch den Ferromagneten um einen Faktor 7 unterdrückt wurde. Diese Unterdrückung ist ungefähr doppelt so stark verglichen mit der des longitudinalen Stroms. Dies konnte mit der starken Magnetfeldabhängigkeit des Tunnelstroms erklärt werden, dabei wurde eine Josephson-Kopplung über die Antiphasengrenzen hinweg angenommen.

Der supraleitende dünne Film mit zwei Stromrichtungen mit unterschiedlicher aber wohldefinierter Mikrostruktur und zusätzlich das Hinzufügen der Grenzfläche zu einem Ferromagneten machten es möglich und waren notwendig um zu einem tieferen Verständnis der Mechanismen welche die kritischen Ströme in dünnen YBCO Filmen begrenzen zu gelangen.

In der YBCO Einfachschicht war es notwendig eine neue anisotrope Abrikosov Flusslinie mit verlängertem normalleitendem Kern einzuführen um die Abhängigkeit von $j_c(T)$ von der Granularität des Films zu erklären. Es wird erwartet dass sich diese anisotropen Abrikosov Flusslinien auf den Kleinwinkelkorngrenzen befinden. Mit größeren Fehlorientierungswinkeln wird die Anisotropie größer. Dies führt zu einer reduzierten Verankerungskraft welche direkt die beobachtete Unterdrückung des kritischen Stroms bedingt.

In der Doppelschicht wird erwartet dass die Domänenstruktur des Ferromagneten zu einer spontanen Entstehung von Flusslinien im Supraleiter führt. Da die Magnetisierung von LCMO hauptsächlich parallel zur Schichtebene liegt wird erwartet dass sich die Flusslinien nur an den Domänengrenzen befinden. Diese Domänengrenzen trennen Domänen unterschiedlicher Orientierung der Magnetisierung. Es wird erwartet dass nur entlang der Domänengrenzen eine Komponente der Magnetisierung senkrecht zur Schichtebene vorhanden ist. Dies führt zu einer Flusslinienverteilung welche ähnlich zu der einer Korngrenze ist. Das ähnliche Verhalten welches für Filme mit granularer Mikrostruktur und Doppelschichten festgestellt wurde kann mit einer

magnetischen Körnung in der Doppelschicht beschrieben werden.

Die Antiphasengrenzen in der Einfachschicht konnten als Tunnelkontakte mit reduziertem Ordnungsparameter beschrieben werden. Durch das Hinzufügen der ferromagnetischen Schicht konnte dieses Modell nochmals bestätigt werden. Der Strom welcher über Antiphasengrenzen hinweg fließt konnte als ein Strom welcher durch Regionen mit reduzierter Supraleitung fliesst welche supraleitende Inseln trennen beschrieben werden. Die Antiphasengrenzen können als bestehend aus supraleitenden und nichtsupraleitenden Regionen beschrieben werden. Dies führt zu komplexen Tunnelkontakten welche lokal als Josephson-Kontakte oder SQUID-ähnliche Strukturen beschrieben werden können. Diese Beschreibung verbindet die in Messungen gleichzeitig beobachteten Tunneleigenschaften und die gemessenen hohen kritischen Ströme.

Die detaillierte Analyse der lokalen kritischen Ströme in dünnen YBCO Filmen und Heterostrukturen zeigt dass es möglich ist die stromführenden Eigenschaften durch die Veränderung der Grenzflächen zu kontrollieren. Der enge Zusammenhang zwischen Mikrostruktur, Grenzfläche und kritischen Strömen wurde für dünne Filme von YBCO bewiesen. Durch eine gezielte Auswahl des Substrats ist es möglich die Mikrostruktur in Bezug auf die Erhöhung der kritischen Ströme zu verändern. Zusätzlich zeigt das Hinzufügen einer ferromagnetischen Schicht die Möglichkeit auf die kritischen Ströme von außen mittels Anlegen eines magnetischen Feldes zu kontrollieren.

Diese Ergebnisse stellen einen wichtigen Beitrag zum Verständnis der strombegrenzenden Mechanismen in dünnen Schichten von HTSL dar. Dies ist ein wichtiger Schritt in Richtung der industriellen Verwendung dieser Materialien in verschiedensten hochentwickelten Lösungen.

Contents

Chapter 1

Superconductivity

1.1 The Superconducting State

The phenomenon of superconductivity is characterized by two properties, zero DC resistivity and perfect diamagnetism. These two properties are only found after cooling the material below a critical temperature T_c, where the material undergoes a phase transition into the superconducting state. The drop to zero resistivity was first observed by H. Kammerling-Onnes[1] in mercury in 1911 and he called the phenomenon superconductivity. After that many more metals and alloys have been found to be superconducting among others the ceramic $YBa_2Cu_3O_{7-\delta}$[5].

The expulsion of magnetic flux from the interior of the superconductor was discovered by W. Meissner and R. Ochsenfeld[10] in 1933 and is referred to as the Meissner effect. The combination of zero resistance and perfect diamagnetism makes the superconducting state distinctive from what a perfect conductor would be. The transition into the superconducting state is a real thermodynamic phase transition. It is defined by independent thermodynamical variables, temperature T and magnetic field H and is independent of history, which is not true for a perfect conductor. Superconductivity can not persist at an arbitrarily high magnetic field. At a critical field $B_c(T)$ the Meissner state and with it the superconductivity is destroyed, see the phase diagram in Fig. 1.1.

1.2 London Theory

The first theory developed by F. London and H. London[11] is describing the superconducting state in a quantitative way including both the perfect
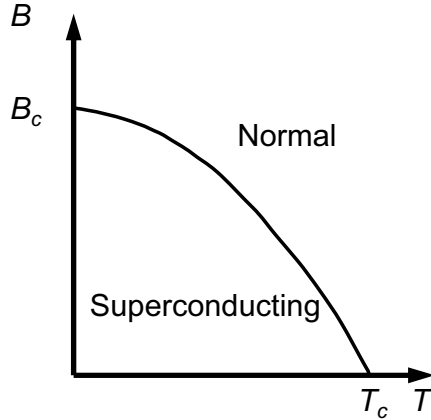
Figure 1.1: Phase diagram of a superconductor.

conductivity and the Meissner effect. For a perfect conductor the electrons will be accelerated without dissipation and the current density carried by these electrons can thus be written as,

$$\frac{\partial \mathbf{j}_s}{\partial t} = \frac{n_s e_s^2}{m_s} \mathbf{E},$$ (1.1)

This is the 1. London equation that relates the superconducting current to the electric field $\mathbf{E}$ with n_s, the density of superconducting electrons and e_s, m_s the charge and mass of was later found to be the paired superconducting electrons.

The 2. London equation is derived by using Eq. (1.1) together with the Maxwell equation $\nabla \times \mathbf{B} = \mu_0 \mathbf{j}$ and it relates the supercurrent to the magnetic field B,

$$\nabla \times \mathbf{j}_s = -\frac{n_s e_s^2}{m_s} \mathbf{B}.$$ (1.2)

and is thus containing a description of the perfect diamagnet.

The London equations together with the Maxwell equation directly give that

$$\nabla \times (\nabla \times \mathbf{B}) = \frac{\mu_0 n_s e_s^2}{m_s} \mathbf{B}.$$ (1.3)

These equations predict that the currents only can flow within a thin layer at the surface of the superconductor and that the same is true for the pene-

tration of the magnetic field. The thickness of this layer is called the London penetration depth λ_L and is given by

$$\lambda_L = \sqrt{\frac{m_s}{\mu_0 n_s e_s^2}}. \tag{1.4}$$

It is the first important characteristic length for describing a superconductor.

1.3 Ginzburg-Landau Theory

The theory of superconductivity developed by Ginzburg and Landau[12] in 1950 describes also the phenomenological properties. It contains the London theory but as new element also includes a variation of the density of superconducting electrons n_s in space. A complex wave function Ψ was introduced such that $n_s = |\Psi|^2$. In the Landau theory of second order phase transitions Ψ could now be used as order parameter and the Gibbs free energy G be written as a series expansion of Ψ,

$$G = G_n + \alpha|\Psi|^2 + \frac{1}{2}\beta|\Psi|^4 + \frac{1}{2m_s}|(-i\hbar\nabla - 2e\mathbf{A})\Psi|^2 + \frac{1}{2\mu_0}|\mathbf{B} - \mu_0\mathbf{H}_{ext}|^2. \tag{1.5}$$

Minimizing Eq. (1.5) with respect to Ψ and $\mathbf{A}$ results in the Ginzburg-Landau equations,

$$\alpha\Psi + \beta|\Psi|^2\Psi + \frac{1}{2m_s}(-i\hbar\nabla - 2e\mathbf{A})^2\Psi = 0. \tag{1.6}$$

and

$$\mathbf{j} = \frac{i\hbar e}{m_s}(\Psi^*\nabla\Psi - \Psi\nabla\Psi^*) - \frac{4e^2}{m_s}|\Psi|^2\mathbf{A} \tag{1.7}$$

The first equation, similar to the Schrödinger equation describes the variation of the order parameter Ψ on the magnetic field, while the second equation defines the supercurrent $\mathbf{j}$.

The Ginzburg-Landau theory can treat features not included in the London theory for example a spatially varying n_s. Also a new characteristic length is introduced, the coherence length ξ which describes the distance over which $\Psi(\mathbf{r})$ can vary,

$$\xi(T) = \frac{\hbar}{|2m_s\alpha(T)|^{1/2}} = \left(\frac{\hbar^2}{2m_s aT_c}\right)^{1/2}\left(1 - \frac{T}{T_c}\right)^{-1/2}. \tag{1.8}$$

The GL penetration depth λ specifies how far a magnetic field can penetrate into the superconductor.

$$\lambda(T) = \left(\frac{m_s}{4\mu_0 e^2 |\Psi|^2} \right)^{1/2} = \left(\frac{m_s \beta}{4\mu_0 e^2 a T_c} \right)^{1/2} \left(1 - \frac{T}{T_c} \right)^{-1/2}. \qquad (1.9)$$

Since these two lengths both have the same temperature dependence, it is possible to define a temperature independent parameter by dividing the two. This ratio is called the GL parameter,

$$\kappa = \frac{\lambda}{\xi}. \qquad (1.10)$$

For type-I superconductors, $\kappa << 1$ and the behavior is that of a perfect diamagnet. But at $\kappa = 1/\sqrt{2}$ this behavior changes qualitatively, the wall energy becomes negative which leads to a subdivision into superconducting and normal domains that continues until it is limited by the microscopic length ξ. These kind of superconductors are called Type II. They are in the Meissner state up to a lower critical field H_{c1}. Above H_{c1} the magnetic field starts to penetrate into the superconductor in form of flux lines. Each flux line is carrying an elementary flux quantum $\Phi_0 = \frac{h}{2e} = 2.07 \times 10^{-15}$ Tm^2. This phase is called the Shubnikov phase and exists up to a upper critical field H_{c2}, where the superconductor is completely filled with magnetic flux lines and the superconductivity breaks down. The phase diagram for a type II superconductor looks like in Fig. 4.2.
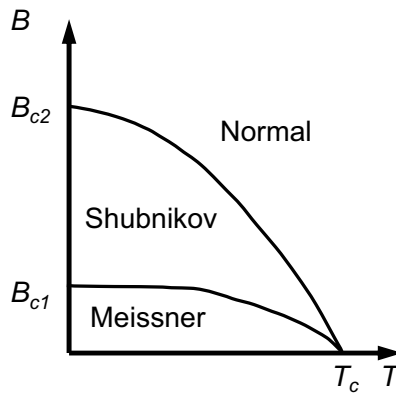

Figure 1.2: Phase diagram of a Type II superconductor.

1.4 BCS Theory

A microscopic theory for superconductors was presented in 1957 by Bardeen, Cooper and Schrieffer[13, 14] and is known as the BCS theory. It explains the absent resistivity in the superconductor with the formation of electron pairs. These are called Cooper-pairs and are formed by electron-phonon interaction[15] between two electrons with opposite spin and momentum. A sketch of how this interaction can work is seen in Fig. 1.3. An electron attracts ions of the crystal resulting in a region of net positive charge. This works as an attractive force on a second electron and results in a coupling of the two electrons with an binding energy of 2Δ.
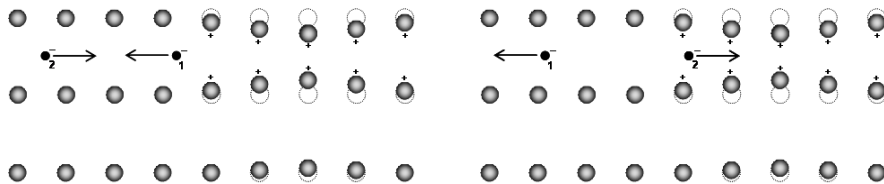

Figure 1.3: Formation of Cooper pairs

Opposite to single electrons that are fermions, the Cooper-pairs are bosons which all can condensate into the same ground state. This results in an energy gap $E_g = 2\Delta$ in the density of states close to the Fermi energy. Electrical resistance arises from inelastic collisions of charge carriers, where they are scattered into empty states slightly above the Fermi level. This results in dissipation of energy. Since in superconductors there are no empty states close to the Fermi level due to the presence of the energy gap, the absence of resistivity can be understood.

However, for large current densities, the kinetic energy of the charge carriers can become large enough, that they through a collision can overcome the energy gap and through inelastic scattering move into an empty state. It is not possible to describe this process looking at the single electrons, but instead the system need to be described as a many particle system, where the jump over the energy gap is described by the first quasiparticle excitation. The energy needed for excitation of the quasiparticles is connected to their kinetic energy ξ_k by,

$$E(\xi_k) = \sqrt{\xi_k^2 + \Delta^2}. \tag{1.11}$$

The minimum of energy needed to destroy the coherence of the superconducting condensate is given by $E = \Delta$ where $\xi_k = 0$.

When the kinetic energy of the supercurrent is overcoming this energy the superconductivity is destroyed. This maximal current is thus called the depairing current and is given by

$$j_0 = 2en_s\sqrt{\frac{2\Delta}{m_s}}, \tag{1.12}$$

n_s the density and m_s the mass of the Cooper pairs. This is the upper limit for the critical current in the superconductor. Using Ginzburg Landau theory it is possible to rewrite this expression as,

$$j_0 = \frac{1}{3\sqrt{2}}\frac{\phi_0}{\pi\mu_0\xi_{ab}\lambda_{ab^2}}. \tag{1.13}$$

1.5 High Temperature Superconductors

In 1986 a new class of materials was discovered that exhibit much higher T_c than conventional superconductors[16]. These are called high temperature superconductors(HTSC), all of them are type II superconductors. Many of the HTSC are cuprates, like for example $YBa_2Cu_3O_{7-\delta}$ with a $T_c = 93$ K[5].

Superconducting current carriers are also for this group of superconductors Cooper pairs. But the pairing mechanisms and the explanation of the high transition temperatures are still in debate. Due to the large energy gap in HTSC (for YBCO $\Delta E = 18 - 22$ meV)[17] the classical electron-phonon interaction cannot explain the pairing. There are theoretical models suggesting strong electron correlation, polaron and bipolaron interaction or an modified BCS mechanism[18, 19]. Here only one of these theories will be discussed in a bit more detail, where he pairing mechanism is due to quantum mechanical exchange interaction[20].

The idea is that there is an antiferromagnetic coupling between the charge carriers, since both superconductivity and antiferromagnetism can be described by a pairing of anti-parallel oriented spins. The correlation between the charge carriers is taking place through quantum mechanical exchange interaction where correlated pairing leads to a lowering in energy.

The mechanism is sketched in Fig. 1.4. It is displayed how holes are moving through the spin lattice. The holes can be parts of the Cooper pairs as is the case for hole conductors like YBCO.

A single hole that is moving would lead to adjacent spins that are parallel and thus frustrated. Since this would result in an increase in energy a single moving hole can be dismissed. For paired holes moving together,
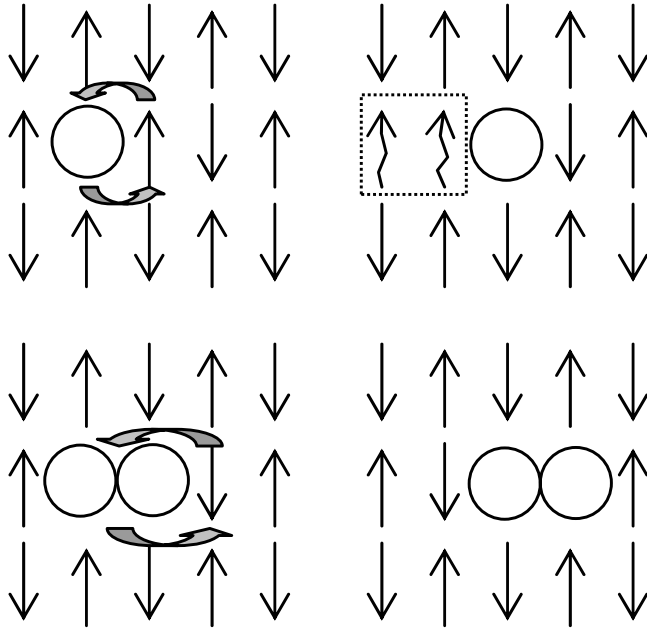
Figure 1.4: Cooper pair formation through quantum mechanical exchange interaction. A single hole moving through the antiparallel spin lattice lead to an excited spin configuration (upper images). Two paired holes can move freely through the antiparallel spin lattice (lower images).

the situation is different, neighboring spins are always kept antiparallel. In this way there is no change in energy and the paired holes can move freely through the crystal lattice. Single holes are not attached to a single atom, but there is an enhanced probability that they will be found close to the ions. The density of charge carriers is strongly dependent on the oxygen doping. For low oxygen doping the charge carriers will stay localized and the system will be ferromagnetic. With increasing oxygen doping the charge carrier density will increase. This reduces the magnetic ordering and the system will become superconducting.

Symmetry of the Order Parameter

The difference in symmetry of the order parameter Ψ is a further distinctive difference between HTSC and conventional superconductors. The order parameter has symmetry properties that depend on the structure of the ma-
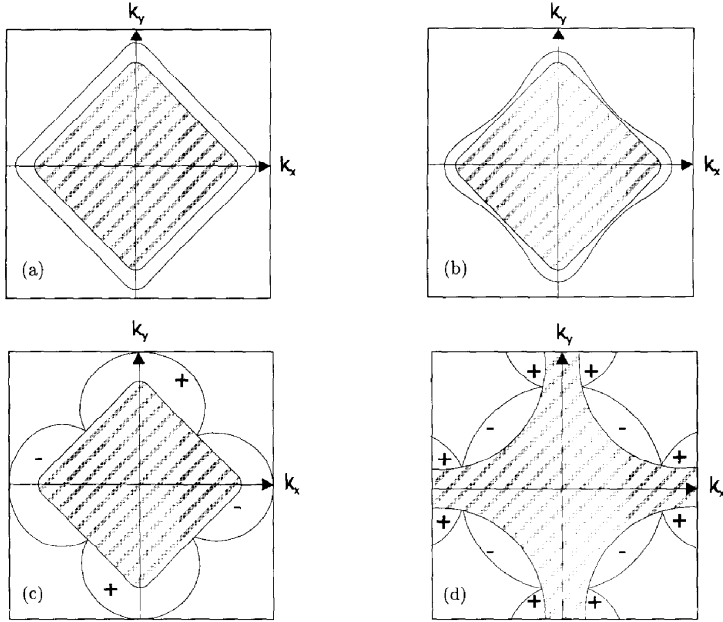
Figure 1.5: Schematically sketch of some possible symmetries of the energy gap in HTSC. a) isotropic s-wave symmetry, b) anisotropic s-wave symmetry, c) $d_{x^2-y^2}$ symmetry and d) extended s-wave symmetry. From D. J. Scalapino, Phys. Rep. 250, 329 (1995)

terial and the bosonian character of the Cooper pairs. The Cooper pairs are in a spin singlet state with $S = 1$ due to their antiparallel oriented spins. This together with the even wave function found for bosons, the angular momentum of the Cooper pairs must also be even, $L = 0, 2, 4, \ldots$. A momentum of $L = 0$ is called s-wave symmetry and $L = 2$ d-wave symmetry. Conventional superconductors are showing s-wave symmetry because the energy gap is in k-space isotropic in all directions which also means that the order parameter is isotropic.

In HTSC, however, the symmetry of the order parameter is still a subject of discussion. The energy gap is anisotropic which suggests knots in the order parameter[21, 22, 23]. So, in the CuO$_2$- planes a $d_{x^2-y^2}$ symmetry can be assumed[24, 23] while along the c-axis the order parameter is strongly suppressed. That is equal to an angular momentum $L = 2$ meaning d-wave symmetry. Surface sensitive measurements have shown d-wave symmetry or anisotropic s-wave symmetry of the order parameter[25], but experiments of

bulk properties yield results of s-wave symmetry. But due to the orthorhombic structure in for example YBCO no pure $d_{x^2-y^2}$ is possible. Further, also pair breaking at crystal inhomogeneities can lead to a change in symmetry wherefore HTSC probably show mixed symmetry[26].

1.6 The Flux-Line Lattice

High temperature superconductors are Type II superconductors which mean they can be in a state called the Shubnikov phase[27]. It is defined by the penetration of magnetic flux in the form of quantized flux lines. The Ginzburg-Landau theory defines two characteristic lengths which determine the superconducting properties. They are the London penetration depth λ and the coherence length ξ. In a superconductor a non-zero volume current would break the symmetry of the paired state. Thus, super-currents can only flow at the interface between superconducting and normal conducting areas. Since changes in flux density in the superconductor and corresponding shielding currents only occur on the length scale of λ, which for YBCO is little more than 100 nm, a flux free superconductor cannot be efficient for current transport. This changes drastically when the superconductor
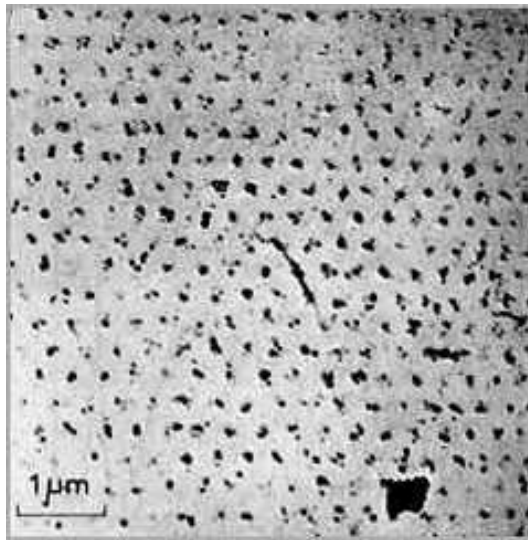

Figure 1.6: First image of a flux line lattice in $Pb-4at\%In$. The image was made by bitter decoration in 1967 by Essmann et al.[28].

enters the Shubnikov phase. In this phase, the superconductor is filled with flux lines, who usually contain a normal conducting core. Since each flux line is carrying one flux quantum Φ_0, the area between normal conducting and superconducting domains is maximized. This is the reason for the exceptionally high transport currents that can be found in these kind of materials.

Ideally, the flux lines arrange themselves in a hexagonal lattice, the Abrikosov lattice[29]. But for a current to flow it is necessary to create a gradient in the flux density. If the flux line lattice was equidistant, this would result in that all the microscopic circular currents around the flux lines would add up to zero, resulting in zero transport current. A flux gradient would instead add up to a non-vanishing current perpendicular to the gradient.

Necessary for the formation of a macroscopical transport current is also the prohibition of flux line motion. When a transport current is flowing through the superconductor there is a Lorenz force acting on the flux lines: $\mathbf{F}_L = \mathbf{j} \times \hat{n}\phi_0$, with $\hat{n}$ the vector of unity along the flux line. A moving flux line is inducing a magnetic field gradient $\dot{\mathbf{B}}$ locally in the superconductor, which lead to a non vanishing electric field through $\nabla \times \mathbf{E} = -\dot{\mathbf{B}}$. The electric field accelerates the unpaired electrons still present in the superconductor at finite temperatures, and thus gives rise to dissipation. This in turn heats the superconductor locally above the critical temperature T_c and eventually even the superconductivity can be destroyed.
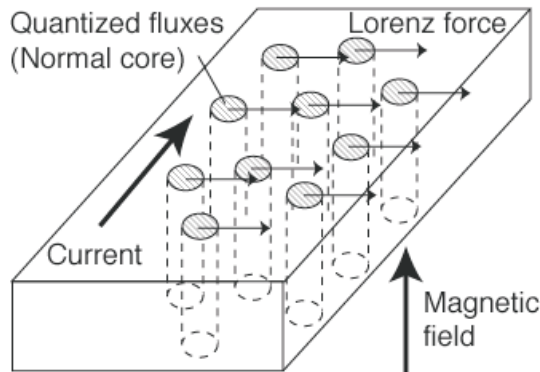

Figure 1.7: Schematic sketch of the flux line lattice.

1.7 Pinning

Structure of a Flux Line

To understand how the flux line motion can be prevented it is important
to know the structure of a flux line. Fig. 1.8 shows the distribution of the
superconducting charge carrier density for an isolated flux line, together
with the magnetic flux density. For a superconductor with $\kappa \gg 1$, one
isolated c-axis oriented flux line can be described quite accurately by ana-
lytical expressions[30]. For the order parameter the following ansatz can be
made,

$$\Psi(r) = f(r)e^{i\phi}, \tag{1.14}$$

where $f(r) = \frac{r}{\sqrt{r^2 + 2\xi_{ab}^2}}$ and ξ is the coherence length. This expression is
in excellent agreement with numerical solutions in the Ginzburg-Landau
theory. Through Eq. (1.6) and Eq. (1.7) the expressions for the magnetic
flux density and current distribution can be found. For the z-component
thus,

$$B_z(r) = \frac{\phi_0}{2\pi\lambda_{ab}^3} K_0 \left(\frac{\sqrt{r^2 + 2\xi_{ab}^2}}{\lambda_{ab}} \right). \tag{1.15}$$
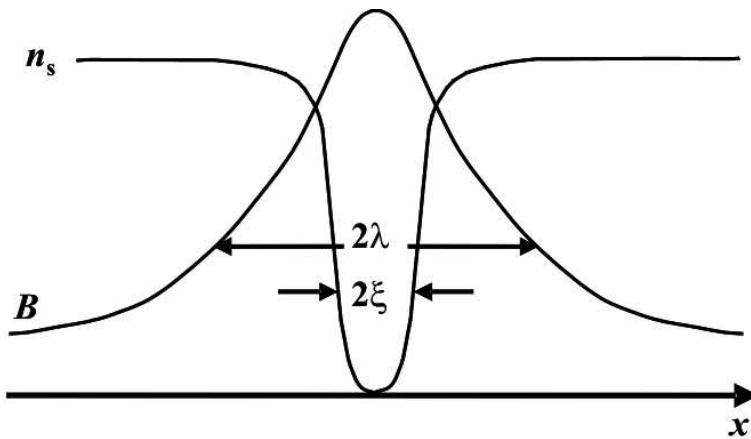

Figure 1.8: Sketch of a flux line showing the chracteristic lengths λ and ξ.

For the current distribution the circular component is,

$$j_\phi = \frac{\Phi_0}{2\pi\lambda_{ab}^3} K_1 \left(\frac{\sqrt{r^2 + 2\xi_{ab}^2}}{\lambda_{ab}} \right) \frac{r}{\sqrt{r^2 + 2\xi_{ab}^2}}. \qquad (1.16)$$

The K_i are the so called MacDonald functions in i'th order. These expressions for $n_s(r) = |\Psi|^2$ and $B_z(r)$ are consistent with those plotted in Fig. 1.8. The discussion above though is only valid for single isolated flux lines, a state that is rarely found in reality. Therefore other theories must be used.

Pinning Mechanisms

As discussed earlier, the motion of flux lines leads to dissipation and can destroy the superconducting state. And even if not enough flux lines move to destroy superconductivity the motion still can lead to unwanted noise disturbing in possible applications. It is therefore crucial to prevent this motion. This can be made by pinning centers which are for example in-homogeneities in the material where the superconducting order parameter is locally suppressed. There are many different types of defects that can act as effective pinning centers, like point defects[31], dislocations[6], grain boundaries[32] and twin planes[33]. The strength of the attractive force acting on the flux line is depending on the type of inhomogeneity and on the flux line system.

Pinning of a flux line is possible in places with spatial variation of the flux line self energy ϵ_L. The pinning energy $\epsilon_p(r)$ per unit length of the flux line is defined as the difference between the line energy at the defect $\epsilon_L(r_{def})$ and at a larger distance from the pinning center $\epsilon_L(r)$,

$$\epsilon_p(r) = \epsilon_L(r_{def}) - \epsilon_L(r). \qquad (1.17)$$

If there is a spatially varying flux line energy, the corresponding pinning force f_p is defined as the maximum of the energy gradient,

$$f_p = -(\nabla \epsilon_p)_{max}. \qquad (1.18)$$

The flux line self energy is defined inside the Ginzburg-Landau theory and by looking at its different terms the different pinning contributions can be identified.

$$\epsilon_L = \int d^2r \alpha(|\Psi|^2 - |\Psi_0|^2) + \frac{\beta}{2}(|\Psi|^4 - |\Psi_0|^4) + \frac{1}{2m^*}|\hat{\mathbf{p}}\Psi|^2 + \frac{1}{2\mu_0}\mathbf{B}^2, \quad (1.19)$$

with Ψ_0 being the order parameter in the Meissner state and $\hat{\mathbf{p}}$ the momentum operator.

The energy of a flux line can be subdivided into three parts.

- The first part defines the condensation energy of the flux line,

$$\epsilon_{L,kond} = \int d^2r \alpha(|\Psi|^2 - |\Psi_0|^2) + \frac{\beta}{2}(|\Psi|^4 - |\Psi_0|^4). \qquad (1.20)$$

  If the condensation energy varies on the length scale of the coherence length ξ, the flux line will gain energy if placed at a normal conducting defect. This leads to strong pinning especially if the defect is in the size of the flux line core.

- The second part of Eq. (1.19) describes the kinetic energy of Cooper pairs circulating around the vortex core,

$$\epsilon_{L,kin} = \int d^2r \frac{1}{2m^*}|\hat{\mathbf{p}}\Psi|^2. \qquad (1.21)$$

  The kinetic energy can also vary on the length scale of ξ and is depending on the density of superconducting charge carriers.

  This pinning mechanism is called flux-line core interaction and is of particular importance in HTSC due to the large ratio λ/ξ.

- The last term of Eq. (1.19) describes the magnetic energy ϵ_{mag} of the flux line.

$$\epsilon_{L,mag} = \int d^2r \frac{1}{2\mu_0}\mathbf{B}^2 \qquad (1.22)$$

  A variation of this contribution can be caused by defects in the crystal and takes place on the length scale of the penetration depth λ. Since for high temperature superconductors $\lambda >> \xi$ this usually give a much smaller contribution to the pinning than does the flux line core pinning.

A further contribution to flux pinning can originate from suprastrictive effects and is related to elastic interaction where the crystal defects have different elastic properties in normal and superconducting states[34, 35]. This contribution to pinning is for HTSC generally small.

The strength of the pinning force does not only depend on the type of defects but also on properties of the flux line lattice. A stiff flux line system has difficulties adjusting to the random pinning centers and is thus less strongly pinned than a soft system, that easily adjust to the pinning centers.

Random disorder and thus random forces on the flux lines disturbs or even destroys the triangular flux line lattice. Too many or too bad defects can even lead to a limitation of the critical current since the superconductivity may be suppressed in an area that the superconducting charge carriers cannot avoid.

Pinning of the Flux Line Lattice

For the electric current transport not only the size of the pinning force from individual crystal defects on single flux lines is important. Instead there is a macroscopical pinning force density, made up from many pinning centers, that act on the flux line distribution. Hence, also the elastic and plastic properties of the flux line lattice as well as thermal forces must be taken into account. As discussed in Chapter 1.6 the flux lines interact with each other to form a regular lattice. The interaction between the flux line lattice and the defect distribution leads to a deformation of the lattice. The position of the individual flux lines may deviate from the periodic Abrikosov lattice, when in order to lower its energy it choses to pass through favorable pinning sites. This leads to deformation of the lattice and increase in elastic energy. The resulting flux line configuration will be the one that minimizes the sum of the flux line energy and the elastic energy. The theory of this summation problem was developed by Larkin and Ovchinnikov[36, 37]. Further, the flux lines are not stiff but can bend to adjust themselves to a certain defect distribution.

Correlated pinning is when there are many regularly distributed defects, where there is interaction between single flux lines and defects, but also a correlated force from all the defects that is acting on the flux line lattice as whole. This is usually the case for linear or planar crystal defects[38].

If the defect structure is non-regular the macroscopic pinning force will be determined by fluctuations in the single pinning forces. The flux line lattice will need to adjust to these fluctuations. The macroscopic crystal order will then be destroyed while locally the structure of the lattice will be kept[39, 36, 37]. This can lead to bundles of flux lines moving together through the destroyed flux line lattice.

1.8   Supercurrent Tunneling

Not only depinning of flux lines can restrict the occurring current densities there might also be areas with reduced superconductivity or even normalcon-

ducting or isolating properties. Such areas lead to an suppressed depairing current, limiting the maximal current flow in the area.

When two superconductors are separated by a thin isolating barrier a supercurrent can still flow between them, see Fig. 1.9. This is due to the so called Josephson effect[40] that describes the tunneling of Cooper pairs through a thin layer of non superconducting material. In the Josephson junction a single order parameter Ψ can be used on both sides. The tunneling current at zero voltage is strongly depending on any external magnetic field, following,

$$j = j_0 \frac{\sin \pi \Phi/\Phi_0}{\pi \Phi/\Phi_0},$$ (1.23)

where Φ is the total magnetic flux in the junction and $\Phi_0 = h/2e$, the flux quantum. This is the so called dc Josephson effect. In Fig. 1.10 this function is plotted as j/j_0 showing the Fraunhofer pattern of the critical current across the junction. Applying a small magnetic field will directly lead to a strong reduction of the critical current in the film. This behavior is independent of temperature. If a voltage difference V is maintained across the junction this causes a phase difference $\pi\phi$ to evolve with time like,

$$\frac{d\Delta\phi}{dt} = \frac{2eV}{\hbar}$$ (1.24)

resulting in an alternating current with amplitude j_0 and frequency $\nu = 2eV/\hbar$. This effect is known as the ac Josephson effect.

A model for the temperature dependence of the critical current over an superconductor-isolator-superconductor tunneling junction was derived by
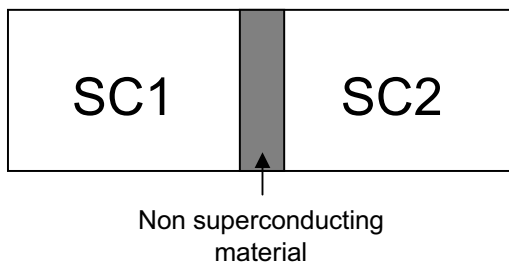

Figure 1.9: The Josephson junction consists of two superconductors separated by a thin layer of non-superconducting material.
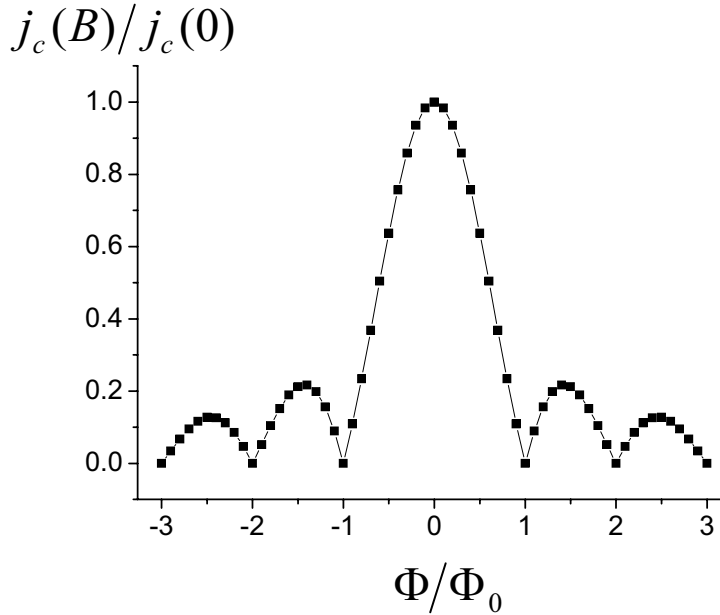
Figure 1.10: Magnetic field dependence of the Josephson tunneling current.

Ambegaokar and Baratoff[41] by use of the BCS-theory,

$$j_c(T) = \frac{\pi \Delta(T)}{2eR_n} \tanh\left(\frac{\Delta(T)}{2k_B T}\right). \tag{1.25}$$

Here $\Delta(T)$ is the temperature dependent BCS energy gap and R_n the normal state resistivity per unit area for the contact. Similar calculations can be done for the superconducting-normal-superconducting junction delivering a similar temperature dependence[42].

The temperature dependence for the Josephson current is plotted in Fig. 1.11 using the model of Ambegaokar and Baratoff.
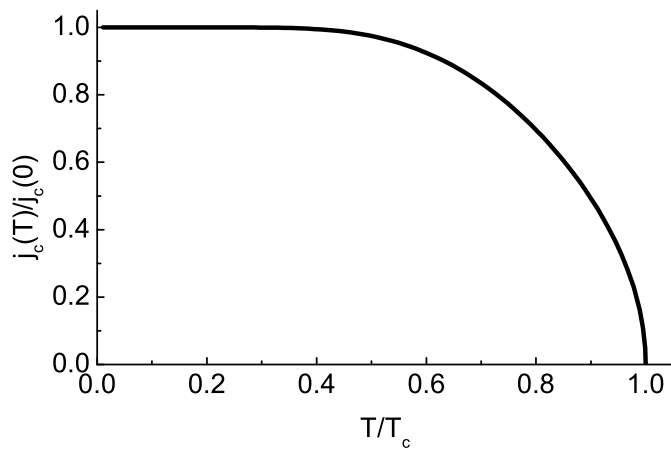
Figure 1.11: Temperature dependence of the critical current in a tunneling junction as described by the model of Ambegaokar and Baratoff.

Chapter 2

Superconducting Thin Films

The current density in a superconducting material is not only given by the intrinsic properties. In this chapter it will be discussed the influence of the sample geometry on the critical current distribution. Especially, thin films will be treated and the role their lateral geometry is playing. In this case the definition of thin holds for film thicknesses where the variation of the critical current can be ignored that is where the ansatz $j_c(d) = const$ is a good approximation. Since the current density use to vary over the length scale of λ, the films that are fulfilling this requirement need to have a thickness $d < \lambda$.

For thin films, the current component normal to the film plane can often be neglected to a good approximation. This is especially true for c-axis oriented HTSC, where the anisotropy of the superconducting properties leads to a critical current density along the c-axis $j_{c,c}$ which is much smaller than the in-plane components $j_{c,ab}$. For YBCO $j_{c,ab}/j_{c,c} > 250$. Thus, assuming a twodimensional current density in the film

$$\mathbf{j} = j_x(x,y)\mathbf{e_x} + j_y(x,y)\mathbf{e_y} \tag{2.1}$$

it will be possible to describe the critical current density in very simple geometries analytically. Such geometries are for example the circular disk[43] or the infinite slab[44].

2.1 Beans Model

For certain, in very simple geometries the Bean model[45] makes it possible to find analytical solutions for the magnetic flux- and critical current-density
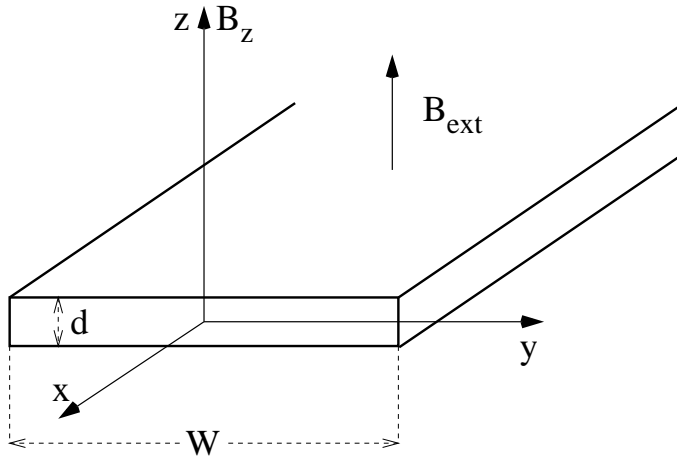
Figure 2.1: Sketch of the superconducting slab, introducing the used coordinates.

distributions. The simplest case is that of the infinite long slab with vanishing thickness[44] that will be treated in the following. The slab is assumed to be infinite along the x-direction, to have a width w and a thickness $d < \lambda$, see Fig. 2.1, where also the used coordinates with the z-direction normal to the film plane is defined. The Bean model assumes that when the slab is placed in an external field, the critical current density will be constant and maximal in the areas with penetrated magnetic flux. Further it is assumed that the magnetic flux starts to penetrate into the superconductor immediately when an external field is applied. Due to the geometry the field will be increased at the surface edges[46] and to set the lower critical field $H_{c1} = 0$ will make a satisfying approximation.

The special geometry of the slab together with the assumptions above give a one dimensional current density,

$$\mathbf{j} = j_x(y)\hat{\mathbf{e}}_x. \tag{2.2}$$

In this model it is now possible to find analytical expressions for the flux and current densities. The flux density along the z-direction is thus given by[44],

$$B_z(y) = \begin{cases} \frac{j_c\mu_0}{\pi}\operatorname{arctanh}\left[\frac{|y|c}{(y^2-Q^2)^{1/2}}\right] & |y| > \frac{w}{2} \\ \frac{j_c\mu_0}{\pi}\operatorname{arctanh}\left[\frac{(y^2-Q^2)^{1/2}}{|y|c}\right] & Q \leq |y| \leq \frac{w}{2} \\ 0 & |y| < Q \end{cases} \tag{2.3}$$

and the current density by,

$$
j_x(y) = \begin{cases} j_c \frac{y}{|y|} & Q \leq |y| \leq \frac{w}{2} \\ \frac{2j_c}{\pi} \text{arctanh} \left[\frac{yc}{(Q^2 - y^2)^{1/2}} \right] & |y| < Q \end{cases} \tag{2.4}
$$

with $c = 2 \left[(w/2)^2 - Q^2 \right]^{-1/2} w^{-1}$ and $Q = w/2 - P$. Here, P is the penetration depth of the magnetic flux defined from the edge of the slab. P thus also defines the area with constant current density and is dependent on the external magnetic field,

$$
P = \frac{w}{2} \left[1 - \cosh^{-1} \left(\frac{B_{ext}\pi}{\mu_0 j_c d} \right) \right]. \tag{2.5}
$$

The analytical solution to Eq. (2.3) can only be determined for vanishing thicknesses d and is only exact at the surface of the superconducting slab making it difficult to make a direct comparison of these results to experimental data. A different approach to calculate the flux density distributions is by the use of Eq. (2.4). From the resulting current density distribution it is possible to calculate the flux density distribution by the use of Biot-Savarts law. This approach makes it possible to calculate the flux density distribution at a height h above a superconducting slab with final thickness d. This is done by solving the following equation

$$
B_z(x, y, h, d) = \mu_0 H_{ex} + \frac{\mu_0}{2\pi} \int_{-W/2}^{W/2} \int_{-d/2}^{d/2} \frac{j_x(x', y')(y - y')}{(y - y')^2 + (h - z')^2} dy' dz'. \tag{2.6}
$$

As an example the flux density distribution will be calculated for a superconducting slab with width $W = 250 \ \mu m$, thickness $d = 250$ nm and critical current density $j_c = 2.9 \times 10^{11} \ A/m^2$. At a height $h = 250$ nm above the surface of the superconductor this results in flux density distributions that look like the ones that are depicted in Fig. 2.2 for different external fields. These values can be compared to results from magneto-optical measurements and the profiles are typical for thin superconducting films in an external magnetic field after zero-field cooling. Characteristic for the profiles are the large maxima in the flux density at the edges of the superconductor and inside the film an area of zero magnetic flux. This area is successively getting smaller with growing external field to finally disappear at high enough values. Looking at the profiles of the critical current density distribution, it is seen that it is dropping to small values at the same point as the magnetic flux profiles reach zero. Also, the critical current have a constant value in the area which is penetrated by magnetic flux.
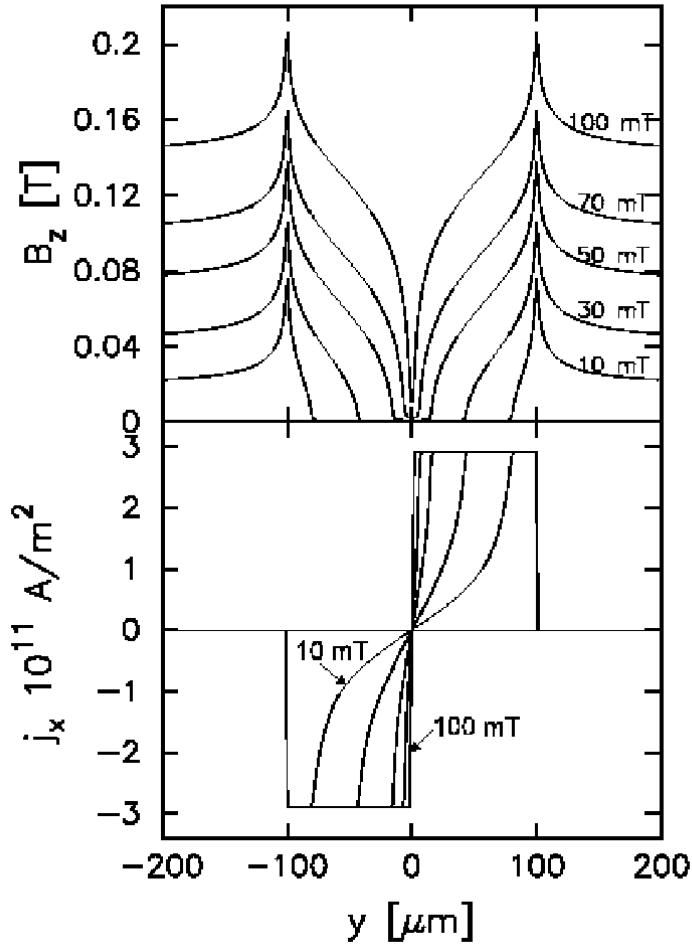
Figure 2.2: Flux and current distributions in a thin slab, as calculated from Eq. (2.4) and Eq. (2.6).The width of the slab is W=200 μm and the thickness d=250 nm. The resulting critical current density is $j_c = 2.9 \times 10^{11}$ A/m^2

2.2 Geometry

In general, for more complicated geometries, it is not possible to calculate the flux and current distribution as above. But for the case of the critical state, where the whole superconducting film is penetrated by magnetic flux and

a constant critical current j_c is flowing in all of the superconductor, there are simple descriptions also for more complicated geometries. Thereby it is useful to introduce a current potential $g(x,y)$ which is connected to the critical current density $j_c(x,y)$ through,

$$\mathbf{j}(x,y) = -\hat{z} \times \nabla g(x,y) = \nabla \times \hat{z} g(x,y), \qquad (2.7)$$

with $\hat{z}$ the normal vector perpendicular to the film plane[47]. If the critical current is assumed to be constant in all of the superconducting film, the current potential can be calculated with[48],

$$g(x,y) = j_c dist(x,y,\Gamma). \qquad (2.8)$$

Here $dist(x,y,\Gamma)$ is a function describing the shortest distant from a point inside the superconductor to the edge Γ. The equipotential lines of $g(x,y)$ are equivalent to the current stream lines in the superconductor. In Fig. 2.3 the solution for three different geometries, a square shaped, a triangular film as well a for a superconducting film in the form of a cross. Thereby the thick black lines with arrows is the current streamlines indicating how the current flows in the film plane. The dashed lines are so called discontinuity lines, short d-lines. They always arise between areas with different current direction. They can either be generated by a change in the direction of the current and are then called d$^+$-lines. d$^-$-lines on the other hand are located between areas where the current density possesses different magnitude. As seen in the images each corner of a superconducting film is a starting point for a d$^+$-line[49].

The d-lines can be visualized by magneto-optical imaging of superconducting films. Thereby the magnetic flux distribution in the film is pictured
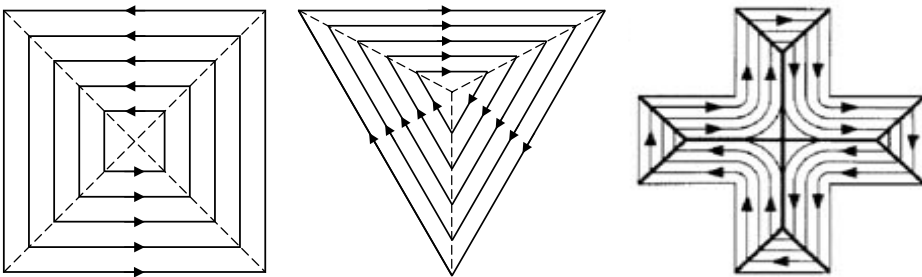

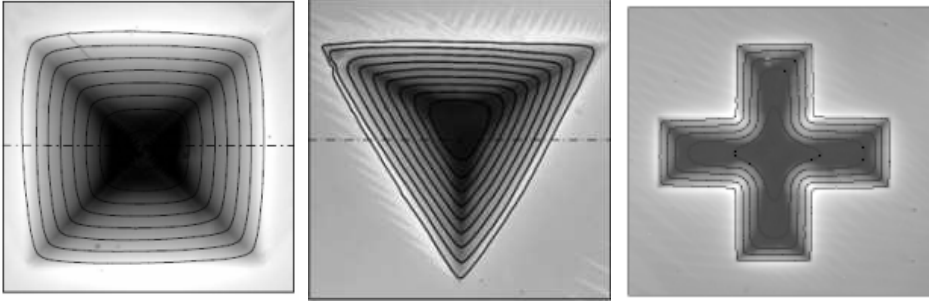Figure 2.3: Sketch of the current paths in three differently shaped films.

Figure 2.4: Magneto-optical images of the magnetic flux distribution in three films with different shape. Bright contrast refer to high magnetic flux. The d^+-lines are clearly seen as dark lines coming from the corners of the films. Also seen are the calculated current stream lines, showing the current path in the films.

and the d$^+$-lines are clearly seen as minima of local flux. In Fig. 2.4 corresponding magneto-optical images of the magnetic flux distribution in three superconducting films are shown. The images are taken while applying a magnetic field after zero field cooling. The bright areas are those with high magnetic flux, and the d$^+$-lines are clearly seen as dark lines running from the corners of the films. Also seen in the images are the calculated current stream lines.

For other geometries there is still a possibility to calculate the current distribution by dividing it along the discontinuity lines. Summation of such prism-shaped parts of the sample make it possible to calculate $B(x,y)$ in the whole sample[50].

2.3   Flux Lines in Thin Films

In thin films in perpendicular magnetic fields the critical current is essentially uniform throughout the thickness of the film. This leads to a penetration depth λ_{film} that is depending on the thickness of the film and which is much larger than the bulk λ. When solving Maxwells equations in the two dimensions of a thin film this results in[51]

$$\lambda_{film} \approx \frac{\lambda^2}{d}. \tag{2.9}$$

The radius of a flux line is expanding from λ in bulk to λ_{film} in thin films with $d < \lambda$. And while in bulk at $r = \lambda$, the radial dependence of the circulating sheet current density of the flux line changes from $1/r$ to an exponential

$e^{-r/\lambda}$ fall off, in thin films, the radial dependence of the critical current changes at λ_{film} and it changes from $1/r$ to $1/r^2$.

For a semithick film, there is a change in how the current density spread outward from the normal conducting core, see Fig. 2.5 a). The flux line has a much larger radius at the surface than in the interior. At the surface, the $1/r^2$ behavior is found for the current decay, while there is a slow transition into the exponential decay in the bulk. This transition takes place on the scale of λ which means films with $d < \lambda$ can be treated as thin in this context, see Fig. 2.5b), where the flux line has a constant $\lambda_{film} = \frac{2\lambda^2}{d}$ and thus also a constant critical current density throughout the film thickness.

Due to the large λ_{film} in thin films, there is a strong long range interaction force between the flux lines that is considerably larger than in bulk. Since there is a strong repulsion between the flux lines, there is a magnetic pressure required for further flux lines to enter the film even as the flux density is low. This results in long range lattice order.
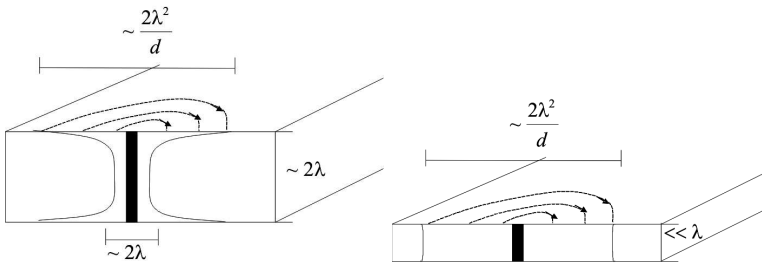

Figure 2.5: a) A flux line in a film where $d \approx 2\lambda$. b) A fluxline in a thin film with $d << \lambda$.

Chapter 3

Thin Films with Modified Microstructure

3.1   YBa$_2$Cu$_3$O$_{7-\delta}$

YBa$_2$Cu$_3$O$_{7-\delta}$[5] is a ceramic high temperature superconductor. Typical for this group of superconductors is their highly anisotropic layered structure built up of perovskite-like subunit cells. For YBCO the crystal structure exhibits a tripled unit cell of perovskite type. The crystal structure of YBCO can change depending on the oxygen stoichiometry. In Fig. 3.1 the orthorhombic phase is shown, which is the superconducting phase. The orthorhombic unit cell contains two CuO$_2$ planes situated symmetric above and below the Y atom. It is in these planes that the superconductivity takes place. Each copper atom is surrounded by 5 oxygen atoms that form a pyramid with a basis area that is slightly distorted ($\approx 2\%$) from a square. There are also Cu atoms between the Ba atoms, which form Cu chains parallel to the b-axis. These Cu atoms are only surrounded by 4 O atoms since the oxygen sites along the a-axis are not occupied. Further, the YBCO unit cell consists of three subunit cells, two containing a Ba atom and one which is situated inbetween them containing an Y atom.

The dimensions of the unit cell are seen in Table 3.1. The c-axis lattice constant is much larger than those for the other two lattice directions. The values for the a- and b-axis are almost identical which leads to frequent formation of twin boundaries, since areas with different orientations can easily be formed by the crystal growth.

Depending on the oxygen doping, the crystallographic phase changes. Beside the superconducting orthorhombic phase also a tetragonal phase exists at low oxygen doping. The oxygen doping can be described by the parameter δ. For $\delta = 1$ there is tetragonal YBa$_2$Cu$_3$O$_6$ which is an anti-

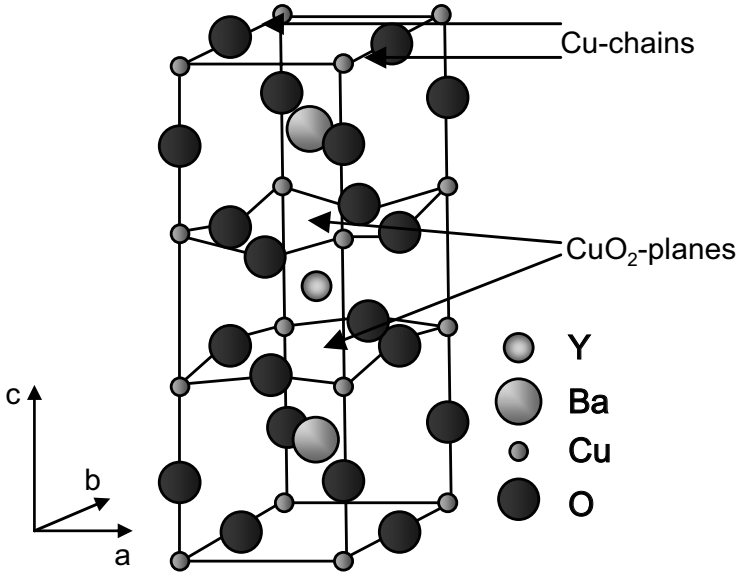Figure 3.1: Unit cell of YBCO in the orthorhombic phase.

a	0.3814 nm
b	0.3884 nm
c	1.1660 nm

Table 3.1: Lattice constants of YBCO[52].

ferromagnetic insulator. When δ is getting smaller a phase transformation occurs at $\delta = 0.6$ into the orthorhombic phase. At the same time there is a phase transition from the antiferromagnetic insulator to the superconducting phase. Fig. 3.2 shows the phase diagram for YBCO, which is typical for the cuprate high temperature superconductors. As seen in the phase diagram, at $\delta = 0.05$ the superconductor has its highest transition temperature $T_c = 93$ K. This $YBa_2Cu_3O_{6.95}$ is the optimally doped form of YBCO. With increasing δ, the transition temperature decreases and the system moves into the so called underdoped regime. In the same way for decreasing δ also T_c decreases and the system moves into the overdoped regime which is small since δ can not get negative.

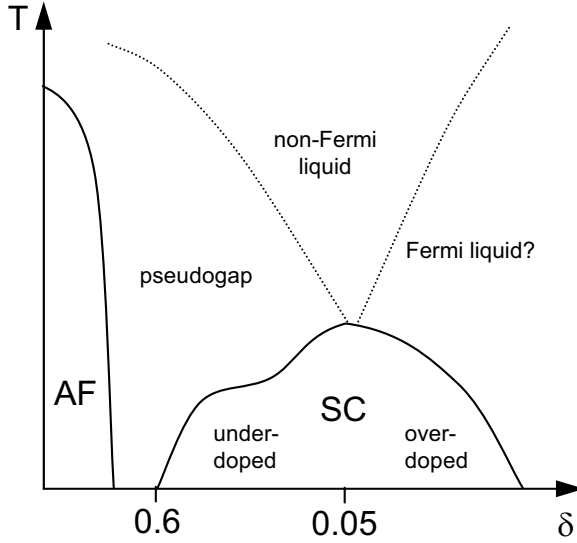This can be understood by looking at the electronic structure of YBCO.

Figure 3.2: Phase diagram of $YBa_2Cu_3O_{7-\delta}$. Depending on oxygen doping δ and temperature the system can show antiferromagnetic, metallic or superconducting properties.

Important for superconductivity are the CuO_2 planes that are situated symmetrically on both sides of the Y^{3+} ion, and the one dimensional Cu-chains situated between the Ba^{2+} ions. The fully doped compound is $YBa_2Cu_3O_7$ where all the oxide sites are filled. With increasing δ more and more oxide atoms leave the oxide chains until at $\delta = 1$ they are completely extinguished [53]. The CuO_2-planes always remain fully occupied. Owing to the strong electro-negativity of the oxygen, occupation of the oxide sites in the copper chains leads to a transfer of electrons from the planes into the chains. Thus with a decreasing δ, a stronger hole doping in the planes is achieved. These holes are those for the superconductivity relevant charge carriers. In this way, an increasing δ lead to a reduction of charge carriers and, thus, also the superconducting properties like the transition temperature are reduced.

Since superconductivity takes place in the two-dimensional CuO_2-planes, there is an extreme anisotropy of the material properties in these compounds. This anisotropy is reflected in the important superconducting parameters. The penetration depth, $\lambda_c = 700 - 800$ nm is much larger than $\lambda_{ab} = 140 - 160$ nm and the coherence length, $\xi_{ab} = 1.0 - 2.0$ nm larger than $\xi_c = 0.3 - 0.4$ nm[54].

The coherence length along the c-direction shows roughly the same value as the distance between the CuO_2-planes. This leads to a suppression of the density of Cooper pairs between the planes. This can also lead to a decoupling of the superconducting planes along the c-axis as found in the bismuth-cuprates[55]. The region with decreased density of Cooper pairs can be treated as a kind of weak link and the currents flowing along the c-axis can thus be described by the Josephson equations[40].

3.2   Growing $YBa_2Cu_3O_{7-\delta}$ Thin Films

The structural properties of YBCO as described in the previous chapter is strictly valid only for bulk material. In thin films the interfaces have a substantial influence on the superconducting properties which will be discussed in detail in the following chapters. The quality of the interfaces of a film depends strongly on the way of production. Thin epitaxial films of YBCO can be grown using different techniques either onto single crystalline or highly textured substrates[56]. Common methods for film growth are thermal evaporation, cathode and ion beam sputtering and pulsed laser deposition, that all need vacuum[57]. Other procedures not needing vacuum are methods of chemical deposition like metal organic deposition[58] and sol-gel technique[59].

Pulsed Laser Deposition

All films used in this work have been produced using Pulsed Laser Deposition (PLD)[60, 61]. With this method it is possible to grow epitaxial thin films with high quality. It is well suited for growing complex materials like YBCO since there is a stoichiometric transfer of material from target to substrate. It makes it quite easy to produce multilayered films of different materials by sequential ablation of different targets as well, for example hybrids of superconducting YBCO and ferromagnetic $L_{2/3}Ca_{1/3}MnO_3$.

In Fig. 3.3, a sketch of a PLD setup is shown. In the upper part the target is seen as black rectangle. It is made of polycrystalline YBCO with cation stoichiometry and is fixed on a rotating target holder to achieve uniform ablation of the target. Target and substrate are situated inside a vacuum chamber. A pulsed laser beam passes through a quartz window into the chamber to hit the target. Usually an Excimer-Laser is used, having a wavelength in the ultraviolet range. The laser beam is strongly absorbed by the black target, which is thus heated up until a plasma is formed. The
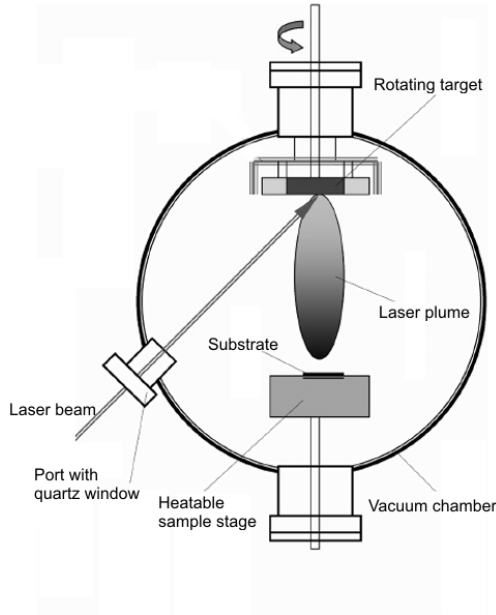
Figure 3.3: Sketch of the setup used for Pulsed Laser Deposition.

plasma expands until it reaches the substrate where the plasma material is deposited and nucleation and growth of the film on the substrate surface takes place. This process is usually run at temperatures between 700 °C and 800 °C at an oxygen pressure of a few tenth of a millibar. At these conditions the tetragonal phase YBa$_2$Cu$_3$O$_6$ is stable and is growing epitaxially onto the substrate[62]. In the laser ablation process very high partial pressures of the single components of the material occur which means the process is running very far from the thermal equilibrium. Only in this way is it possible to get the desired layer growth with well defined orientation of the materials. The resulting film is in the isolating tetragonal phase and must be oxygenated to transform into the superconducting orthorhombic phase[63]. This is done by enhancing the oxygen pressure to 750 mbar and let the sample cool down to room temperature in a particular temperature protocol.

The way the layers of the film are growing is strongly dependent on the kind of substrate used. Commonly used materials are among others SrTiO$_3$ (STO), LaAlO$_3$ and MgO. All materials possess an from YBCO differing size of the unit cell. This lattice mismatch relative to the YBCO unit cell is shown in Table 3.2. Since there is no substrate material having lattice pa-

rameters exactly corresponding to those of YBCO, no Frank-van-der-Merwe layer by layer growth is possible[64]. Instead there is strain increasing with each layer and eventually the growth mode changes and defects like growth island will occur[65, 66, 67].

	a	b	c
SrTiO$_3$	2.14%	0.49%	0.29%
LaAlO$_3$	-0.81%	-2.42%	-2.62%
MgO	10.20%	8.41%	8.19%

Table 3.2: Lattice mismatch between commonly used substrates and YBCO.

3.3   Growth of YBCO on Well Oriented SrTiO$_3$ Single Crystalline Substrates

There is no substrate material for growing YBCO that has a perfect lattice match. The difference in size of the lattice parameters leads to strain in the growing film. When using well oriented SrTiO$_3$ as substrate material the lattice mismatch is, for a 2.14%, for b 0.49% and for c 0.29%. This relativley small diffrence leads to a misfit strain energy which is increasing with each layer. This means that for the first several layers the film is growing layer-by-layer but at a certain film thickness it changes into island growth. The formation of islands on a thin wetting layer as it occurs here is the so called Stranski-Krastanov growth, where there is a competition between interface energy and strain energy. The strain that has built up in the film due to the lattice mismatch is reduced by the formation of islands[68]. Island growth is occurring on all substrate materials but start at different thicknesses, which in case of STO is after 8 to 16 monolayers.

The lateral size of the islands increases with film thickness and eventually neighboring islands grow together. But at each growth layer new islands nucleate as well. This process results in a film built up from pyramidal formed islands that coalesce and overgrow each other. In Fig. 3.4 an image made by scanning tunneling microscopy of one such growth island is shown[69]. The terrace structure is typical and the step height is usually one YBCO unit cell.

Due to the coalescence of growth islands the Stranski-Krastov growth results in a superconducting film containing a high density of defects like screw dislocations[70, 71, 31], anti phase boundaries[72, 73, 74], and grain boundaries[75].
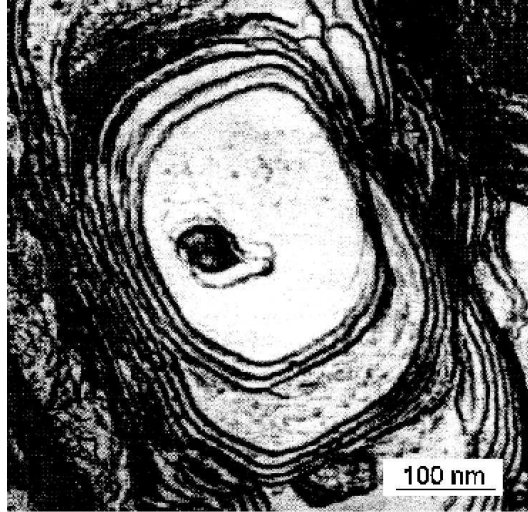
Figure 3.4: Image made by scanning tunneling microscopy showing a single growth island in YBCO grown on STO(001)[69].

Grain Boundaries

Grain boundaries are formed in epitaxial thin films due to the island growth. To see what impact they might have on the superconducting properties, a polycrystalline sample is considered as an example of this extreme situation. The polycrystalline sample has a microstructure consisting of arbitrarily ordered grains in the size of some 10 μm. Fig. 3.5(a) shows the critical current distribution in such a polycrystalline sample of optimally doped $YBa_2Cu_3O_{7-\delta}$[76]. A small section of the sample is depicted inFig. 3.5(b) where the magnetic flux distribution is shown together with the current stream lines. The diameter of the sample is 1 mm and the images were taken at $T = 5$ K in an external field of $B_{ex} = 64$ mT. Although the superconductor locally shows values of several 10^9 A/m^2 the resulting transport current can only reach some 10^6 A/m^2. This is explained by the granularity of the superconductor, where the grains are arbitrarily oriented to each other. This results in grain boundaries of more than 10°, which is much above the region defined as low-angle grain boundaries. For these large-angle grain boundaries there is a very strong suppression of the critical current compared to the values in the single grains[76]. The current carrying properties are strongly dependent on the orientation between neighboring grains. For low-
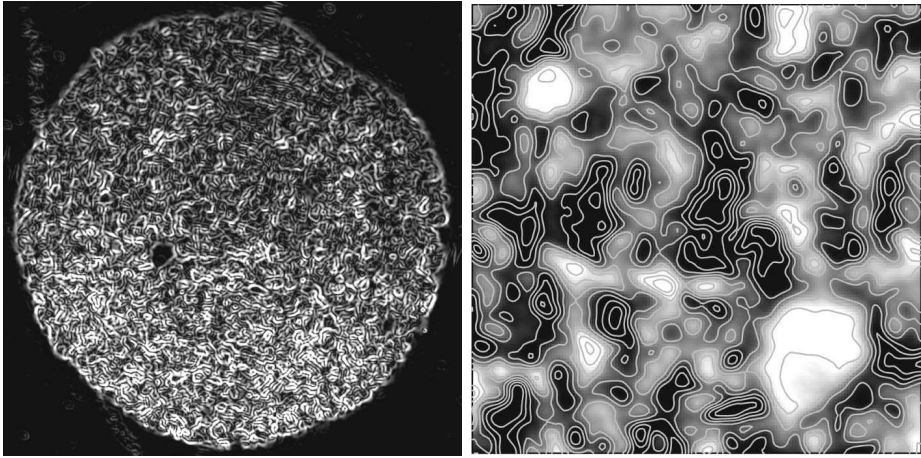
(a) Current distribution in the sample.

(b) Detail of the sample sample as in a) show-
ing the flux distribution together with current
stream lines.

Figure 3.5: Magneto-optical images of a polycrystalline YBCO sample for an ex-
ternal field $B_{ex} = 64$ mT and $T = 5$ K.[76]

angle grain boundaries the situation is completely different and they are able
to carry critical currents comparable to those in the single grains[77, 78].

To achieve high transport currents in superconducting films, this shows
that it is crucial to limit the number of grain boundaries and increase the
quality of their transparency mainly by reducing the grain boundary angle
between the grains.

3.4   Thin Films on Vicinal Cut SrTiO$_3$

To influence the micro structure of thin films various substrates can be used.
One possibility to modify the properties of superconductors like transport
current, is the use of differently structured substrates. A special substrate is
the vicinal cut substrate on which it is possible to grow homogeneous films
nearly without grain boundaries[79, 74]. These substrates cause a change of
the growth mode and a restraint of the island formation occurring on flat
substrates. Also they enable the controlled generation of an array of planar
defects throughout the film, so called anti phase boundaries (APB). Due to
the special surface a step-flow growth can occur on these substrates. Thereby
the growing superconducting material will self-organize at the substrate sur-
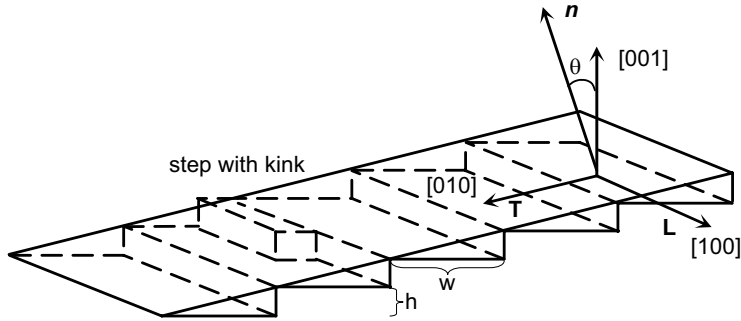
Figure 3.6: Sketch describing the surface of a vicinal cut substrate.

face. [80]. This results in a film with a completely modified microstructure as compared to the film grown on a flat substrate.

A vicinal cut substrate has its surface tilted slightly away from the crystallographic c-axis. A sketch of the vicinal surface is depicted in Fig. 3.6 including the tilt angle θ. The free energy of the surface will be reduced if terraces are formed having locally the (001) orientation. The deviation from the macroscopic orientation of the plane is thus compensated by the formation of straight steps[74, 79]. Ideally, the vicinal surface forms a structure with terraces having a width w and a step hight h, related through the angle θ as

$$tan\theta = \frac{h}{w}. \tag{3.1}$$

In reality however there will be a variation of step heights and terrace widths. If there is an additional deviation from the (010) or (100) orientation in the STO, the step height will change and kinks will form[74].

To grow a film with a highly regular terrace structure separated by straight parallel steps the STO substrate must be heated to 930 °C[74]. At this temperature the mobility of the surface atoms is strongly enhanced, which enables a reorganization to a surface with minimal free energy. The resulting substrate surface exhibits step edges which are extremely straight and exclusively aligned along the [100] direction having nearly constant terrace widths. This is important since only on such substrates the superconductor grows to have a defect structure enabling the extremely high critical currents.

Directly at the surface steps there is a higher binding energy making them to preferable adsorption sites. If the deposited YBCO particles have

sufficient mobility and are located closer than the diffusion length λ_s they can diffuse to a surface step. Particles further away from a step might instead arrange themselves into islands which make it important for the step width to be smaller than λ_s. If this is fulfilled there will be an organized step-flow growth of the superconductor resulting in an extremely smooth film nearly without grain boundaries.

YBCO on STO(106)

With larger tilt angle, the terrace width is decreasing and the density of planar defects increases. But not for all angles the resulting film will have a regular step and terrace structure, but there will be certain orientations for which the vicinal surface configuration will be exceptionally stable[74]. One of such orientations is the crystallographic (106) orientation, which corresponds to vicinal angle of about 10 °. The periodicity of the terrace structure is for this orientation particularly pronounced. A particular angle of $\theta = 9.46$ ° leads to a terrace width $w = 2.3$ nm and a step height of 0.39 nm. Thus, the terraces consist of six unit cells STO separated by steps of one unit cell height. In Fig. 3.7 a) the surface of a STO(106) substrate is seen, the image has been obtained using a scanning tunneling microscope. To see is that the terrace width is extremely constant over all of the surface.

The resulting YBCO film grown onto this substrate is depicted in Fig. 3.7 b), the thickness being 240 nm. With increasing film thickness the width of the terraces is increasing and for this film it has an average $w = 4.9$ nm.

Since the step heights are smaller than the YBCO unit cell along the c-axis $c = 1.2$ nm, there is a formation of planar defects along the c-axis which is due to a relative shift of the unit cells along this direction[74]. Such shifts play an important role for the formation and annihilation of anti-phase boundaries, but also for the overgrowth of neighboring substrate steps, see Fig. 8.27. Since the growth of YBCO is starting with the BaO subunit cell and the step hight is c/3 (YBCO), a planar defect will form due to the stacking mismatch[81]. This will last until a stacking fault is eventually generated, for example by the growth of two succeeding BaO subunits cells. The width of the terraces does not exceed 4-7 nm for YBCO grown onto STO(106). This results in a very high density of planar defects in the film. Furthermore, the structural width $r_p \approx 0.7 - 1$ nm of the anti-phase boundaries is smaller than the coherence length ξ_{ab} of YBCO.

By growing YBCO onto a vicinal STO(106) substrate it is possible to produce a superconducting film, which is very homogeneous along the steps
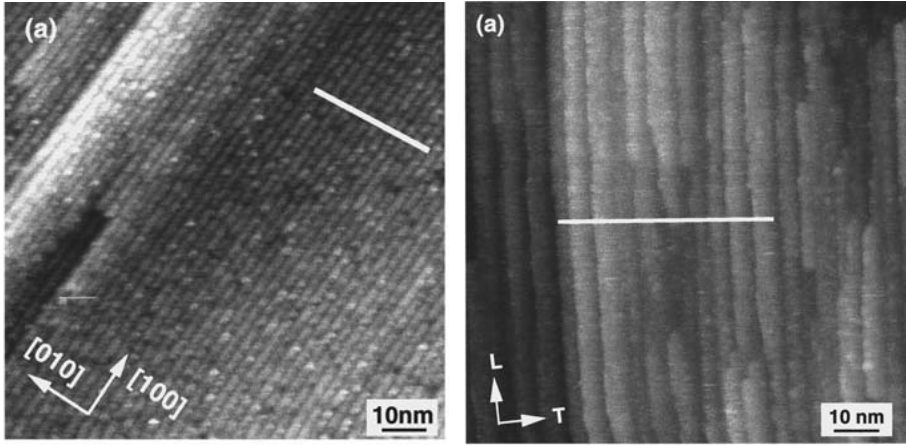
(a) SrTiO₃ surface after UHV annealing.

(b) The corresponding YBCO film grown onto the substrate in a).

Figure 3.7: STM images with area 100 nm×100 nm, clearly showing the step and terrace structure in substrate and film[74].
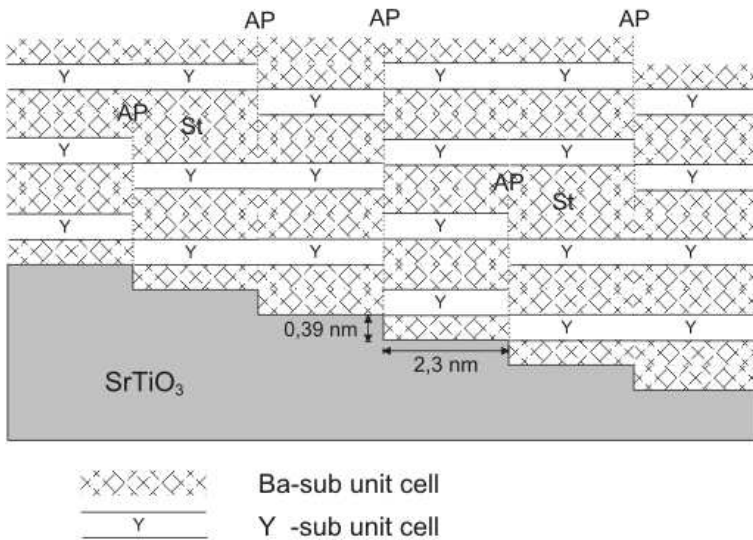

Figure 3.8: Sketch showing how anti phase boundaries are formed and annihilated in the YBCO thin film.[82].

and at the same time introduces an array of planar defects in a controlled way. This gives us a film with high critical currents and a well defined microstructure, containing two fundamentally different directions[74, 83]. It will be seen in the following chapters that these two directions will exhibit completely different properties for current transport. Owing to the unusually well defined microstructure, films grown on vicinal substrates are ideal for studying complex properties in superconductors. Especially, if there is a strong connection to the microstructure as for critical currents.

Chapter 4

Ferromagnetism and Superconductivity

The properties of superconducting films can not only be influenced by the chosen substrate. Another approach is the creation of a second interface to different types of materials. Examples are structures consisting of superconducting and normal metals or magnetic materials. This work will focus on the interesting combination of a high-temperature superconductor (HTSC) and a ferromagnet (FM). Such a combination makes it possible to influence the critical current density in the superconductor via the magnetization of the ferromagnet.

Superconductivity and ferromagnetism are two phenomena that are antagonistic by nature. While in the ferromagnet the spins of the electrons order themselves parallel which lead to a magnetic momentum, in the superconductor the electrons form Cooper-pairs with antiparallel spin. The creation of a hybrid structure of a superconducting and a ferromagnetic thin film leads to a competition of the antagonistic ordering phenomena at the interface[84]. This interaction leads to interesting properties of this kind of hybrid structures. In both layers, there is a reduction of the transition temperature[85, 86], proving that both the ferromagnet and the superconductor are strongly influenced by the other part. While the phenomenon of superconductivity has already been treated in the previous chapters, next a short introduction to the ferromagnetic material will be given.

4.1   Ferromagnetic Manganites: $La_{2/3}Ca_{1/3}MnO_3$

Rare earth manganites are oxide compounds with interesting structural and physical properties, like doping dependent electric conductivity, ferromagnetism and large magnetoresistance values[87]. Thin films can even exhibit
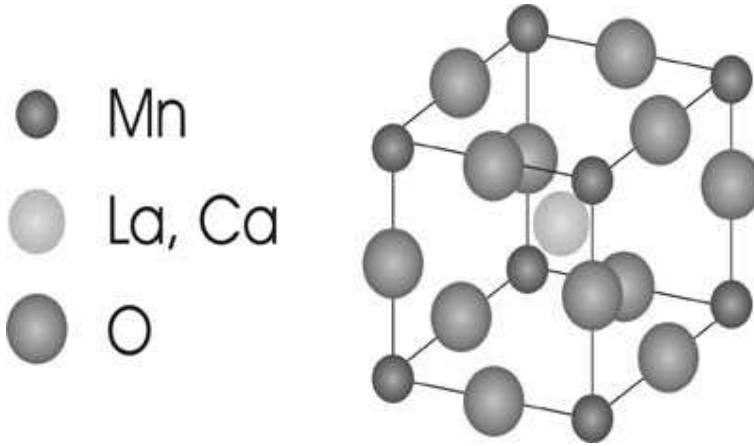
Figure 4.1: Unit cell of LCMO.

a colossal magneto resistance[88]. The crystal structure of the manganites is that of a cubic Perowskite. This makes it similar to the oxide high temperature superconductors[89, 90]. The unit cell of LCMO is depicted in Fig. 4.1. It has a La or Ca atom in the center surrounded by Mn and O atoms.

In this work only the doped $LaMnO_3$ will be discussed. In its pure form it is an antiferromagnetic insulator which properties are changing when introducing a dopant like Ca, Sr, Ba or Pb. Depending on temperature and doping-concentration, the manganites can be a ferromagnetic metal, ferromagnetic insulator, antiferromagnet or exhibit canted ferromagnetism or charge and orbital ordering[91]. The phase diagram of the Ca-doped $LaMnO_3$, that is $La_{1-x}Ca_xMnO_3$ is depicted in Fig. 4.2. If doped with 1/3 Ca which will be located at the La sites, the obtained phase is a ferromagnetic metal $La_{2/3}Ca_{1/3}MnO_3$ (LCMO) which has a bulk transition temperature of 275 K. Above this temperature it is a paramagnetic insulator.

Since this work is concentrating on thin films the special properties of thin film LCMO need to be illuminated. In Chapter 3 the strong influence of the substrate on the superconucting properties in an oxide high temperature superconductor was discussed. Naturally also the properties like the local magnetization of the LCMO thin film can be influenced by the choice of the substrate as will be seen below. Depending on the lattice mismatch between substrate and film strain fields are created during epitaxial growth. Thin LCMO films grown under compressive strain for example on $LaAlO_3$
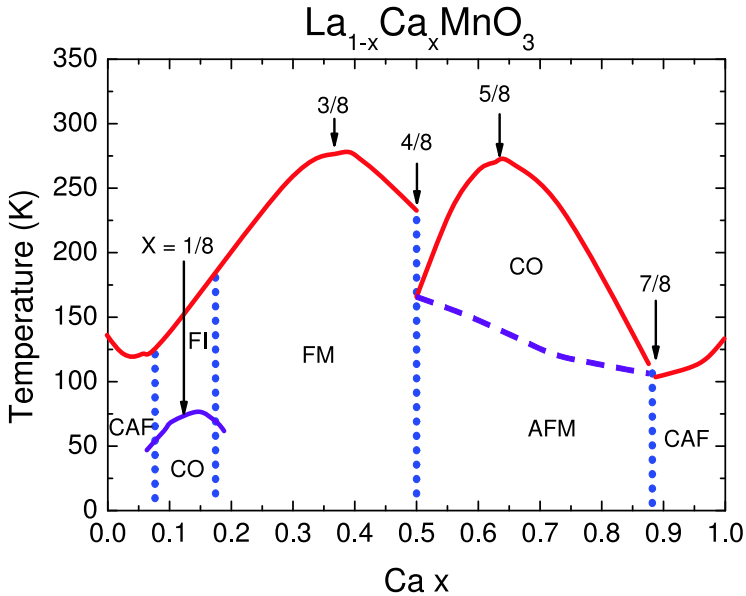
Figure 4.2: Phase diagram of $La_{1-x}Ca_xMnO_3$. FM: Ferromagnetic Metal, FI: Ferromagnetic Insulator, AF: Antiferromagnet, CAF: Canted Ferromagnet and CO: Charge/Orbital Ordering. After S.-W. Cheong and H.Y. Hwang[91].

exhibit out-of-plane magnetization, while films grown under tensile strain fields, like on STO show in-plane magnetization[92, 93]. This can be seen in Fig. 4.3 where typical domain patterns in two LCMO films at zero magnetic field are imaged with a magnetic force microscope. The black and white contrast comes from the uniform magnetic field distribution in the films. In a) an LCMO film grown on $LaAlO_3$ that is under compressive strain, taken from[94] is seen. It has a maze-like domain pattern typical for out-of-plane magnetization. This, in contrast to the film shown in b), taken from[95], which has been grown on STO, which mean tensile strain. For this film, the domain pattern look feather-like which is an indication for in-plane magnetization.

Further, if grown onto a vicinal cut substrate a magnetic anisotropy has been observed for ultrathin films[96]. It manifests as uniaxial magnetic anisotropy with easy axis along the steps of the substrate.

Also typical for the hole-doped rare-earth manganites is the high spin polarization of the transport electrons[97]. There are two subbands found,
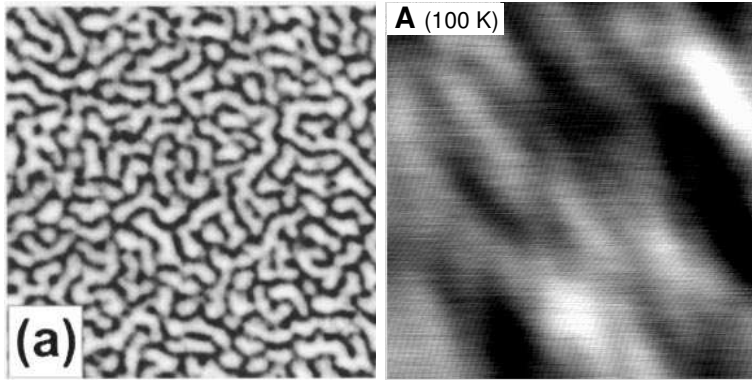
(a) $La_{0.7}Ca_{0.3}MnO_3$ grown on LaAlO$_3$ under compressive strain, showing out-of-plane magnetization. From [94].

(b) $La_{0.65}Ca_{0.35}MnO_3$ grown on SrTi$=_3$ under tensile strain showing in-plane magnetization. From [95].

Figure 4.3: MFM images of the magnetic domain patterns in two different LCMO films.

the first for the majority spins, carrying a spin directed along the magnetization. The second subband is for the minority spins, who are directed against the magnetization. Due to exchange interaction, the subbands are shifted with respect to each other resulting in a finite magnetization[98]. There are many different definitions of the spin polarization P[99]. One of them defines P as the normalized difference at the Fermi level between the majority $n\uparrow$ and minority $n\downarrow$ density of states,

$$P_n = \frac{n\uparrow - n\downarrow}{n\uparrow + n\downarrow}.\tag{4.1}$$

Other definitions are as the normalized difference between majority and minority current densities, resistivities or in the case of superconducting/ ferromagnetic contacts, the difference in current over the contact.

4.2 Superconductor/Ferromagnet Heterostructures

In hybridstructures of superconductors and ferromagnets, high quality interfaces are a crucial prerequisite for achieving strong connection between the two materials. This can be fulfilled by using materials possessing similar crystal structure. For YBCO having a Perowskite-like unit cell it will be suggestive to make a combination with a ferromagnetic Perowskite. LCMO is a
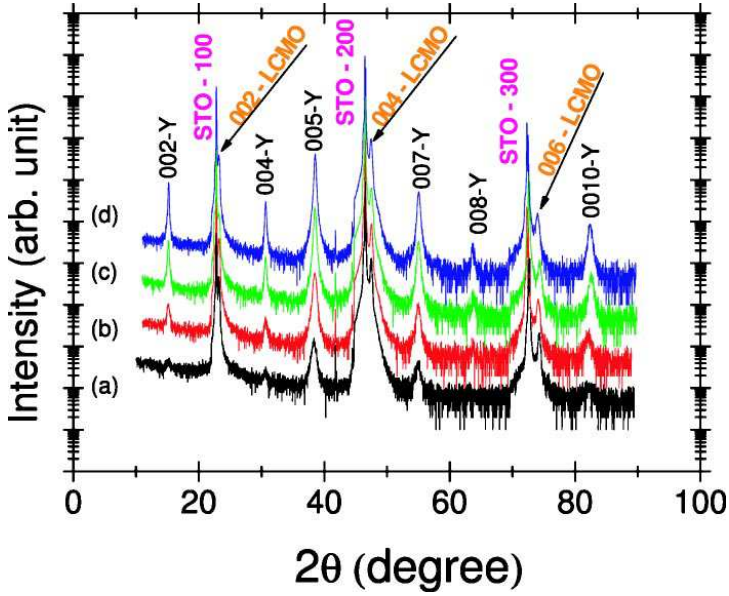
Figure 4.4: X-ray pattern for heterostructures consisting of 50 nm LCMO and (a) 20 nm, (b) 30 nm, (c) 50 nm and (d) 100 nm of YBCO, respectively. From Soltan et al. [86].

good choice since the in-plane lattice parameters of LCMO and YBCO are very similar. This makes it possible to grow bilayers epitaxially, exhibiting a structurally sharp interface[100].

The bilayers have been grown by pulsed laser deposition(see Chapter 3.3) from targets of $L_{2/3}Ca_{1/3}MnO_3$ and $YBa_2Cu_3O_{6.95}$ respectively[61]. The substrates were held at a constant temperature of 780 °C. During the deposition of YBCO the oxygen pressure was kept at 0.6 mbar and during the deposition of LCMO at 0.4 mbar. After the growth the bilayers were annealed in situ at $T = 530$ °C and an oxygen pressure of 1.0 mbar for 30 min.

The resulting bilayers show full oxygenation, high crystalline quality and sharp interfaces[100]. In Fig. 4.4 the X-ray diffraction pattern is shown for bilayers of 50 nm LCMO and 20-100 nm YBCO grown on a STO(100) substrate[86]. Only (00l) diffraction peaks are appearing for both YBCO and LCMO proving the c-axis textured growth of both layers. The diffraction pattern does not change if the growth order is altered.
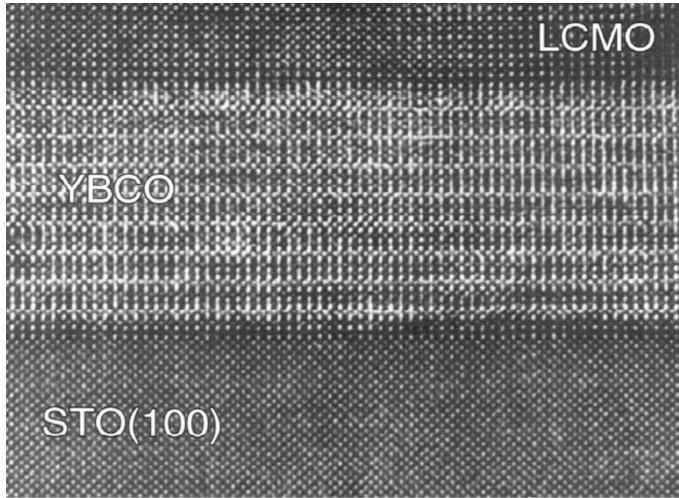
Figure 4.5: High resolution TEM image showing the crossection of a YBCO/LCMO super lattice, after Habermeier et al.[100]

Transmission electron microscopy images like in Fig. 4.5[100], show an atomic flat interface between the layers. This shows that the LCMO and YBCO can be grown cube on cube resulting in structurally high quality interfaces.

Interaction Between Superconductor and Ferromagnet

Though being generally incompatible phenomena, ferromagnetism and superconductivity can coexist in hybrid structures of the two constituents. Looking at a sample consisting of one LCMO layer of 50 nm thickness grown on STO and on top a layer of 100 nm of YBCO. The magnetization is measured with a SQUID magnetometer between 5 and 300 K. The coexistence of superconductivity and ferromagnetism can be seen in Fig. 4.6, where the magnetization has been measured as function of temperature both field cooled and zero field cooled in an external in-plane field of 100 Oe. The figure shows, that the sample orders ferromagnetically at $T = 145$ K and has a superconducting transition at $T = 87$ K. There is a diamagnetic signal occurring below $T = 87$ K in the zero field cooled measurement. This demonstrates that below this temperature both superconducting and magnetic ordering appears in the same sample.

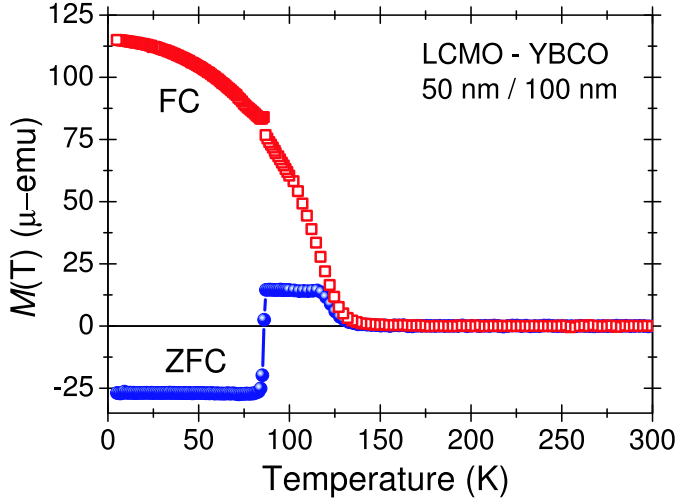At the interface there is a strong competition between the two ordering

Figure 4.6: Temperature dependence of the magnetization in a bilayer consisting of 50 nm LCMO and 100 nm YBCO. The measurements were done after zero-field cooling (ZFC) and field-cooling (FC) in an in-plane magnetic field of $H_{ext} = 10$ Oe. From S. Soltan[101]

phenomena, which usually leads to suppression of both transition temperatures [85, 86]. To explain this several processes have been suggested like oxygen diffusion[102], charge transfer[103], redistribution of orbital occupancy[104], spin diffusion[86, 105] and dipolar magnetic coupling via stray fields[106]. Below the last three processes will be shortly described.

Magnetic Coupling via Stray Fields

Studies on hybrid systems of conventional superconductors and metallic ferromagnets have shown a strong influence of the ferromagnet on the pinning properties in the superconductor. It is possible to enhance the intrinsic flux line pinning by introducing magnetic structures in the vicinity of the superconductor[107, 108, 109, 110].

Owing to the different length scales in the HTSC materials, where λ is about two orders of magnitude larger than ξ, usually only weak magnetic pinning is found. The magnetic pinning is created by an interaction of magnetic structures with the flux lines and since the magnetic energy is varying on the length scale of λ, this lead to an magnetic flux line energy that is smeared out over a comparably large length scale in the HTSC. It has

thus been a surprise that in epitaxial bilayers of YBCO and ferromagnetic perowskites like $SrRuO_3$ or LCMO substantial magnetic pinning has been found at all temperatures[111, 112, 108]. There, magnetic stray fields of the domain pattern in the ferromagnet cause a substantial pinning force density on the flux lines in the superconductor.

Bilayers of YBCO and LCMO can be fabricated with a thin insulating barrier of 5 nm STO layer between the two functional materials which leads to an electronic decoupling[112]. The remaining possibility for interaction between ferromagnet and superconductor is by magnetic stray field coupling.

Investigations of such bilayers using a SQUID magnetometer show for the hysteresis loops a lack of symmetry with respect to the vertical axis. This asymmetry is an indication either for magnetic pinning of the flux lines in the superconducting layer or of granular structure in the superconductor[113]. But since a change of the effect occurs for different substrates and no granularity is seen in the magneto-optical images, the effect is most probable due to magnetic pinning. In Fig. 4.7 the contribution of magnetic pinning to the overall pinning is depicted for different bilayers and for temperatures up to $T = 80$ K.   There is a substantial contribution of magnetic flux line pinning for all samples and all temperatures[112]. In the samples grown
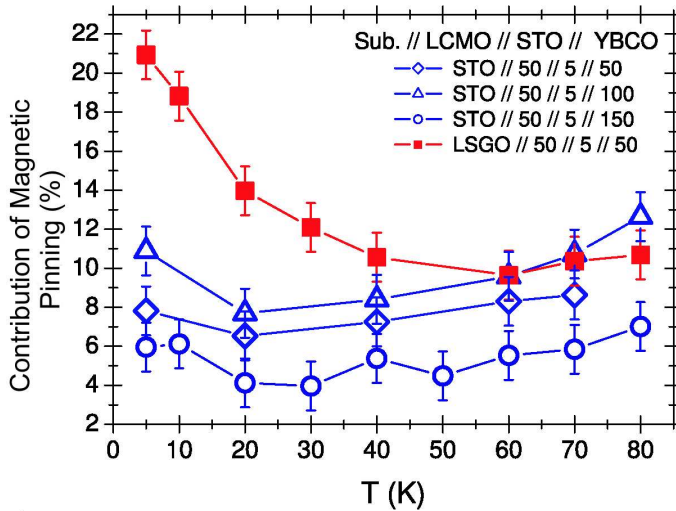

Figure 4.7: Contribution of magnetic pinning to the total flux line pinning, for different HTSC/FM heterostructures. From J. Albrecht et al.[112]
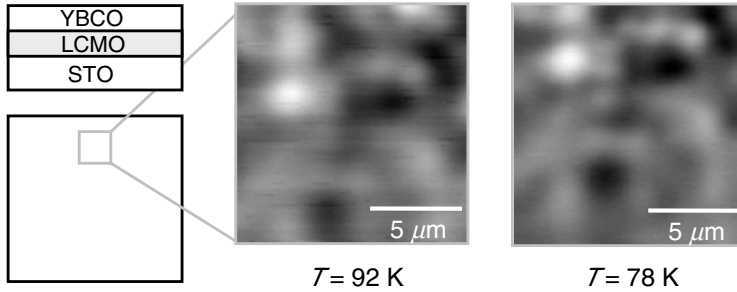
Figure 4.8: Images of the magnetic induction pattern above the LCMO/YBCO bilayer. The images were made above and below the superconducting transition respectively. The gray scale represents positive (white) and negative (black) values for the magnetic flux. From J. Albrecht et al.[106]

on STO, LCMO exhibits in-plane magnetization. If grown on $LaSrGaO_3$, which is under compressive strain, LCMO has an out-of-plane magnetization which is seen to lead to even stronger magnetic pinning effects. The conclusion from these measurements is that in electronically decoupled ferromagnet/superconductor bilayers there is a substantial contribution of magnetic flux line pinning.

Another evidence for magnetic dipolar interaction can be provided by visualizing how magnetic domains of the ferromagnet give rise to a spontaneous flux distribution in the superconducting layer[106]. Images of the magnetic field distribution directly above a YBCO layer were made using a Scanning Hall Probe Microscopy (SHPM) in a sample consisting of 50 nm LCMO and 100 nm YBCO. Two such images of an film area of $13 \times 13~\mu m^2$ are shown in Fig. 4.8 for temperatures above and below the superconducting transition, respectively. The gray scale represents the perpendicular component of the local magnetic field, where white refers to positive and black to negative values. The two images show identical magnetic patterns which mean there does not exist any flux-free Meissner state in the superconducting state. There is a spontaneous creation of flux lines in the superconducting film due to the presence of the adjacent ferromagnetic layer. This clearly shows that the stray field of the ferromagnet can penetrate the whole superconducting layer and that the interaction is not only limited to a thin surface layer. This leads necessarily to an interaction of the magnetic pattern and the flux line system[106].

Spin Diffusion

Looking at structures of a normal metal and a superconductor with a highly transparent interface, there is a decaying but finite probability to find Cooper pairs in the normal metal. This is called proximity effect and the length describing the decay of the Cooper pair density in the normal metal is given by the proximity length ξ_{prox}. The proximity effect gives rise to interesting physical effects, for example reduced critical temperature in the superconducting layer.

In ferromagnet/superconductor heterostructures, the proximity effect is strongly suppressed. This is due to the destructive action of the exchange energy J_{spin} on the Cooper pairs. This exchange energy is the difference between the two occurring spin bands in the ferromagnet. Since the electrons of a Cooper pair are in different spin bands, the Cooper pairs will break up if J_{spin} is large enough.

While in bilayers of metallic ferromagnets and low-temperature superconductors there are oscillations in T_c due to the tunneling of Cooper pairs into the ferromagnetic layer[114, 115], no such effect has been seen in superlattices of half metal ferromagnets and high temperature superconductors[100, 85]. This can be understood by the large exchange energy $J_{spin} = 3$ eV of the manganites[116].

Instead there is an inverse proximity effect in these heterostructures. There is self-diffusion of spin-polarized quasiparticles into the superconducting layer driven by the force of the exchange energy, see Fig. 4.9. At the interface the Cooper pairs are sharing their spins between the superconductor and the ferromagnet. The spin of the electron in the ferromagnet is expected to be parallel to the magnetization, and consequently the spin of the electron in the superconductor must be antiparallel to the magnetization[117].

The injection of quasiparticles into the superconductor creates locally an nonequilibrium state with a suppressed superconducting order parameter and a suppressed critical current density and transition temperature[118].

Bilayers of LCMO and YBCO with a structurally sharp interface, represent a good system for investigating spin diffusion into HTSC films. In such a system the spin diffusion length has been determined experimentally by Soltan et. al[86]. From measurements of the zero-field cooled magnetization $M(T)$ the transition temperature T_c of the YBCO film could be extracted. Investigating bilayers with a fixed thickness of 50 nm LCMO but with varying thickness d of the YBCO layer from 20 up to 100 nm a dependence of T_c on the thickness of YBCO was found, see Fig. 4.10. The result is a
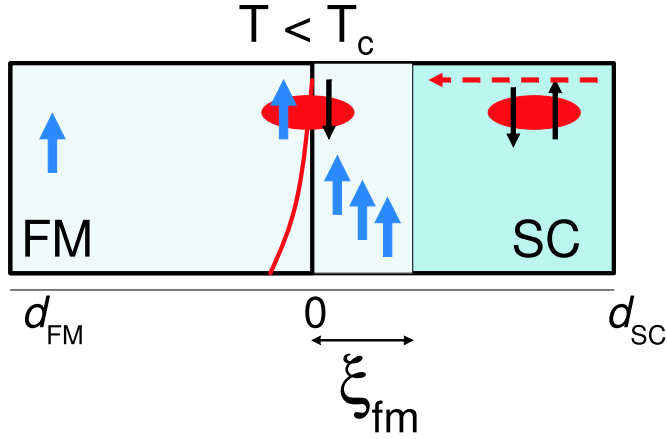
Figure 4.9: Sketch of the interface between a ferromagnet and a superconductor showing the order parameter. The spin-polarized quasiparticle quenches the order parameter to penetrate into the ferromagnet and also diffuses into the superconductor up to the dissuasion length ξ_{fm}. From S. Soltan[101].

strong decrease of T_c for the bilayers containing thin YBCO layers of less than 30 nm. Further Fig. 4.10 shows a fit to the experimental data using

$$d = \alpha \xi_{FM} \cong 3.7 \frac{\alpha m^* \hbar v_F^2}{\Delta(0) \Delta E_{ex} n_{qp}(0) e^2} \frac{\sqrt{T/n_{qp}(T)}}{\sqrt[4]{1 - T/T_c}}, \qquad (4.2)$$

with the quasiparticle density n_{qp} as only free parameter and m* and e, the electron effective mass and charge[86].

The recovery of T_c in the YBCO layer takes place at about 30 nm as seen in Fig. 4.10. With $\alpha \approx 3$ this results in a spin diffusion length of $\xi_{FM} = d/\alpha \approx 10$ nm. The drop of the transition temperature in LCMO/YBCO bilayers is explained by the diffusion of spin-polarized quasiparticles into the superconductor on a length scale of the spin diffusion length $\xi_{FM} = 10$ nm. Such a small ξ_{FM} was expected since nearly full spin polarization at the Fermi level of LCMO prevents the tunneling of Cooper pairs into the ferromagnetic layer and thus suppresses the proximity effect.

Electronic Interface Phenomena

Modern synthesis methods that allow the growth of metal oxide heterostructures with atomic-scale precision allow detailed studies of electronic interface
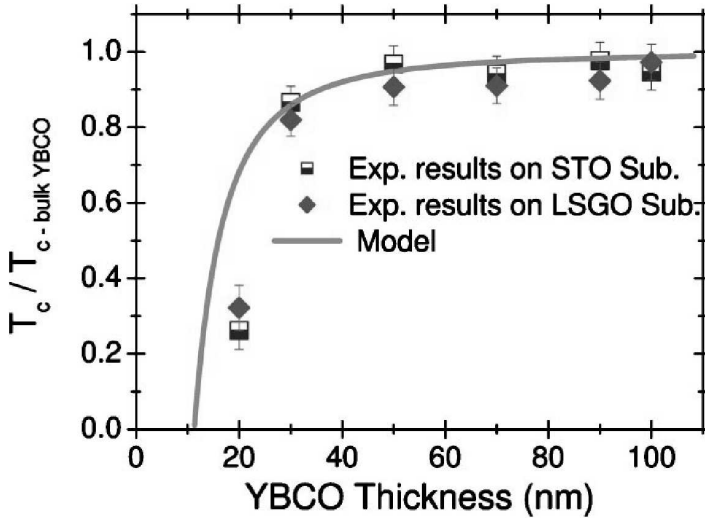
Figure 4.10: Normalized superconducting transition temperature in bilayers with varying YBCO thickness. The solid line represents Eq. (4.2)

phenomena. Especially tri-layers of LCMO and YBCO have been investigated with XMCD (X-ray magnetic circular dichroism) and off-specular neutron reflectometry, by Chakhalian et al.[104] revealing microscopic information of the magnetization profiles both along and perpendicular to the lattice plane.

The XMCD studies showed the occurrence of an uncompensated magnetic moment in the YBCO layer close to the LCMO interface. This moment was found to have antiparallel orientation compared to the ferromagnet, see Fig. 4.11. Together with data from neutron reflectometry this leads to the conclusion that the interface consists of a 10 Å thick layer of LCMO where the ferromagnetic moment is suppressed. Further, this is coupled antiferromagnetically to a 20 Å thick YBCO layer exhibiting large spin polarization. The Cu polarization is thus assumed to be confined to the proximity of the interface.

Due to the atomic arrangement at the interface, the antiferromagnetic interaction between ferromagnet and superconductor has to compete with the antiferromagnetic coupling between the Cu spins. Since this coupling is large, the ferromagnetic polarization of the Cu spins should be an effect of spin canting. At the interface between LCMO and YBCO there is a broken
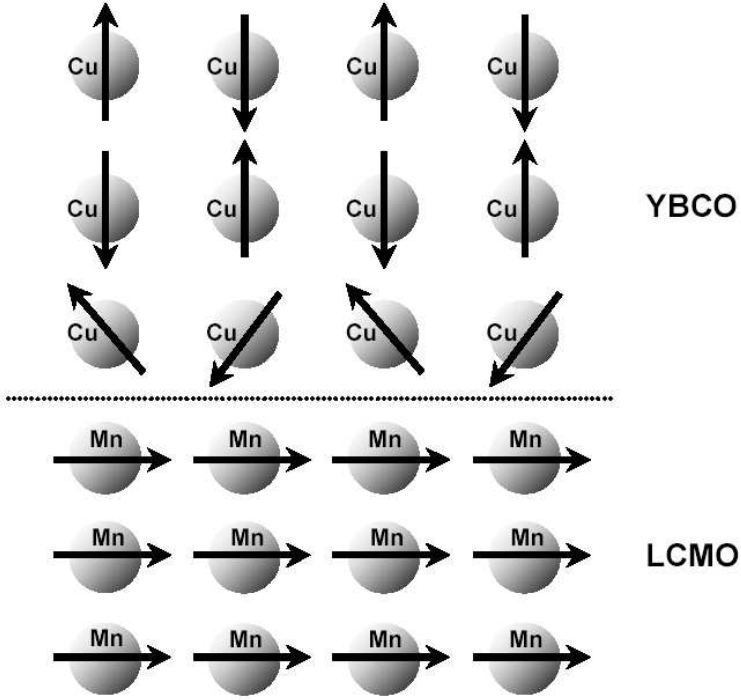
Figure 4.11: Interaction at the interface between superconducting YBCO and ferromagnetic LCMO. Due to the ferromagnet, a magnetic moment is assumed to be induced in the interfacial Cu plane of the YBCO.

lattice symmetry that modifies the orbital physics. Consequently a magnetic moment can be induced in the interfacial Cu plane of the YBCO, oriented antiparallel to the magnetic moment of the Mn in LCMO. This interaction between ferromagnet and superconductor need to take place over a non-magnetic ion, in this case oxygen. In the bulk of LCMO, there is a random occupation of the $d_{x^2-y^2}$ and $d_{3z^2-r^2}$ orbitals. At the interface to YBCO this can change due to the Mn-O-Cu exchange path and the orbitals of the Mn will preferentially occupie the $d_{x^2-y^2}$. This modified orbital occupancy is what is expected to establish an antiferromagnetic interaction resulting in the induction of a magnetic moment in the Cu by spin canting.

Chapter 5

Experimental Techniques

5.1 The Magneto-Optical Faraday-Effect

The magneto-optical Faraday effect can be used to directly image the magnetic flux distribution in superconductors[119, 120]. Especially for superconducting thin films it is possible to calculate the critical current distributions from these images[121].

When shining polarized light through a magneto-optical sensitive material, the plane of polarization is changed in presence of a magnetic field. This phenomenon is called the magneto-optical Faraday effect and has proved to be a useful tool for microscopical imaging of magnetic flux distributions in superconductors. The effect is due to a Zeeman splitting in the magneto-optical sensitive layer. This leads to different probabilities for absorption and emission of two circularly polarized light beams which make up the linearly polarized light. Due to this difference the polarization plane will be rotated in the presence of magnetic field.

In Fig. 5.1 a sketch of the experimental setup used for imaging of magnetic flux distributions in superconducting thin films is shown. On top of the superconductor a magneto-optical sensitive layer is placed with a mirror in between. In the image, the left part of the superconductor is not containing magnetic flux while the right part is in the Shubnikov-phase. The incoming light is plotted at an angle β to the normal of the layer in order to make the view clearer. In real measurements $\beta = 0$ is used. The thickness d of the magneto-optical sensitive layer is chosen so that it makes an multiple plus one quarter of the wavelength of the incoming light. If there is no magnetic field present, this results in complete destructive interference of the two reflected light beams, $\vec{N}$ and $\vec{F}$ since the polarization of $\vec{F}$ which
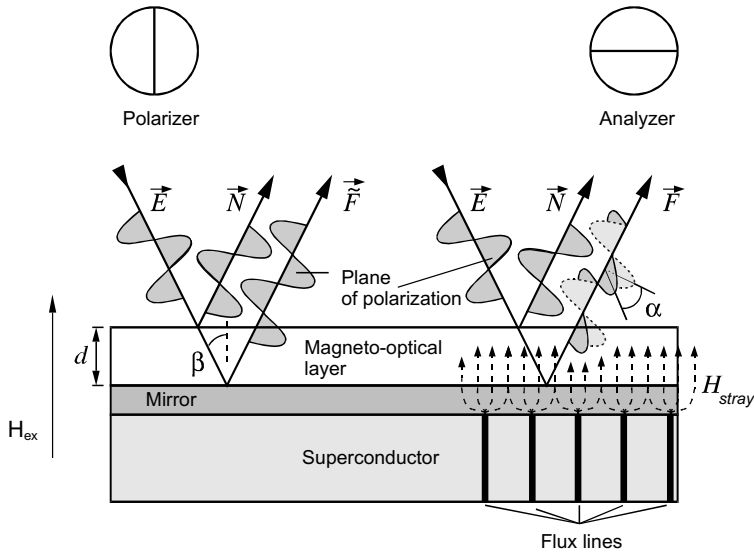
Figure 5.1: Sketch showing how the magneto-optical Faraday effect can be used to image magnetic flux distributions in superconductors.

passes through the magneto-optical layer is not rotated[122]. Those parts of the reflected light which are not rotated will be blocked by an analyzer which has the plane of polarization perpendicular to the incident light. This results in zero transmission in the flux free case.

The situation changes if the superconductor is put in the Shubnikov phase where it contains magnetic flux. The presence of magnetic field causes the plane of polarization to rotate when the polarized light passes through the magneto-optical sensitive layer. Due to the rotation, a light component perpendicular to the incoming light beam will emerge which can pass through the second polarizer. Since the Faraday-effect is directly dependent on the present magnetic field, the intensity of light will be a measure of the local magnetic field. The light intensity at the analyzer is depending on the intensity of the incoming light I_0, the angle α through which the light was rotated, the thickness d of the magneto-optical layer and the absorption coefficient γ,

$$I = I_{off} + I_0 e^{-2\gamma d}\sin^2\alpha \tag{5.1}$$

Stray light, depolarization effects in the objectives as well as errors from polarizer and analyzer are all included in I_{off}.
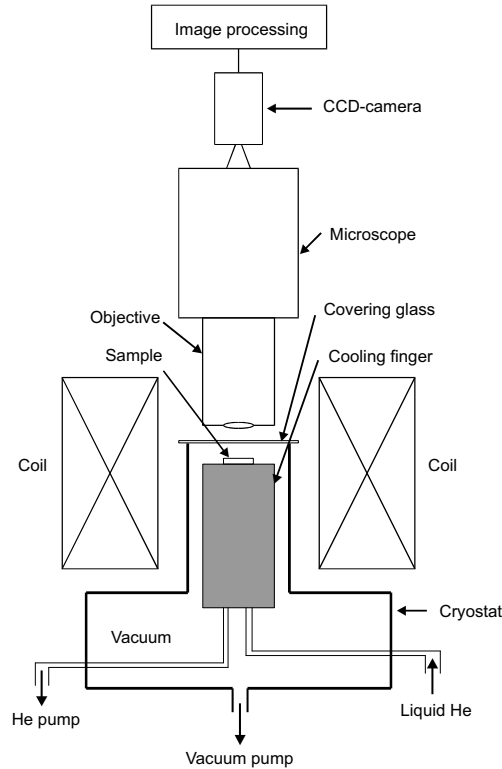
Figure 5.2: Sketch of the setup used for magneto-optical imaging.

5.2 The Experimental Setup

To actually be able to image the magnetic flux distribution in a superconductor the use of a microscope is needed. A sketch of the setup is shown in Fig. 5.2. The superconducting sample is placed on a cooling finger in the cryostat around which a magnetic coil can be placed. A polarized light microscope is used to investigate the sample and a CCD-camera records the images digitally. Finally a PC can be used to further process the images.

Cryostat and Magnet

The superconductor is placed in a helium flow cryostat in which the temperature can be varied from T=5 K up to room temperature. For the used setup there are two cryostats available. The first enables fast cooling but no exact determination of the temperature and is built in the central workshop

of the Max Planck Institute. The temperature is measured with an iron-gold-chromium thermo-element. The second cryostat produced by CryoVac is very slow but has an excellent temperature control, enabled by the use of a temperature controller TIC 304-MA also of CryoVac. This makes it possible to do temperature-dependent measurements with a temperature resolution of up to 0.5 K.

In both cryostats, the superconductor is fixed to the cooling finger with a heat conducting grease. The sample chamber is covered with a glass plate made of 2 mm thick low-stress suprasil glass which only has a very small Faraday rotation. The cooling is carried out by pumping liquid helium through the cooling finger. A valve is regulating the rate of flow and together with a heater, the temperature can be regulated. The sample chamber is evacuated by a rotary pump and a turbo pump for better isolation and to avoid condensation of air onto cover glass, sample and magneto-optical sensitive layer.

A magnetic field is generated by a copper-air coil where the axis of the coil is parallel to the light beam and perpendicular to the sample surface. The coil is supplied with electric current from a current constant EMS-100-50-380-D-LB-10 of Electronic Measurements Inc. The magnetic field depends on the current through a proportionality of 8 mT/A. With this coil it is possible to achieve magnetic flux densities of up to $B_{ext} = 500$ mT but for longer times not more than $B_{ext} = 150$ mT should be used.

Polarization Microscope

The polarization light microscope consists of a commercial microscope, Polyvar Met from the company Reicher Jung, together with a mercury vapor lamp HBO 200 used as light source. The power of the lamp is 200 Watt and it is supplied with stabilized DC-voltage in order to get a light intensity that vary as little as possible with time. The light from the mercury vapor lamp is passing through an edge filter. This is screening the part of the spectrum with wavelengths above $\lambda = 475$ nm and so increases the lateral resolution.

Polarizer and analyzer are adjusted separately. The possibility of twofold regulation makes it possible to correct anisotropic depolarization effects that might appear for example from the switching mirror.

The objectives used are made from low stress glass to further minimize depolarization effects. By combination of different oculars and objectives it is possible to achieve magnifications between 20 and 2000 times.
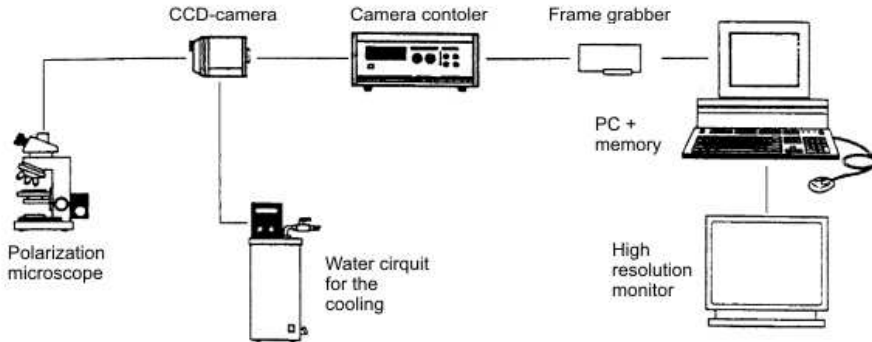
Figure 5.3: Sketch of the setup used for image processing.

CCD-Camera and Image Processing

Recording of the light intensity distribution is done with a CCD-camera (Charge-Coupled Device) type C4880 from Hamamatsu. To reduce noise, the cameras CCD-chip is cooled to -30 °C by a Peltier cooling element. The resolution of the camera is 1000 times 1018 image points with a gray scale depth of 12 Bit per image point. This results in relative intensities from 0 up to 4095. The camera is controlled by a separate camera controller that digitizes the images and sends them to a PC-card (Advanced Frame Grabber Board from the company Imaging Technologies Inc.), see Fig. 5.3. With a PC the images can be saved and further processed. Controlling the CCD-camera and imaging the digital images is made with the commercial program Hipic 3.10 of the company Hamamatsu.

5.3 Magneto-Optical Sensitive Layers

To be able to image the magnetic flux distribution a magneto-optical sensitive layer is needed which has a high Verdets constant that leads to a large Faraday rotation. To be able to do temperature-dependent measurements it is also necessary to use a material were Verdets constant does not vary with temperature. Ferrimagnetic iron garnet films do fulfill these requirements and are thus used as field sensing layers. Iron garnets are compounds of the form $\{Me^{3+}\}_3 [Fe^{3+}]_2 (Fe^{3+})_3 O_{12}^{2-}$. The iron garnet is ferrimagnetic if $\{Me^{3+}\}$ is diamagnetic, for example Lu^{3+} or Y^{3+}. The spontaneous magnetization comes from the different magnetization in the sub lattices of $[Fe^{3+}]_2$ and $(Fe^{3+})_3$. It is important to have magneto-optical iron garnets with a

very low density of defects which can be achieved by producing them as thin films on gallium-gadolinium garnet substrates using liquid phase epitaxy. High-temperature superconductors absorb visible light which makes it impossible to do measurements in transmission. Instead a couple of hundred nm of vapor deposited metal is added as a reflexion layer. The resulting multilayer is usually called "indicator". In measurements the indicator is placed with the reflecting layer on top of the superconductor and so enables measurements in reflexion.

The iron garnet films have an inplane magnetization which means the Faraday effect is measured through the rotation of the magnetization out of the film plane. This make it possible to make a continuous, quantitative determination of the local magnetic flux.

The indicators used in this work are iron garnets from the company Gamma Scientific Production in Russia. An image of the cross section of the indicator made by a light microscope is seen in Fig. 5.4. As seen, the indicator consists of a 500 μm thick substrate made of Gadolinium garnet(Gd_3Ga_5O12), covered with a layer of 6.4 μm of the ferrimagnetic iron garnet which is made from the elements, Fe, Ga, Lu , Bi and O. Finally a 0.4 μm thick reflection layer made of titanium is put on top of all. Such an indicator has a lateral resolution of $3-5$ μm[123] which is mainly limited by the distance between the sample surface and the iron garnet layer.
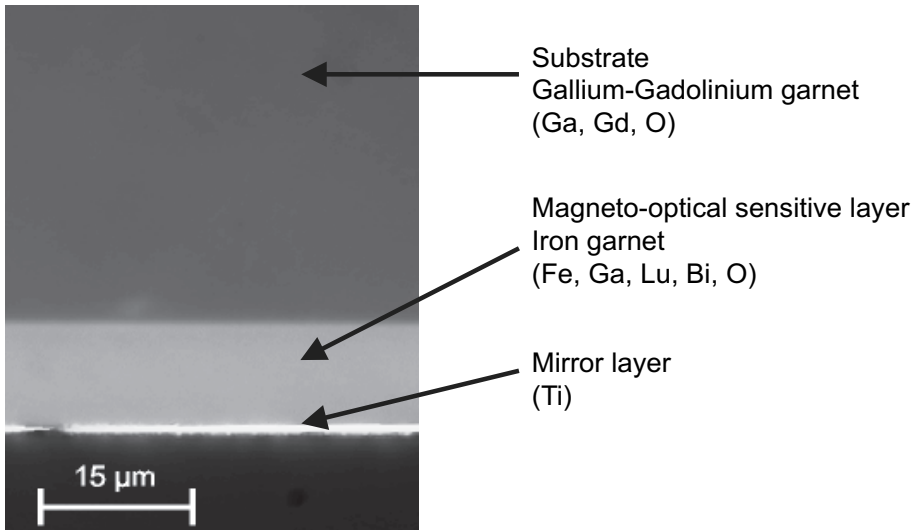

Figure 5.4: Crtoss-sectional image of the indicator made by light microscope

5.4 Magneto-Optical Imaging

The indicator is used to directly image the magnetic flux in superconducting thin films. Three thus obtained images of the flux distribution in different external magnetic fields are seen in Fig. 5.5. The images are typical for isotropic superconductors with quadratic shape. The film imaged is a 200 nm thick YBCO thin film. In all images the gray scale refers to high magnetic flux where the contrast is bright and to zero magnetic field where is black. The film has been cooled down in zero magnetic field to a temperature of $T = 10$ K. Then a small external field of $B = 30$ mT was turned on and the first image taken. It shows how the magnetic flux starts to penetrate into the film from the edges, while the interior still stay in the Meissner state. The second image is taken at $B = 100$ mT, where the film is fully penetrated by flux. Finally the external field is turned of and the third image taken at $B = 0$ mT. The images are acquired after waiting several minutes to take care of relaxation processes of the vortices[124]. Especially the white lines in the last image shows the pinned magnetic flux in the film. The black lines, in the second image, that go from the corners of the sample into the middle are called d^+-lines and are depending on the geometry.

To do more detailed studies of the superconducting properties it is desirable to convert the measured light intensities into quantified flux densities. The relation between magnetic flux and Faraday-rotation is made via the angle ϕ. It determines the angle through which the spontaneous magnetization M_s in the indicator is rotated out of the film plane. The relation
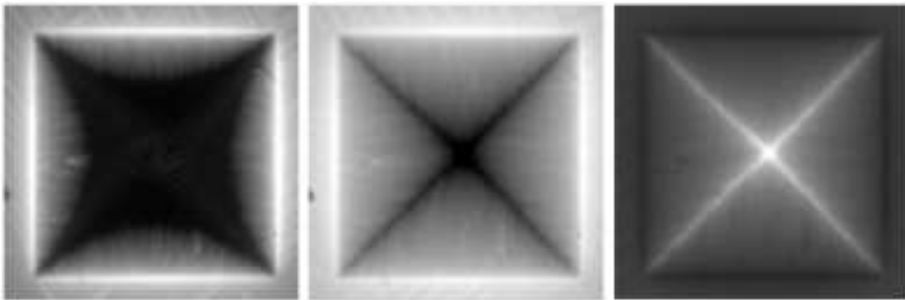

Figure 5.5: Magneto-optical images showing the magnetic flux entering a quadratic YBCO thin film. In the two first images the magnetic field is $B = 30$ mT and $B = 100$ mT respectively while the last image is taken in the remanent state with $B = 0$ mT.

between ϕ and the local magnetic field H can be written,

$$\phi = \arctan \frac{\mu_0 H}{B_k}, \tag{5.2}$$

with B_k being the anisotropic field intensity of the iron garnet which for the used iron garnet indicator is $B_k \approx 220$ mT. The Faraday-rotation α is proportional to the field perpendicular to the layer[123],

$$\alpha = cM_\perp = cM_s \sin\phi = cM_s \sin(\arctan \frac{\mu_0 H}{B_k}). \tag{5.3}$$

This makes cM_s an angular proportionality constant. This together with Eq. (5.1) makes it possible to determine the relation between the measured intensity I and the magnetic field H,

$$I = I_{\text{off}} + I_0 \sin^2(cM_s \sin(\arctan \frac{\mu_0 H}{B_k})). \tag{5.4}$$

The parameters cM_s, I_0 and I_{off} can only be determined numerically by fitting the function to experimental data.

Calibration of the Light Intensity

To get a quantitative image of the magnetic flux in the sample, the measured light intensities $I_{x,y}$, have to be converted into magnetic flux distributions $B_z(x,y)$. To do so Eq. (5.4) is rewritten as,

$$B_z = B_k \tan\left(\arcsin\left(\frac{1}{cM_s} \arcsin\left(\sqrt{\frac{I - I_{\text{off}}}{I_0}}\right) + \alpha_0\right)\right), \tag{5.5}$$

where α_0 is the deviation of the polarizer and analyzer from the exactly crossed 90 ° position. This additional parameter is added since experiments are usually not performed with exactly crossed alignment which might result in vertical tangents causing unwanted ambiguities in the calibration function. This means the following fitting parameters have to be determined: α_0, cM_s, I_0 and I_{off}. The intensity distribution of the incoming light is given by I_0 and is varying substantially with the lateral position in the experiment. The intensity of the incoming light can in a first approximation be described by a Gauss distribution. In the process of analyzing the measurements this variation is taken care of by the subtraction of an image taken in the state of $B_z(x,y) = 0$. As long as the magnetic fields are not too large this makes a sufficiently good correction to the local variation of the light intensity. The

parameter I_0 describes the transmission of polarizer and analyzer by exactly crossed alignment. It is dependent on the used equipment but is also closely connected to the alignment of polarizer and analyzer and thus to α_0 and must be determined separately for each measurement.

For calibration the light intensities are determined for different external magnetic fields. The so obtained pairs of variables I, B_z can be used to make a fit of the function Eq. (5.5). Such a calibration curve is seen in Fig. 5.6. Here, the variables I, B_z are seen as crosses and the fitted function as solid line. For calibration a measurement has been performed making images at the same magnetic field in increasing and decreasing external magnetic field in order to take care of stray fields of the superconductor. The influence of the superconductor is seen in that the crosses in Fig. 5.6 are shifted to the right and left at each point. After all parameters have been determined it
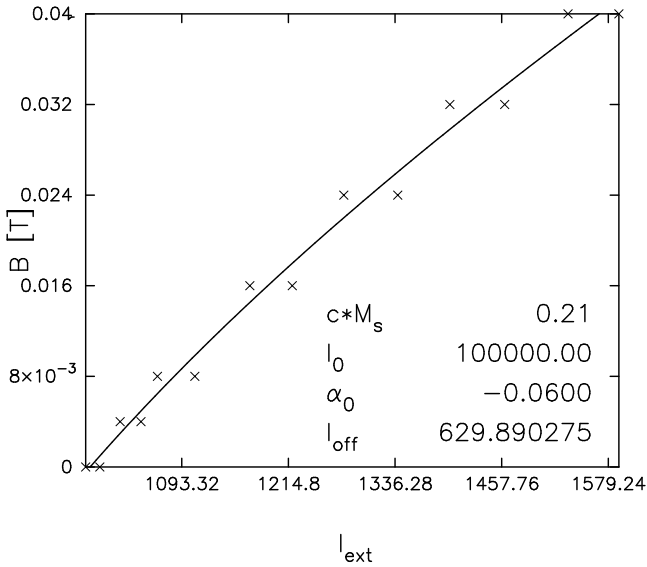
Figure 5.6: Relation between light intensity and magnetic flux density. Experimental values and fit of the calibration function $B_z(I)$.(solid line)
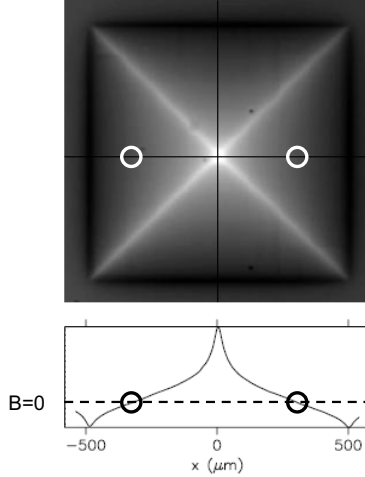
Figure 5.7: Magnetic flux distribution in the remanent state determined from Fig. 5.5 c) using $B_z(I)$. The profile is taken along the black line. Indicated with circles are areas with low flux density.

is possible to calculate the light intensity distribution $I(x,y)$ into a magnetic flux distribution $B(x,y)$. Such an image calculated from the light intensities in Fig. 5.5 is shown in Fig. 5.7. It shows the magnetic flux distribution in the film and a profile taken along the black line. Circles indicate the regions around $B = 0$ where the flux density is particularly low and flux-line flux-line distances are particularly large. This leads to only small interactions between the flux lines. The images of the magnetic flux distribution in a superconductor have a lateral resolution of about 1 μm, where the optic is the limiting factor.

5.5   From Magnetic Flux to Critical Currents

The relation between a critical current density distribution $\mathbf{j(r)}$ and magnetic flux density distribution $\mathbf{B(r)}$ is given by the law of Biot and Savart,

$$\mathbf{B(r)} = \mu_0 \mathbf{H}_{ex} + \mu_0 \int_V \frac{\mathbf{j(r')} \times (\mathbf{r} - \mathbf{r'})}{4\pi \left| \mathbf{r} - \mathbf{r'} \right|^3} d^3 r'. \tag{5.6}$$

To determine the critical current $j(r)$, an inversion of Eq. (5.6) has to be performed. But since the known variable determined from the measurement is the scalar field $B_z(x,y)$ only the z-component of the induction field $\mathbf{B}$ is

determined and thus no information can be extracted for possible dependences in the z-direction. For the calculations it is necessary to assume the current density along the z-direction to be negligible small, which is nearly exact for the case of thin films. Also all changes in the current densities along the z-direction are neglected, again a very good approximation for HTSC thin films. Any changes in critical current occur on the length scale of λ in type II superconductors and justifies the neglecting of these effects in films with thicknesses of the order of λ and smaller.

With an external magnetic field parallel to the z-direction and two-dimensional current distribution, the law of Biot and Savart can be rewritten as,

$$B_z(\mathbf{r}) = \mu_0 H_{ex} + \mu_0 \int_V \frac{j_x(\mathbf{r}')(y - y') - j_y(\mathbf{r})(x - x')}{4\pi |\mathbf{r} - \mathbf{r}'|^3} d^3 r'. \tag{5.7}$$

Since there are no external contacts to the superconductor the continuity equation is valid for j_x and j_y leading to $\partial_x j_x + \partial_y j_y = 0$. But this still does not make it possible to solve Eq. (5.7) analytically to determine the critical current density. Instead, the use of the translation invariance of the Biot and Savart's law, which allows the periodic continuation of the flux distribution is used and makes it possible to do the calculations in Fourier space. For this a scalar current potential $g(x, y)$ is introduced,

$$\mathbf{j}(x, y) = \nabla \times (g(x, y)\mathbf{e}_z) \tag{5.8}$$

with which Biot-Savarts law can be written as

$$B_z(\mathbf{r}) = \mu_0 H_{z,ex} + \mu_0 \int_V K_g(\mathbf{r}, \mathbf{r}') g(x', y') d^3 r', \tag{5.9}$$

where the kernel is given by,

$$K_g(\mathbf{r}, \mathbf{r}') = \frac{1}{4\pi} \frac{2(z - z')^2 - (x - x')^2 - (y - y')^2}{[(x - x')^2 + (y - y')^2 + (z - z')^2]^{\frac{5}{2}}}. \tag{5.10}$$

In Fourier space we have after a two dimensional Fourier transformation,

$$\tilde{B}_z(k_x, k_y) = \int \int dx dy B_z(x, y) e^{i(k_x x + k_y y)} \tag{5.11}$$

and

$$\tilde{g}(k_x, k_y) = \int \int dx dy g(x, y) e^{i(k_x x + k_y y)}. \tag{5.12}$$

Using the convolution theorem Eq. (5.9) in Fourier space turns into

$$\tilde{B}_z(k_x, k_y) = \mu_0 \tilde{K}_g(k_x, k_y) \tilde{g}(k_x, k_y), \tag{5.13}$$

where the Fourier transformation of the integral kernel can be calculated,

$$\tilde{K}_g(k_x, k_y) = e^{-kh}\sinh(\frac{kd}{2}), \tag{5.14}$$

with $k = \sqrt{k_x^2 + k_y^2}$. Here both the thickness of the film d and the distance h between sample surface and indicator is used. It is now possible to calculate the current potential in Fourier space using Eq. (5.9),

$$\tilde{g}(k_x, k_y) = \frac{1}{\mu_0}\frac{\tilde{B}_z(k_x, k_y)}{\tilde{K}_g(k)}. \tag{5.15}$$

A back transformation into real space is done and finally the sought current density components j_x and j_y are calculated through derivation of the scalar current potential $g(x, y)$,

$$j_x = \frac{\partial}{\partial_y}g(x, y), \tag{5.16}$$

$$j_y = -\frac{\partial}{\partial_x}g(x, y). \tag{5.17}$$

When applying this algorithm to experimental data there a problem occurs due to the noise. The problem is emerge in the division in Eq. (5.15), since it works as a high pass filter, amplifying the high frequency noise. This may then cover the actual information. To solve this problem a so called Hanning window is used that cut off the k-vectors with high frequency[121]. This procedure slightly reduces the lateral resolution, but still delivers the best results.

A problem that is not taken care of in the described algorithm are magnetic fields induced by supercurrents in the superconducting film, which have been neglected this far. The currents induce an in-plane magnetic field, perpendicular to the flux lines. This field rotates the magnetization of the indicator back into the plane and thus leads to errors in the determination of the current densities, especially for high currents. By an iteration process this error can be corrected[125]. This is done by including the magnetic flux density in the plane B_{xy} into Eq. (5.5) resulting in,

$$B_z = \left(1 + \frac{B_{xy}}{B_k}\right)B_k\tan\left(\arcsin\left(\frac{1}{cM_s}\arcsin\left(\sqrt{\frac{I - I_{off}}{I_0}}\right) + \alpha_0\right)\right). \tag{5.18}$$

The whole calculation of the critical current density is now iterated several times, starting with a $B_{xy} = 0$. For each iteration a new B_{xy} is calculated
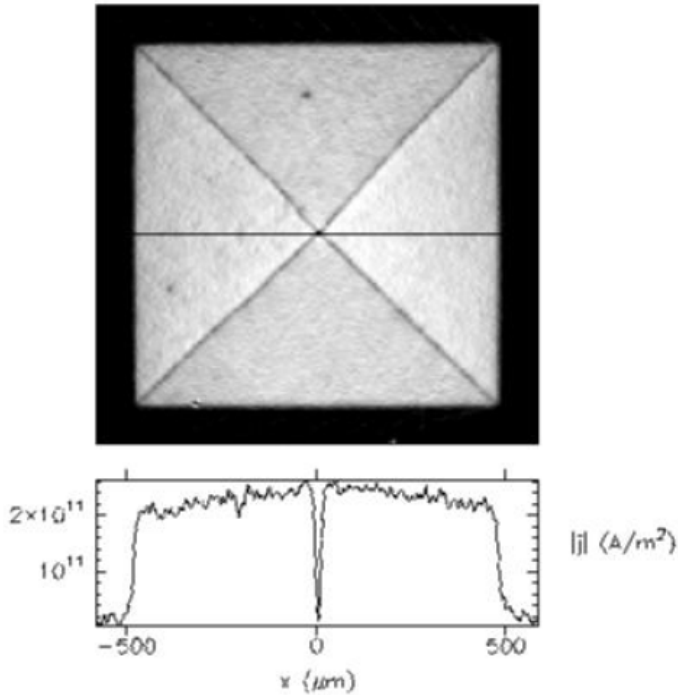
Figure 5.8: Typical image of the critical current density distribution in the remanent state for a square shaped superconducting thin film. The distribution was calculated from the image in Fig. 5.7 using the method described in the text. The current profile is taken along the black line.

using the law of Biot and Savart, Eq. (5.9) and inserted into Eq. (5.18). The iteration is continued until convergence is achieved.

5.6 SQUID

A Superconducting QUantum Interference Device (SQUID) can measure magnetic flux extremely precise. It can detect changes in magnetic field down to the order of 1 fT. It consists of a superconducting ring, which is disrupted on two places by normal conducting or insulating material, see Fig. 5.9. Thus, there are two Josephson junctions formed making the active part of the SQUID. If a bias current is sent through the SQUID, which is larger than the critical current of the two Josephson junctions, a voltage will be induced. Owing to the special properties of the Josephson junction, this
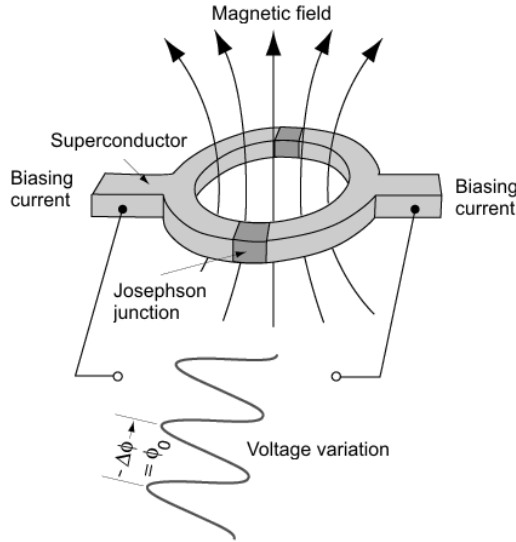
Figure 5.9: The squid consists of two superconductors separated by thin insulators which make two parallel Josephson junctions.

voltage signal will be a periodic function of the magnetic flux threading the SQUID ring. The voltage will be dependent not only on the bias current but also on a supercurrent that is induced in the ring in the presence of the magnetic field. If the magnetic field changes, the supercurrent in the ring will change and thereby also the voltage. The voltage signal can be modulated with lock-in detector linearizing the voltage to flux relation.

In a real system used for measurements, the SQUID is placed inside a superconducting magnetic shield and is cooled with liquid helium. Since the SQUID is so sensitive to magnetic fields, there are many sources for noise like the magnetic field from earth or from electrical cables. One way to suppress these are to put 2 or more SQUIDs beside each other to form gradiometer structures[3].

5.7   Temperature-Dependent Measurements

Temperature-dependent measurements of the local magnetic flux and critical current distributions can be performed using the magneto-optical technique. The measurements are usually performed in the remanent state after zero-field cooling. By making images during a slow and steady increase in tem-

perature this delivers the temperature dependence of the pinned magnetic flux distribution. Since it is important to reduce temperature fluctuations and keep the temperature gain slow enough, the increase in temperature need to be controlled by hand. Thereby either only the heater is used by fixed helium flow or the helium flow is reduced by fixed heating. The available digital temperature controllers can not react fast enough on changes in heat capacities which directly influences the controlling parameters. This mean that the answer of the system to changes is not constant but varies with temperature, making the temperature controll difficult.

The temperature dependence of the magnetization in a square shaped isotropic superconducting thin film has been measured both with the magneto-optical technique and with a SQUID. The magneto-optically measured current distribution allows the calculation of the integral magnetization that can be directly compared to magnetization measurements performed with a SQUID magnetometer. A direct comparison of results from the two measurement techniques can be seen in Fig. 5.10, showing excellent agreement for all temperatures.
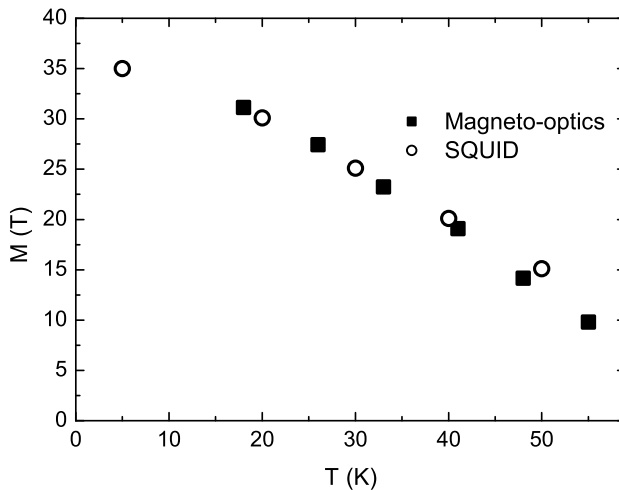

Figure 5.10: Comparison of the magneto-optical technique and the SQUID for a large temperature range.

Chapter 6

Critical Currents in Vicinal YBCO Thin Films

To enhance flux pinning and critical currents in thin films of high-temperature superconductors, it is important to understand the mechanisms that lead to the depinning of a flux line. A suitable method to obtain insight into flux pinning properties is the detailed analysis of the temperature-dependent critical current densities[126, 127, 128, 129, 111, 130, 131, 132]. This can be effectively performed by quantitative magneto-optics, allowing direct imaging of magnetic flux density distribution in superconducting thin films and the determination of the local critical current densities[8]. The simplest system for these kind of experiments should have few microstructural inhomogeneities, since those can act as obstacles for the current flow[130] and make analysis more difficult. A homogeneous film can be manufactured using a vicinal cut substrate, due to the special growth mode occurring because of the surface steps[80].

Thin films of optimally doped YBCO were grown on 5×5 mm^2 vicinal STO (106) substrates, see sketch in Fig. 6.1. The miscut of the substrate towards the (100) direction is $\theta = 9.46°$. This produces steps with a width $w = a_{STO}/tan\theta = 11$ nm where $a_{STO} = 3.905$ Å is the lattice constant of STO[131]. This results in very straight steps with heights of one unit cell[74, 79]. The YBCO film is 150 nm thick and is grown with pulsed laser deposition. Due to the steps in the substrate a step flow growth is occurring resulting in a very smooth film nearly without grain boundaries along the steps. Between the steps an array of nearly parallel antiphase boundaries is formed. Because of the nearly defect free growth, the APBs are expected to dominate as pinning sites[127].
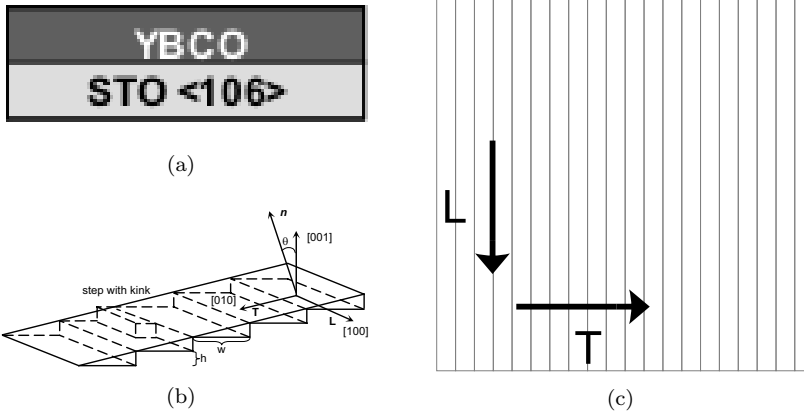
Figure 6.1: YBCO grown on vicinal cut STO, (a) sketch of the sample structure, (b) sketch of the substrate surface and (c) the Longitudinal(L) and Transversal(T) directions relative to the substrate steps.

6.1   Magnetic Flux and Critical Current Distributions

The penetration of magnetic flux into these films is anisotropic[74, 83, 131] as can be seen in Fig. 6.2. Flux penetrates more easily along the steps of the substrate than across the steps where the anti phase boundaries act as good pinning centers. The gray-scale images represent B_z, the flux density component perpendicular to the surface of the film. Bright parts refer to a high local magnetic flux density of about 20 mT. The images were taken in perpendicular magnetic field after zero-field cooling a) in an increasing field of $B = 16$ mT, b) in the remanent state. The remanent state is produced by cooling the film down to $T = 6.5$ K after which a magnetic field of $B = 250$ T is turned on for a few seconds to fully penetrate the film. The magnetic field is then turned off to put the film into the remanent state. Before starting the measurement a constant delay time of about 10 s was used to take care of the relaxation processes[124]. The image seen in Fig. 6.2 shows the pinned magnetic flux in the film at $T = 6.5$ K.

From images of the flux distribution it is possible to calculate the critical current distribution in the film by an inversion of the Biot-Savart law in two dimensions[8]. This processing is described in detail in Chapter 5.5. An image of the modulus of the critical current distribution at $T = 6.5$ K is shown in Fig. 6.3. The gray scale refers to current densities from $j_c = 0$ A/m^2, black, up to $j_c = 5 \times 10^{11}$ A/m^2, white. The strong anisotropy of
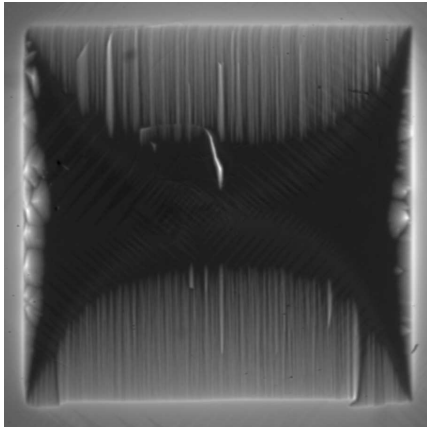
(a) Magnetic flux distribution in an increasing magnetic field of $B = 16$ mT.
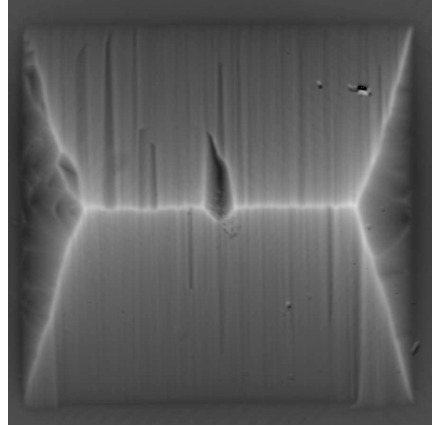
(b) Magnetic flux distribution in the remanent state.

Figure 6.2: Magnetic flux distributions in a vicinal YBCO film at $T = 6.5$ K.

j_c due to the substrate steps is clearly seen as different current densities in regions with different current directions, higher in the L-direction (light gray), lower in the T-direction (dark gray). At this temperature of $T = 6.5$ K the different directions show averaged critical current densities of $j_{c,L} = 3.3 \cdot 10^{11}$ A/m^2 and $j_{c,T} = 1.3 \cdot 10^{11}$ A/m^2 respectively. These are typical values for high quality 150 nm thick YBCO films grown on vicinal STO[82, 8]. Below the image a current profile is shown which has been taken along the solid black line.

Two macroscopic irregularities in the film are marked out in the image. At (a), there is a scratch in the film resulting in an area which can not be crossed by the supercurrents. The currents are forced to flow around the scratch resulting in components along the APBs and, thus, in an enhanced current density in that area. The white spot marked with (b) refers to a defect in the detector layer and is not related to superconducting properties. Apart from these the film is nearly defect free and of a high quality supported by the high values for the critical current densities especially in the L-direction.

In Fig. 6.4 the magnetic flux distribution in the remanent state is shown again, but here with addition of the calculated current stream lines. It shows how the current is flowing in nicely shaped rectangular loops parallel to the film edges. In Fig. 6.1b) two current directions are indicated, the

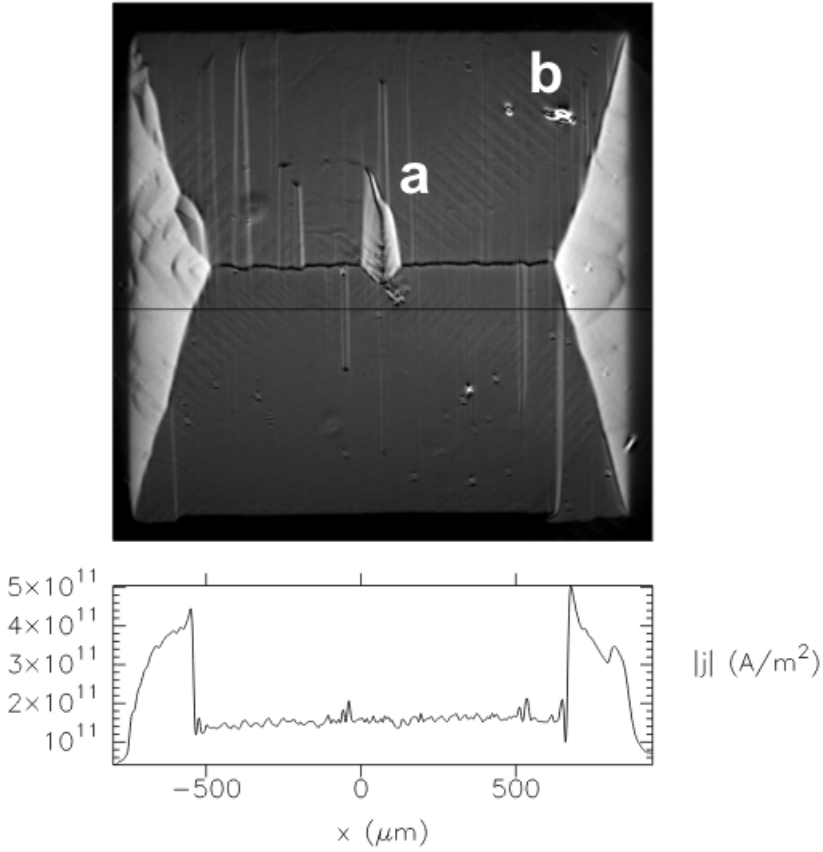Longitudinal (L) along the steps and the Transversal (T) across the steps.

Figure 6.3: The critical current distribution in the film at $T = 6.5$ K. (a) and (b) indicate defects in the film. The current density profile is taken along the black line.
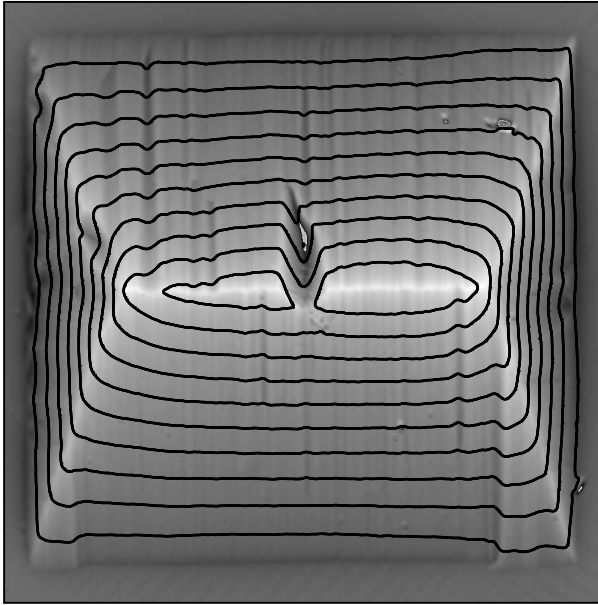
Figure 6.4: The magnetic flux distribution in the remanent state. Also seen is the calculated current stream lines.

*

6.2   Temperature Dependences of Magnetic Flux and Critical Current Distributions

A good method to distinguish between different mechanisms limiting the current transport is given by the detailed analysis of the temperature dependence of the critical current density[126, 127, 128, 129, 111, 130, 131, 132]. The first step in these investigations is to do a temperature-dependent measurement of the magnetic flux distribution in the film, as described in Chapter 5.7. The experiment was done in the remanent state by increasing the temperature, from 6.5 K up to above $T_c = 91$ K. Images are taken at steps of 1 Kelvin, while slowly heating the sample up to above T_c. To minimize the relaxation processes of the vortices, a constant delay time of 10 s was used before acquiring each image. In Fig. 6.5 such a sequence of images showing the temperature dependence of the magnetic flux distribution in the film is seen. The images seen are taken between 6.5 K and 80 K.   Clearly seen is how the anisotropy of the film is decreasing with increasing temperature. Also the intensity is decreasing meaning that more and more flux is leaving the sample as the temperature is increasing.

For each of the measured images of the magnetic flux distribution, the critical current distribution is calculated. This results in a series of images showing the distribution of j_c at each K[133]. An array of such images is presented in Fig. 6.6 at increasing temperatures from $T = 6.5$ K (a) up to $T = 89$ K (f). With increasing temperature one immediately sees how the current anisotropy is decreasing to disappear near $T_c = 91$ K. In the image Fig. 6.6(f), taken at $T = 89$ K only 2 K below T_c, the angle between the discontinuity lines and the film edge has increased and almost a cross is formed like in films grown on flat substrates. Also seen in the images is an overall decrease in contrast relating to the decrease of the critical current with increasing temperature. At 89 K the critical current has been reduced to about $j_c = 8 \cdot 10^9$ A/m^2 and the difference between the two directions is very small. This means, that the anisotropy of the film has almost disappeared at this temperature close to T_c.

From these images values for the critical current can be determined for each current direction separately for all the measured temperatures from $T = 6.5$ K to $T = 90$ K. The critical currents are averaged over carefully chosen areas with side lengths of several 100 μm for each current direction. The areas are chosen around the $B = 0$ line that necessarily appears in the remanent state[134]. This in order to take care of any magnetic field dependence of the critical current due to flux-line flux-line interactions.
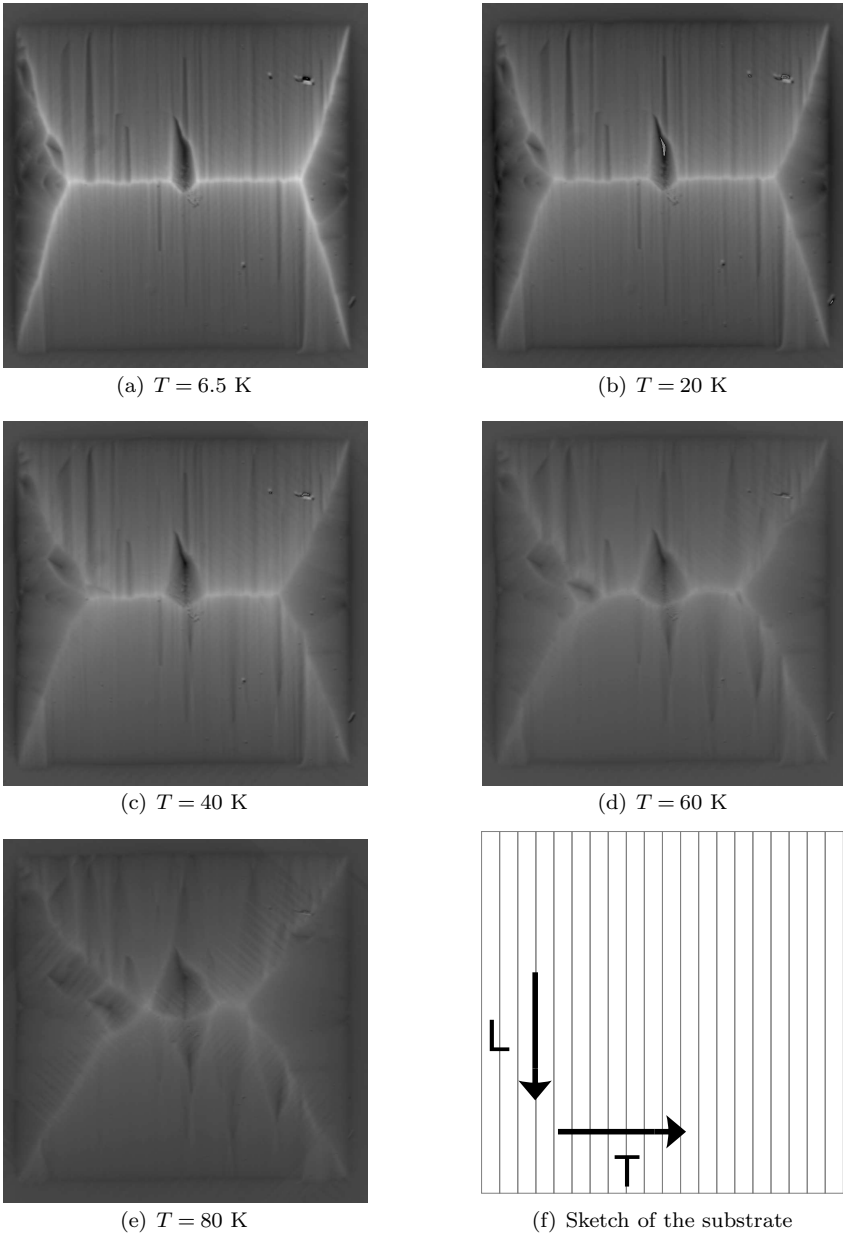
(a) $T = 6.5$ K

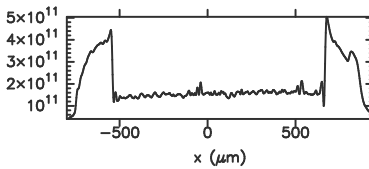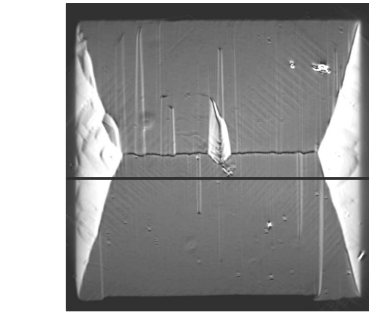(b) $T = 20$ K

(c) $T = 40$ K
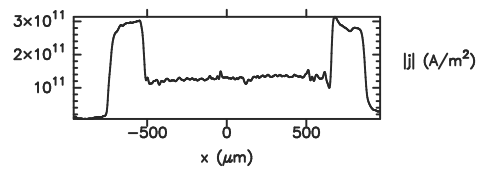

(d) $T = 60$ K

(e) $T = 80$ K

(f) Sketch of the substrate

Figure 6.5: The temperature dependence of the magnetic flux distribution in the film.

(a) *T=6.5 K*

(b) *T=20 K*

(e) *T=80 K*

(f) *T=89 K*

(c) *T=40 K*
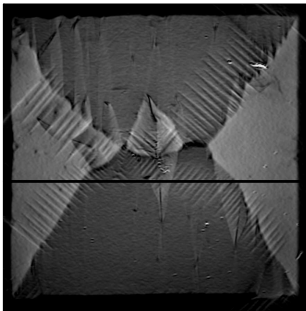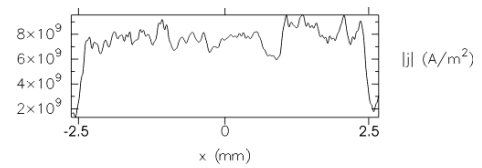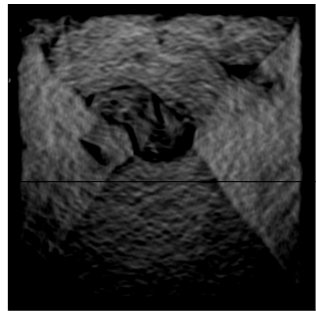
(d) *T=60 K*
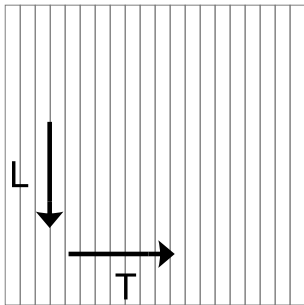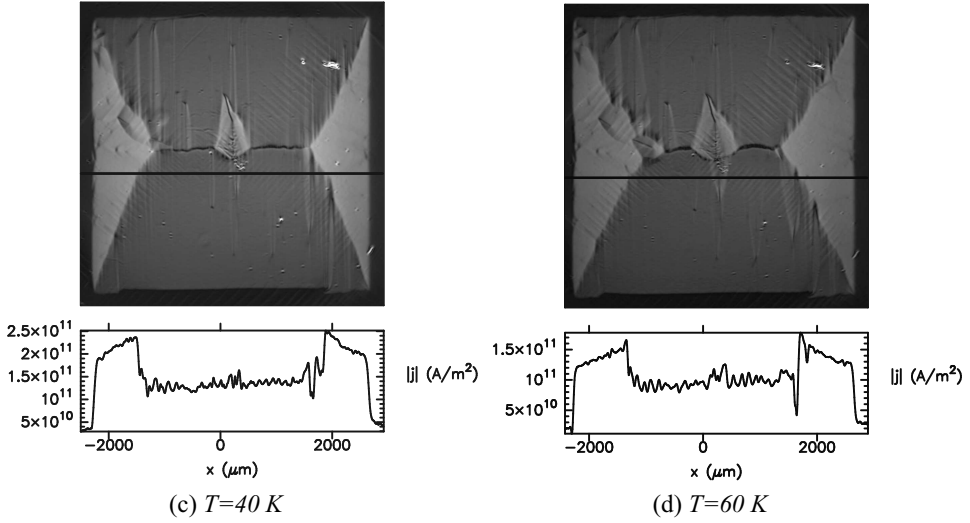
(g) Sketch of substrate, indicating the current directions relative to the steps.
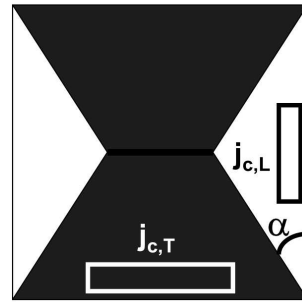
(h) Sketch of the j_c distribution in the film. Seen are the areas were the average values $j_{c,L}$ and $j_{c,T}$ are extracted. Also the angle α is introduced.
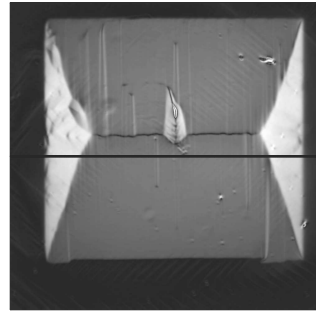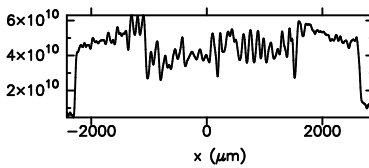
Figure 6.6: The temperature dependence of the critical current distribution in the film.
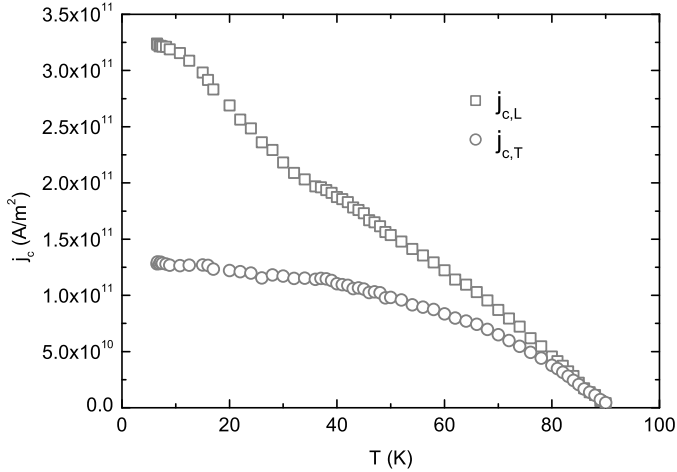
Figure 6.7: Temperature dependence of the critical currents $j_{c,L}$ and $j_{c,T}$ in the vicinal film.

These areas are indicated in Fig. (h), in black for the longitudinal current and in white for the transversal current direction. The carefully obtained temperature dependent values of the critical currents can now be plotted over the temperature as seen in Fig. 6.7, where the longitudinal current is plotted as squares and the transversal as circles. Clearly seen is the completely different behavior of the two current directions[131].

From these data it is also possible to determine T_c. In a first analysis we have a look at the temperature where j_c is vanishing. This temperature for both directions can be estimated by a linear fit to the values at higher temperatures, seen in Fig. 6.8. For both directions values close to $T = 91$ K are found, which means there is no substantial suppression of T_c due to the antiphase boundaries.

A value for the current anisotropy can be calculated as the ratio

$$A_j = \frac{j_{c,L}}{j_{c,T}} \tag{6.1}$$

of the local critical current densities at each measured temperature[8]. The temperature dependence of the current anisotropy A_j is shown in Fig. 6.9 as open squares. Also seen as black solid squares are the geometrically
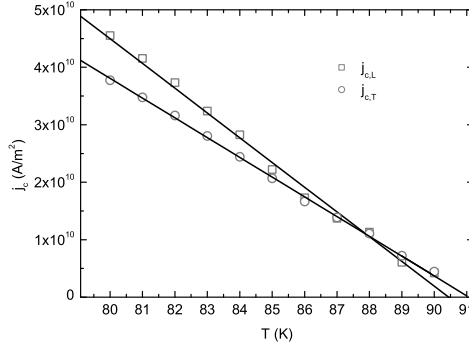
Figure 6.8: Determination of T_c from the temperature dependence of the critical current.

determined anisotropies

$$A_\alpha = \frac{1}{\tan\alpha}. \tag{6.2}$$

These values are calculated using the angle α between the areas with different current directions[8]. The definition of α is indicated in Fig. 6.6 (h). This second estimation is rather rough, since the d-lines separating the dif-
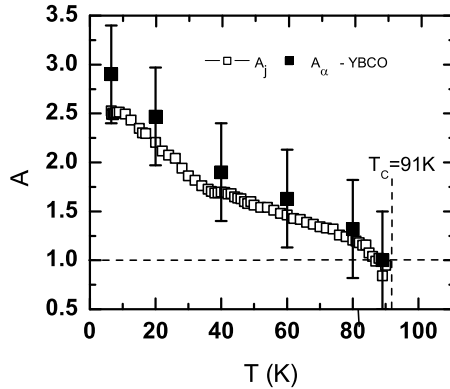
Figure 6.9: Temperature dependence of the current anisotropy Open squares are calculated from the current values, filled squares from the geometry of the critical current distribution.

ferent current areas are not straight lines as in Beans model but instead have a slight curvature. In Beans model the penetrated flux leads to constant j_c-values, resulting in straight d-lines. This is different from what happens in real films where there is a magnetic field dependence of the critical current[135, 8]. From the occurring $B_z = 0$ line, $j_{c,L}$ is decreasing towards the film edge while $j_{c,T}$ is increasing. This together with a not completely homogeneous film leads to the problems in determining the angle α and thus the geometrical anisotropy A_α. Nevertheless, there is an excellent agreement between the anisotropies determined with the two methods. The current anisotropy at low temperatures is $A_j \approx 2.5$ and decreases with increasing temperature to disappear completely at $T_c = 91$ K. This temperature dependence is confirming what could already be predicted by looking at the images of $j_c(T)$.

6.3   Critical Currents Around a Microscopical Defect

As already mentioned in Chapter 6.1 there is a scratch in the film marked with an (a) in Fig. 6.3. The magnetic flux distribution at this macroscopical defect is shown in Fig. 6.10. In (a) for an increasing external magnetic field of $B = 16$ mT, the defect is clearly seen as a bright line. The magnetic flux is penetrating from the top of the image and has already filled the whole defect, while the area around the defect is still flux free and thus remaining black. The image (b) is in the remanent state where the defect is now seen as a dark line surrounded by bright magnetic flux. That it appears dark is because of stray fields from the vertical component of the critical current.
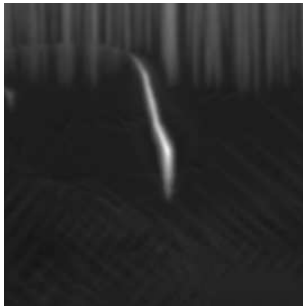
(a) B_z at increasing external field of 16 mT.
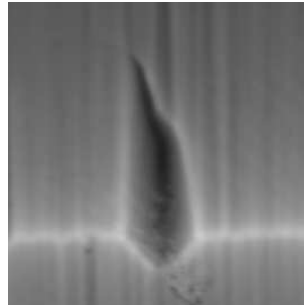
(b) B_z in the remanent state

Figure 6.10: Magnetic flux distributions at a macroscopical defect.

This defect allows the study of which role geometrical constraints have on the current pattern locally. Owing to the presence of the scratch the horizontal current component has to be zero. This leads to a critical current distribution as depicted in more detail in Fig. 6.11 for temperatures between 6.5 K and 80 K. The defect contains a nonsuperconducting area which cannot be crossed by the supercurrents. The currents are forced to flow around the scratch resulting in components along the APBs. This is the bright area seen in the images were the critical current is strongly enhanced. This is a further example of the role of the geometry for the critical currents. With increasing area, that is decreasing current anisotropy, also the shape of the area with longitudinal current at the defect is changing. The area is getting broader and broader while the critical current is further reduced. At $T = 89$ K the defect are hardly to be seen, since the current components along the steps close to the defect is now reduced to a value very close to that for the transversal current.

(a) $T = 6.5$ K   (b) $T = 20$ K   (c) $T = 40$ K

(d) $T = 60$ K   (e) $T = 80$ K   (f) $T = 89$ K
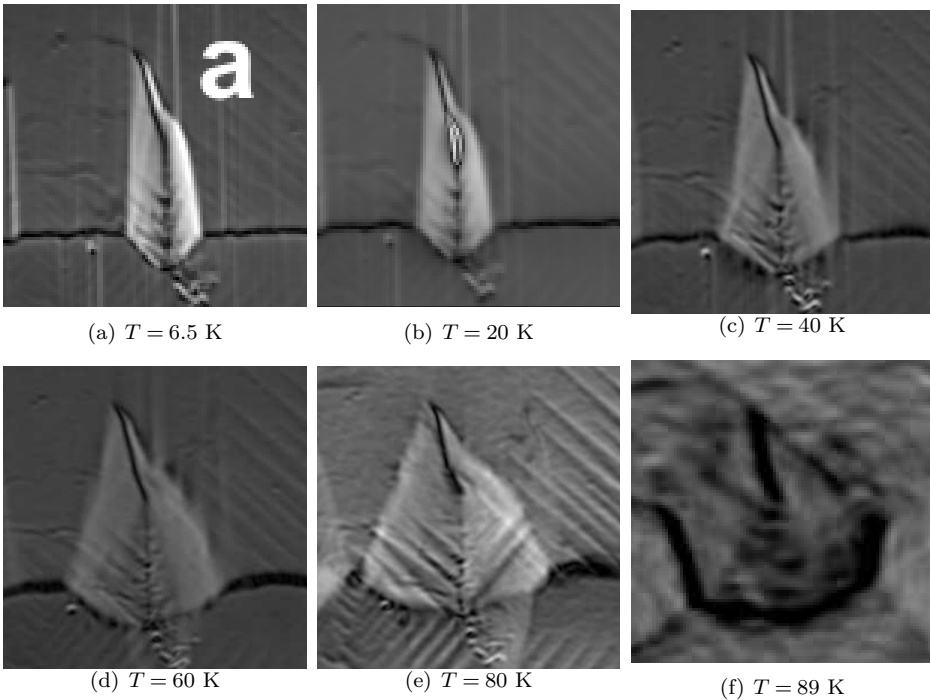
Figure 6.11: Critical current density distributions at a macroscopical defect for temperatures between 6.5 K and 89 K.

Chapter 7

Critical Currents in YBCO/LCMO Bilayers

The critical current in thin superconducting films is determined by the pinning of flux lines at defects and inhomogeneities[2]. The density of growth-induced defects in thin films of high-temperature superconducting materials is already high but to further increase the critical current artificial defects are introduced in order to enhance flux line pinning. Different attempts have been used for influencing the properties of the critical current; structuring of substrates[130, 136, 137], inclusion of precipitates[138], irradiation[139, 140], rare-earth mixing[141, 7], inclusion of nanoparticles[142, 143, 144] or addition of a second interface to a different material[145].

Highly interesting is the addition of an interface to a ferromagnetic layer which is expected to influence the properties of the critical current substantially. The addition of a ferromagnetic layer on top of the superconducting film is expected to give a possibility to explore contributions of magnetic pinning and to enable new insights into the current limiting mechanisms of the superconductor. Thus, hybrid structures consisting of a superconducting and a ferromagnetic layer will be investigated using the same quantitative magneto-optical method as used by the single layer YBCO thin film[8].

Studies of such complicated systems require from the heterostuctures both to have a well defined microstructure and a high-quality interface. The extraordinary homogeneous YBCO thin film grown on a vicinal cut substrate, presented in the last chapter, thus proves to be a suitable choice for the superconducting layer. It has a homogeneous current path along the steps of the substrate but also exhibits a second current path with different microstructural properties across the APBs formed along the steps[80]. This makes it possible to investigate the influence of an additional ferromagnetic layer on two current paths with different microstructure contained in

the same sample. By use of the magneto-optical method this can even be achieved in one measurement. For good coupling between the superconducting and ferromagnetic layer a high quality interface is required that is highly regular both electronically and magnetically. LCMO is a suitable choice as ferromagnet since it has similar crystal structure and lattice parameters as YBCO, enabling epitaxial growth with atomically flat interfaces[100]. The resulting YBCO/LCMO hybrid structures fulfill the requirements for studying coupling effects between superconductor and ferromagnet and especially the behavior of the critical current.

The structure of the studied hybrid structure looks like in Fig. 7.1(a)[146]. The films were grown epitaxially onto vicinal cut SrTiO$_3$ substrates with a nominal vicinal angle $\theta = 9.46$ °, using pulsed laser deposition. The YBCO is optimally doped, 150 nm thick and a bilayer is formed by adding 50 nm LCMO on top of it. The lateral size of the films is 5×5 mm^2. Thus, the microstructure of the superconducting layer must be identical with the YBCO thin film studied in the previous chapter. The only difference is the growth of the ferromagnetic layer on top of the superconductor which is not expected to change the microstructure of the superconductor.

(a) YBCO grown on vicinal cut STO and covered with a layer of ferromagnetic LCMO.

(b) Sketch of the substrate indicating the the longitudinal (L) and transversal (T) directions relative to the substrate steps.
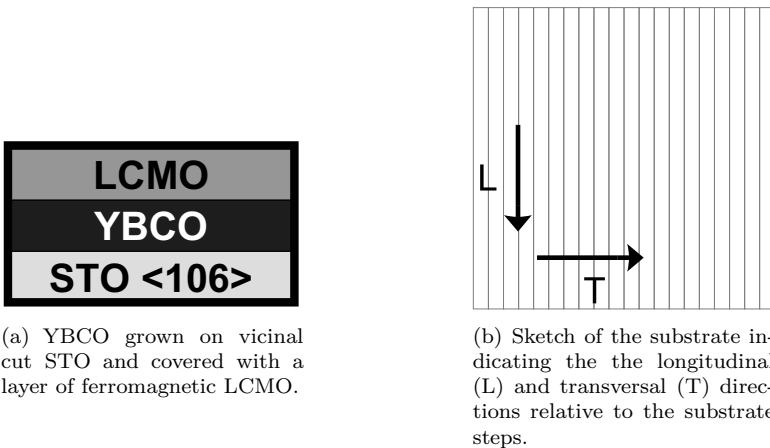
Figure 7.1: Structure of the studied sample.
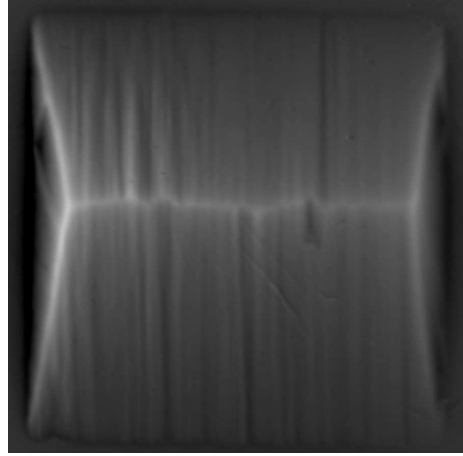
7.1 Magnetic Flux and Current Distributions

The penetration of magnetic flux into these hybrid structures is depicted in Fig. 7.2. The images were taken in perpendicular magnetic field after zero field cooling down to $T = 9$ K, in an increasing field of $B = 3.2$ mT Fig. 7.2(a) and in the remanent state Fig. 7.2(b). The remanent state was produced in the same way as for the single layer. The gray-scale images represent B_z, the flux density component perpendicular to the surface of the film. Bright parts refer to high local magnetic flux of about 20 mT. The procedure of measurement was the same for the two samples and Fig. 7.2(b) shows the pinned magnetic flux in the film at $T = 9$ K. The flux penetration is strongly anisotropic and looks similar to that found in the single layer YBCO thin film, Fig. 6.2. There are some differences though, the flux penetrates faster into the bilayer than into the single layer, as can be seen in that for the flux in Fig. 7.2(a) and Fig. 6.2(a) the same penetration depth is found although the external fields are $B = 3.2$ mT and $B = 16$ mT, respectively. Further, the anisotropy is enhanced in the bilayer, the magnetic flux penetrates even more easily along the APBs as compared to across the steps than is the case for the YBCO thin film. Also, there is an asymmetry in the flux penetration coming from a variation in thickness throughout the film plane, as will be discussed in more detail in Chapter 7.2.

From the images of the magnetic flux distribution, the critical current distribution in the film is calculated following the same scheme of inversion of the Biot-Savart law as for the YBCO thin film. Two thus obtained images of the modulus of the critical current distribution in the bilayer at $T = 9$ K are shown in Fig. 7.3(a) for an increasing field of $B = 3.2$ mT and in Fig. 7.3(b) for the remanent state. The gray scale refers to current densities from $j_c = 0$ A/m^2, black contrast, up to $j_c = 1.1 \cdot 10^{11}$ A/m^2, bright contrast. The strong anisotropy of the critical current is enhanced as compared to the single layer YBCO, Fig. 6.3. In the remanent state, at this temperature of $T = 9$ K the two current directions show current densities of $j_{c,L} = 1.1 \cdot 10^{11}$ A/m^2 and $j_{c,T} = 2.0 \cdot 10^{10}$ A/m^2, respectively. These values are considerably lower than those found in the YBCO film with the same microstructure. This means that the addition of a ferromagnetic layer strongly reduces the critical current in the superconducting film.

There is a difference in the critical current between left and right in the image, which is again due to the variation in thickness through the sample.
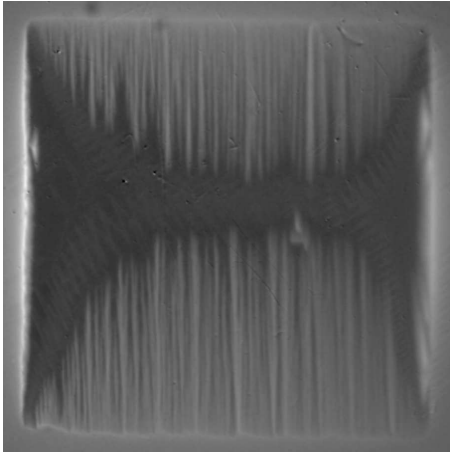
(a) Magnetic flux distribution in an increasing magnetic field of $B = 3.2$ mT.

(b) Magnetic flux distribution in the remanent state.

Figure 7.2: Magnetic flux distributions in a vicinal YBCO/LCMO bilayer at $T = 9$ K.

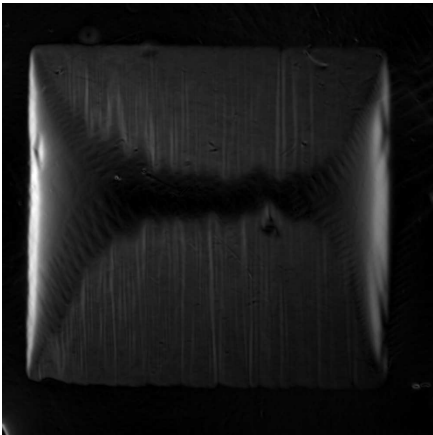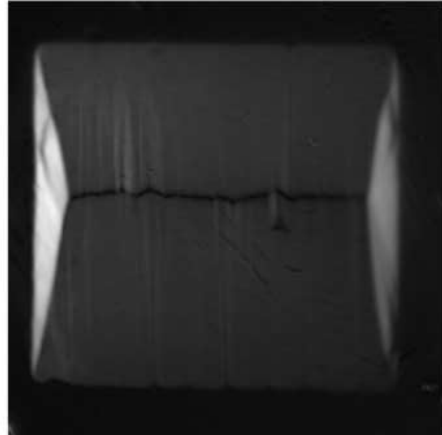(a) Critical current distribution in an increasing magnetic field of $B = 3.2$ mT.

(b) Critical current distribution in the remanent state.

Figure 7.3: The critical current distributions in the vicinal YBCO/LCMO bilayer at $T = 9$ K.

7.2 Temperature Dependence of the Magnetic Flux and Critical Current Distributions

In Chapter 6 a detailed study of the temperature dependence of the critical current in a vicinal YBCO thin film was presented[131]. By doing the same measurements on the bilayer it should be possible to learn how the ferromagnet influences the different current properties in the superconductor. A temperature dependent measurement of magnetic flux in the bilayer was done in the remanent state for temperatures from $T = 9$ K and up to above $T_c = 81$ K[146]. Images were again taken in steps of one Kelvin while slowly heating the film. In Fig. 7.4 a sequence of thus obtained images shows the temperature dependence of the magnetic flux between 10 K and 70 K. These images are comparable to those shown in Fig. 6.5 for the YBCO film. The behavior is similar in the two films, the magnetic flux is slowly leaving the sample with increasing temperature while the anisotropy is decreasing.

For each of the measured images, the critical current density distribution is calculated. Resulting is a series of images showing the distribution of j_c at each K. A sequence of such images is shown in Fig. 7.5 at increasing temperatures from $T = 10$ K up to $T = 50$ K.

With increasing temperature the current anisotropy is getting smaller and also there is an overall decrease in the critical current, similar to Fig. 6.6. The main difference between the single and bilayer is the higher anisotropy of the bilayer especially at lower temperatures.

Values for the critical currents are determined for each current direction separately for all measured temperatures from $T = 9$ K to above $T = 80$ K. Due to the variation in thickness, the areas are chosen in the left and upper parts, where the film is thicker. These carefully obtained values are plotted over the temperature in Fig. 7.6. The longitudinal current direction along the APBs is plotted as squares and the transversal as circles. The difference in temperature dependence between the two current directions is here even larger than for the YBCO thin film, Fig. 6.7.

From these data T_c can be determined which is shown in Fig. 7.7. It can be estimated as the temperature where j_c disappears. It is found that T_c is close to $T = 81$ K for both current directions. Comparing with the critical temperature $T_c = 91$ K of the single layer, the addition of the ferromagnet apparently not only reduces the critical current in the film but also the temperature of the superconducting transition.

Looking at the images of magnetic flux and critical current density dis-

(a) T=10 K

(b) T=20 K

(c) T=30 K

(d) T=40 K

(e) T=50 K

(f) T=70 K
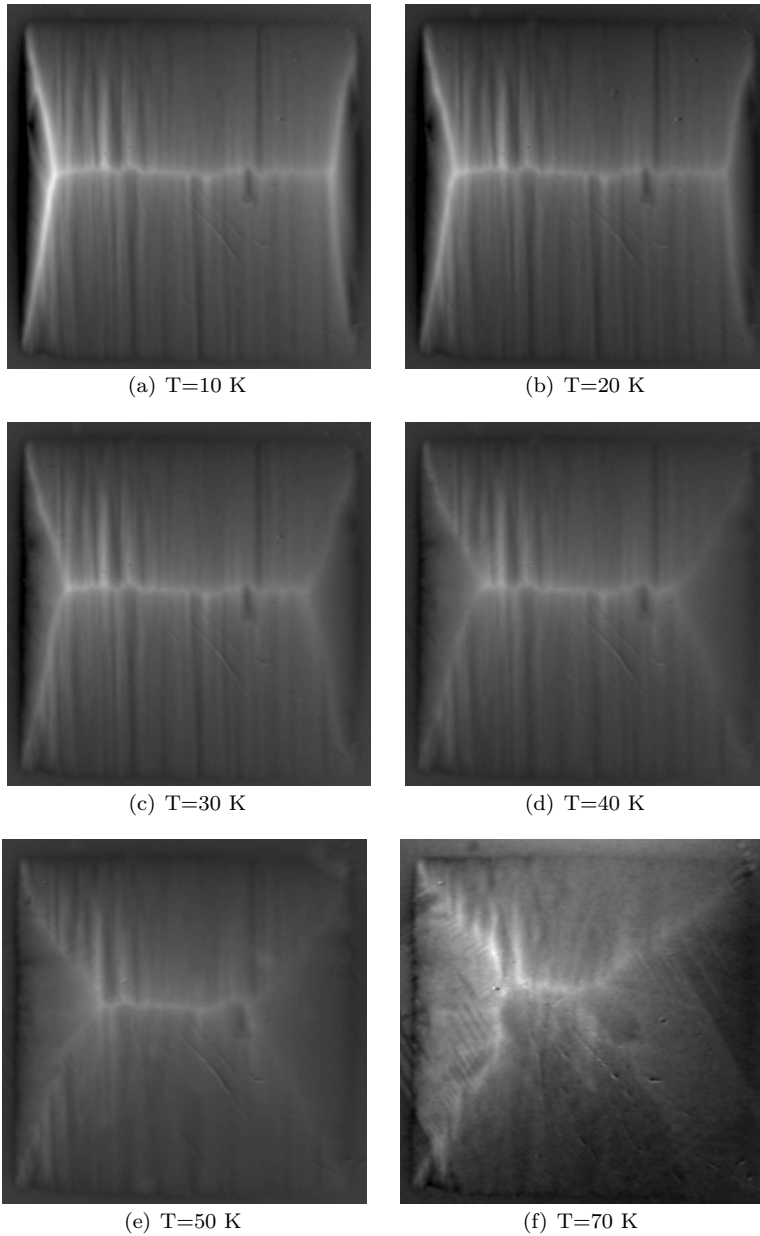
Figure 7.4: Temperature dependence of the magnetic flux distribution in the remanent state in the YBCO/LCMO heterostructure.

(a) T=10 K

(b) T=20 K

(c) T=30 K

(d) T=40 K

(e) T=50 K

(f) Sketch of the current distribution indicating the areas where current values are extracted.
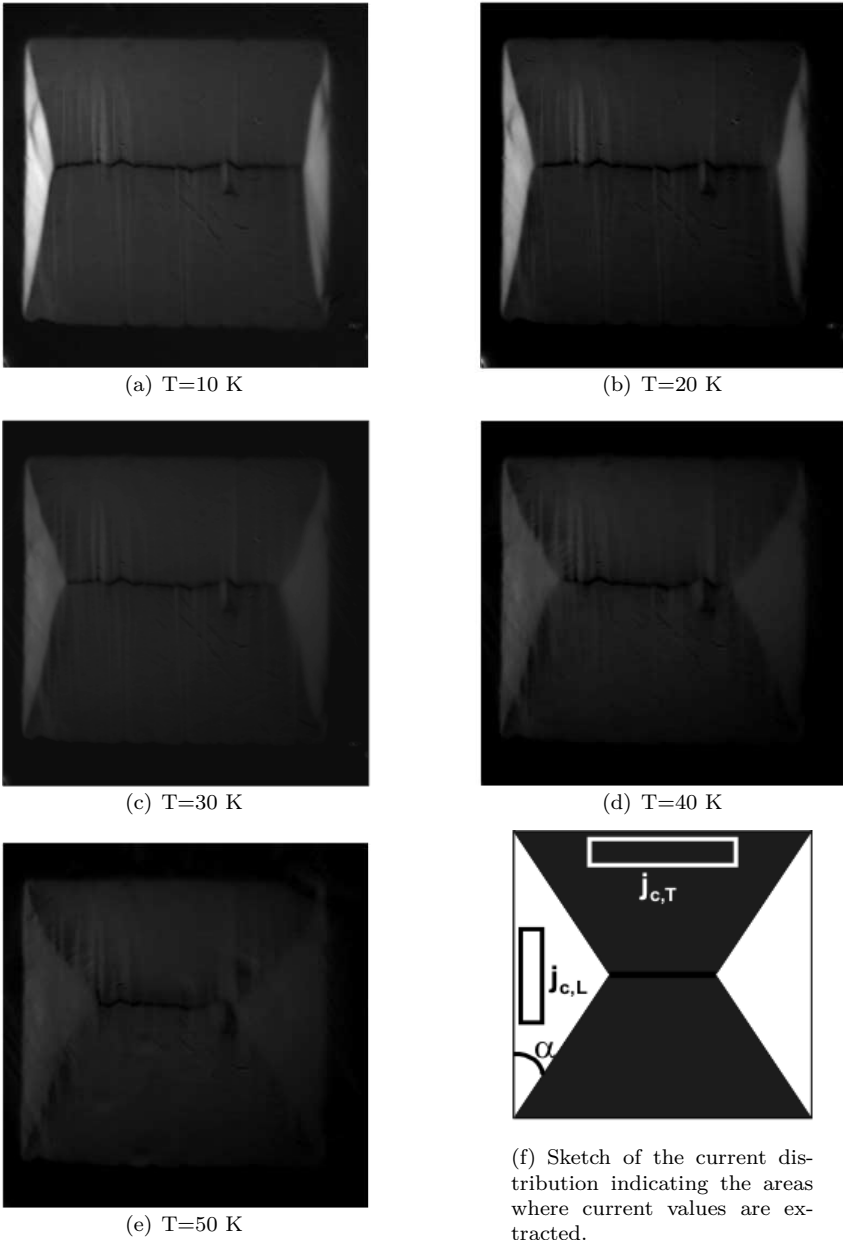
Figure 7.5: Temperature dependence of the critical current density distribution in the remanent state for the YBCO/LCMO heterostructure.
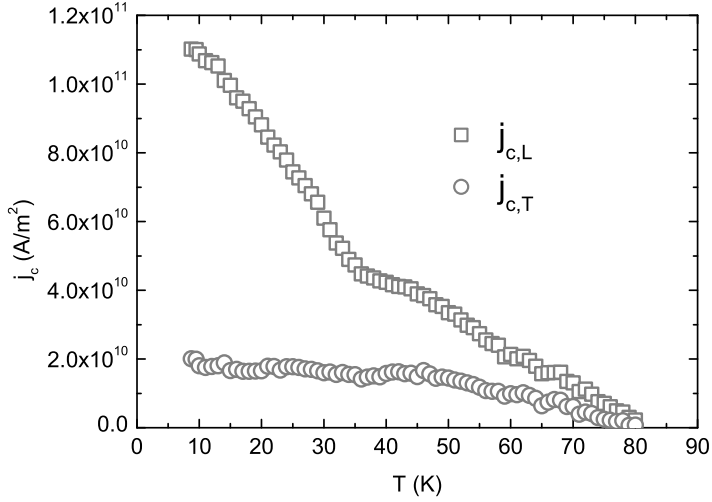
Figure 7.6: Temperature dependence of the critical currents $j_{j,L}$ and $j_{c,T}$ in the YBCO/LCMO bilayer.
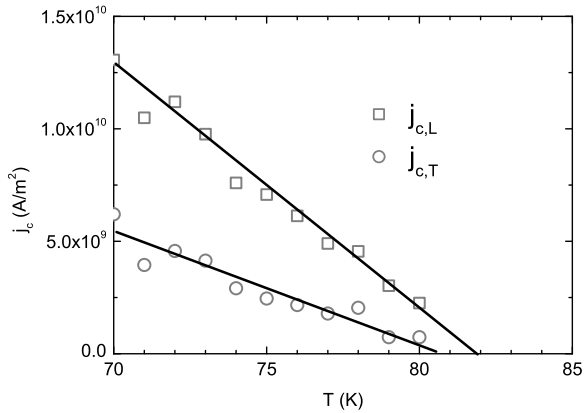
Figure 7.7: Determination of $T_c = 81$ K from the temperature dependence of the critical current.
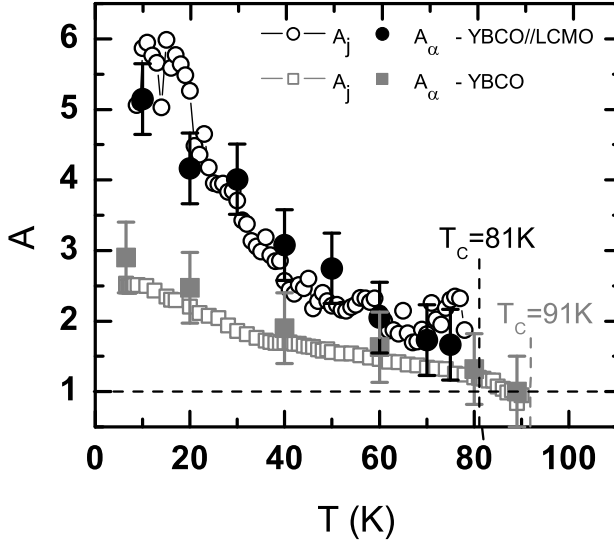
Figure 7.8: Comparison of the temperature dependence of the current anisotropy of the YBCO/LCMO bilayer (circles) and the single YBCO layer (squares). Open symbols are calculated from the current values, filled symbols from the geometry of the critical current distribution.

tribution of the bilayer they might at first seem to be very similar to those of the single YBCO film. But taking a closer look the larger anisotropy of the bilayer is clearly to be identified. This can of course be investigated in more detail by calculating the current anisotropy of the bilayer and compare it to that found for the single layer presented in Fig. 6.9. Following this, both the current anisotropy $A_c = j_{c,L}/j_{c,T}$ and the geometrically determined anisotropy $A_\alpha = 1/\tan\alpha$ is calculated and added to Fig. 6.9. This new graph is shown in Fig. 7.8, where the light gray values are for the YBCO thin film and the black values for the hybrid structure where open circles are A_j and filled circles A_α. Again there is an excellent agreement between the anisotropy values determined by the two different methods.

A comparison of the temperature-dependent anisotropies between the two samples directly reveal the much higher anisotropy of the bilayer. Especially at low temperatures the anisotropy in the bilayer is with $A \approx 5$ about twice as high as in the YBCO thin film. Further the anisotropy is decreas-

ing much more rapidly when the temperature increases. Above $T = 40$ K though there is no real difference in the temperature dependences. Also the anisotropy of the bilayer is here only slightly higher than in the single layer. It is interesting that the anisotropy of the bilayer is not disappearing at $T_c = 81$ K but still has a value of $A \approx 2$.

Thickness Variation in the Film

It has already been mentioned in the previous chapters that there is a variation of thickness throughout the film plane in the hybrid structures. In Fig. 7.9, it can be seen how it affects the properties of the film.   First of
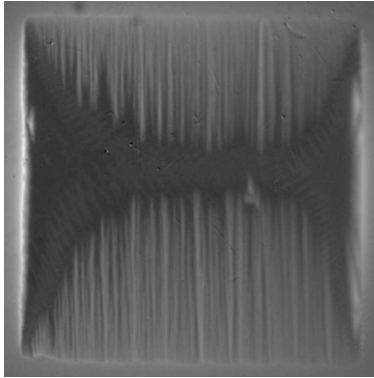
(a) Magnetic flux distribution in an increasing field of $B = 3.2$ mT and at T=9 K.
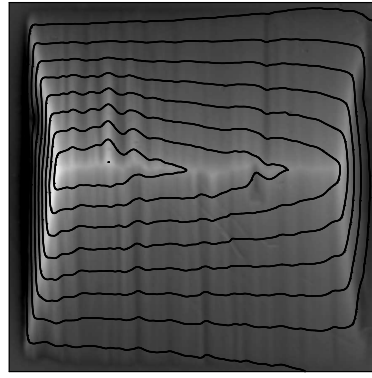
(b) Magnetic flux distribution in the remanent state at T=9 K. Also seen are the calculated current stream lines.
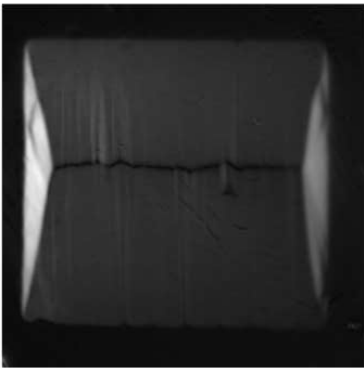
(c) Critical current distribution in the remanent state at T=9 K.
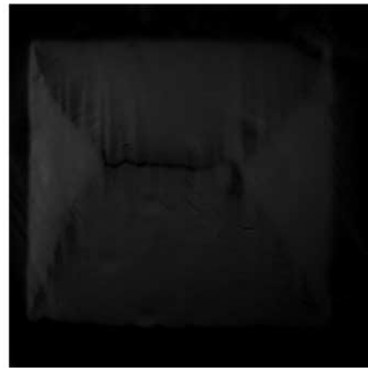
(d) Critical current distribution in the remanent state at T=50 K.

Figure 7.9: The thickness variation of the bilayer affects the different properties of the superconductor.
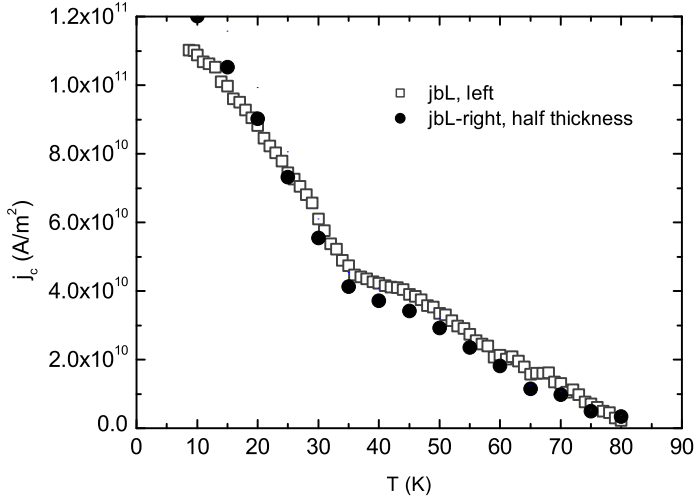
Figure 7.10: Temperature dependence of $j_{c,L}$ calculated in areas with different thickness. Open squares refer to the thicker left part of the bilayer, filled circles to the right part which is assumed to have half the thickness.

all the penetration of magnetic flux is influenced. The flux penetrates more easily into the thinner parts, found in the bottom right corner of the film, see Fig. 7.9(a), than into thicker areas like in the upper left corner. The resulting flux distribution is thus asymmetric. Since magnetic flux and critical currents are closely related, naturally also the critical current distribution is asymmetric due to the thickness variation. This asymmetry is getting stronger with increasing temperature and is therefore seen more clearly in Fig. 7.9(d). Since the thickness is assumed to be constant throughout the whole film plane in the calculation of the critical current density distribution this results in an image where thinner areas show darker contrast, like in Fig. 7.9(c), meaning an underestimation of j_c. This is also seen when looking at the calculated current stream lines in the film, Fig. 7.9(c). The current stream lines are lying much closer in the left part of the film compared to the right.

If we assume the thickness of the film in the right part to be the half of the thickness to the left, it is possible to calculate new correct values for the critical current in this part. In Fig. 7.10 the same temperature dependence of $j_{c,L}$, as in Fig. 7.6, calculated in the left area, is here shown as open squares. Additionally the new values, calculated with half the thickness and extracted in the right part of the film is shown as black filled circles. There is an excellent agreement between the two analyses, proving that the thickness variation does not influence the temperature dependence of the critical current which is the major topic of this work.

7.3   Changing the Growth Order

After studying the behavior of the current in a hybrid structure, where the ferromagnet has been grown on top of the superconductor, it is natural to ask what happens if the growth order is changed. The structure of such a bilayer is shown in Fig. 7.11. A layer of 50 nm LCMO is grown onto the vicinal cut STO substrate followed by the growth of a 100 nm thick YBCO layer on top.

Images of the magnetic flux and critical current distributions, Fig. 7.12 and Fig. 7.13 respectively, show that YBCO grows very well onto LCMO. This is proven by the high critical currents of $j_{c,L} = 1.5 \cdot 10^{11}$ A/m^2 and $j_{c,T} = 7.0 \cdot 10^{10}$ A/m^2 found at low temperatures, and also by a high value of the critical temperature $T_c = 90$ K. The same temperature-dependent measurement is done as for the previous two films. In Fig. 7.12 the resulting magnetic flux distributions in the remanent state is shown for temperatures between $T = 14$ K and $T = 85$ K. Striking is that the anisotropic flux penetration does nearly not change when the temperature is increased. The corresponding images of the critical current density distribution is seen in Fig. 7.13. The bilayer shows only a few defects, apart from which the film

Figure 7.11: Structure of a bilayer consisting of 50 nm LCMO grown on vicinal cut STO and covered with a layer of 100 nm YBCO.

(a) T=14 K

(b) T=30 K

(c) T=60 K

(d) T=85 K
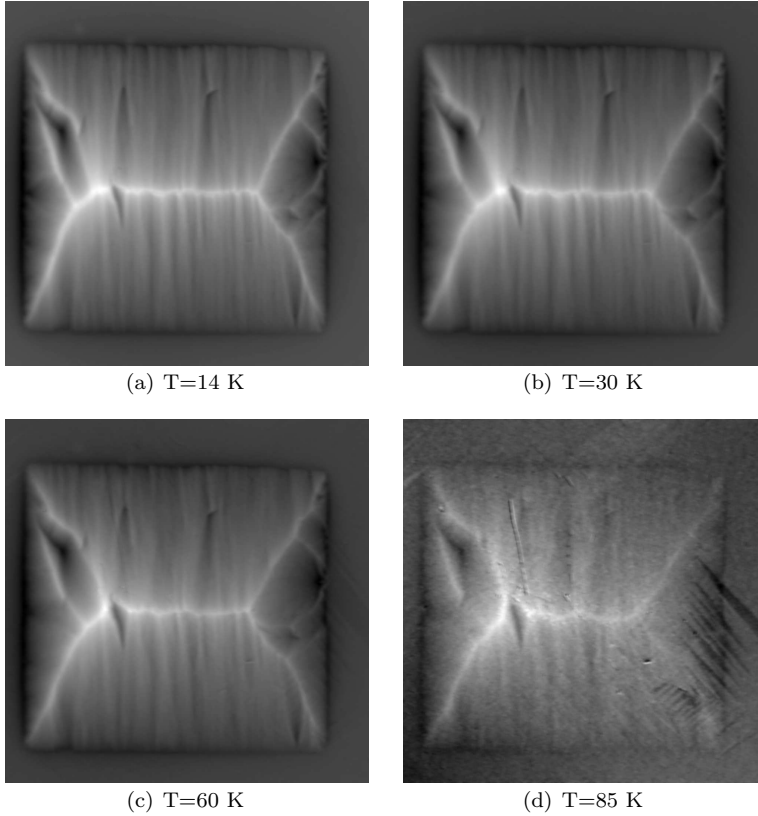
Figure 7.12: Temperature dependence of the magnetic flux distribution in the remanent state in the LCMO/YBCO heterostructure.

is very homogeneous. The current anisotropy is determined to be $A \approx 2.4$ at low temperatures. It is not surprising that the anisotropy is lower when growing the YBCO on top of the LCMO. The steps must be partly overgrown by the LCMO and thus the step and terrace structure is less pronounced when growing the superconductor. Surprising is though, that the current anisotropy is almost not decreasing at all with temperature. At $T = 85$ K the distribution of j_c looks very similar to that found at $T = 14$ K.

The microstructure of the superconductor in this hybrid structure is much more complicated. The YBCO layer is grown on top of a LCMO layer which has been grown onto a vicinal cut substrate, which results in a not well defined microstructure. To be able to understand the behavior of the

(a) T=14 K

(b) T=30 K

(c) T=60 K

(d) T=85 K
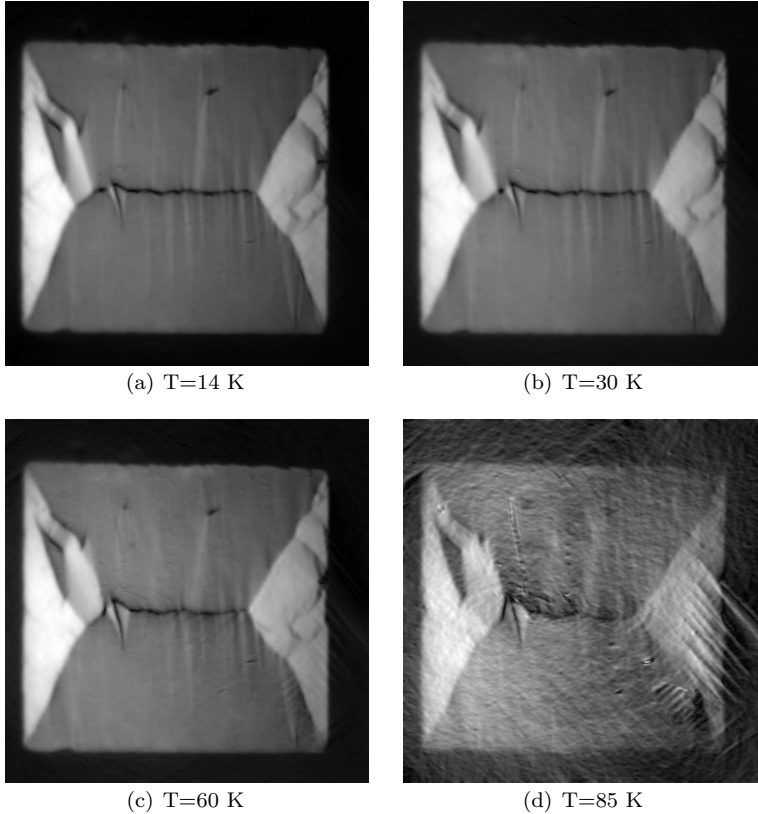
Figure 7.13: Temperature dependence of the critical current density distribution in the remanent state for the LCMO/YBCO heterostructure.

critical current in these bilayers it is needed to thoroughly investigate the growth properties. Such investigations are beyond this work. Nevertheless, the conclusion can be made that the growth order in hybrid structures of superconducting and ferromagnetic layers is very important to the properties of the critical current and an interesting topic for further research in the future.

7.4   Perspectives - Bilayers on Flat Substrates

Heterostructures grown on flat substrates might at first thought seem to be a simpler system than the vicinal heterostructures. But as discussed in Chapter 3.3 films on flat substrates contain many growth islands with

associated grain boundaries. This leads to films with microstructures that are not very well defined. This makes it difficult to separate between growth induced and ferromagnetic influences on the critical current. Investigations of the critical current in such heterostructures is thus very difficult but will hopefully follow in the near future. The presented study of the vicinal bilayer will be the starting point for such explorations into more complex systems like superconductor/ferromagnet bilayers grown on flat substrates.

Chapter 8

The Influence of Microstructural Properties on Critical Currents in Thin Films

In the previous chapter it was found that an additional ferromagnetic layer strongly influences the critical current in a superconducting thin film. Not only the critical current was reduced but also the current anisotropy became significantly larger after adding a ferromagnetic layer to the superconductor, see Fig. 8.1.

The change in current anisotropy, when adding a ferromagnetic layer,
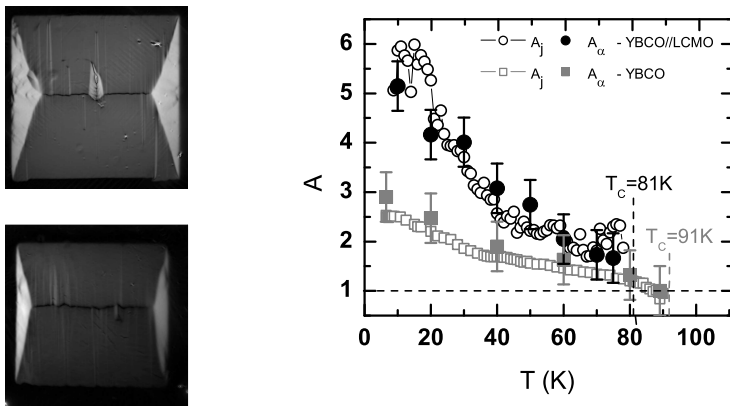
Figure 8.1: The critical current density distributions at T=20 K in a) the vicinal YBCO thin film and b) the bilayer. In c), the temperature dependence of the current anisotropies in the two films are shown. The black symbols refer to the bilayer, the gray to the YBCO thin film.

must mean that the temperature dependence of the two current directions is influenced in different ways. This means for understanding the influence of the ferromagnet it is necessary to understand the behavior of both current directions individually. But before discussing the complex system of the bilayer, a simpler system needs to be understood; the critical current in the vicinal single layer YBCO. The microstructure of the vicinal film is very well defined, due to the special growth process occurring[80]. Such films are typically very smooth and nearly free of grain boundaries along the steps. Between the steps there are narrow extended defects acting as excellent pinning centers. In the following the temperature dependence of critical currents in these films will be discussed for each current direction independently. This is a prerequisite for the analysis of the influence of an additionally ferromagnetic layer.

8.1 Critical Currents and Pinning Mechanisms in a Vicinal YBCO Thin Film

In an epitaxial thin superconducting film there are several possible pinning mechanisms that can be responsible for the current transport[6, 82]. Here, the special case will be discussed where the size of the pinning sites is of the order of the coherence length ξ. This is what is expected in thin films on vicinal cut substrates, where the main pinning sites are the very narrow APBs between the steps[127]. A flux line located in a pinning potential made up from such pinning sites is depicted schematically in Fig. 8.2. At zero current, the depth of the pinning potential is the pinning energy U_0. This quantity is in good approximation proportional to the flux line energy $\epsilon(T)$[147] if the flux lines are individual and non-interacting. This is well fulfilled in the magneto-optical measurements of this work when the current density data is extracted from areas of low magnetic flux densities. Looking at a flux line located in the pinning potential, three mechanisms can be imagined to be important for the pinning properties of the film. First of all, the flux line might be activated to jump out of the pinning potential as seen in the sketch. This is most probable at high temperatures where a lot of thermal energy $k_B T$ is available. For this mechanism mainly the depth U_0 of the potential is important. When less thermal energy is available, the flux lines do not have enough energy to jump out of the potential. The strength of the pinning is therefore not given by the depth of the potential but by its gradient which is proportional to the pinning force f_p. Finally, there will
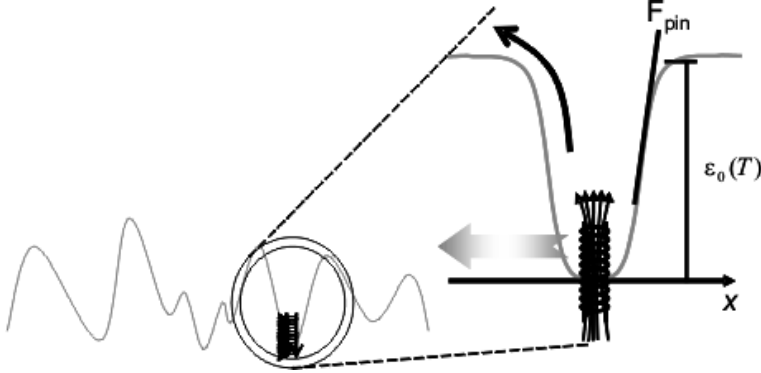
Figure 8.2: Sketch showing a flux line in its pinning potential. Pointed out are the three main pinning mechanisms responsible for the current properties of the film. Thermally activated depinning, strong flux line core pinning and quantum creep.

always be a finite probability for tunneling of flux lines through the pinning potential even at low temperatures and strong pinning.

The individual flux line is well defined by the two characteristic lengths ξ and λ both having a temperature dependence of $(1-T/T_c)^{-1/2}$ close to T_c. At these temperatures the Ginzburg-Landau theory gives an expression for the condensation plus kinetic energy per unit length of the flux line,

$$\epsilon_{0,kin+cond}(T) = \frac{\Phi_0^2}{8\pi\mu_0\lambda^2(T)}. \tag{8.1}$$

The only temperature dependent term is $\lambda(T)$ which leads to a temperature dependence,

$$\epsilon_{0,kin+cond}(T) = \epsilon_0(1-\frac{T}{T_c}). \tag{8.2}$$

The coherence length $\xi(T) = \kappa^{-1}\lambda(T)$, where κ is the Ginzburg-Landau parameter, describes the length over which the energy can vary.

For a flux line to get depinned it needs to be exposed to an activation energy U_0 which will be proportional to $\epsilon_{0,kin+cond}(T)$. Though the above discussion is strictly taken only valid close to T_c it will be assumed that the temperature dependence of the critical current will follow a similar power law behavior wherefore the following ansatz will be made,

$$j_c(T) = j_c(0)(1-\frac{T}{T_c})^s. \tag{8.3}$$
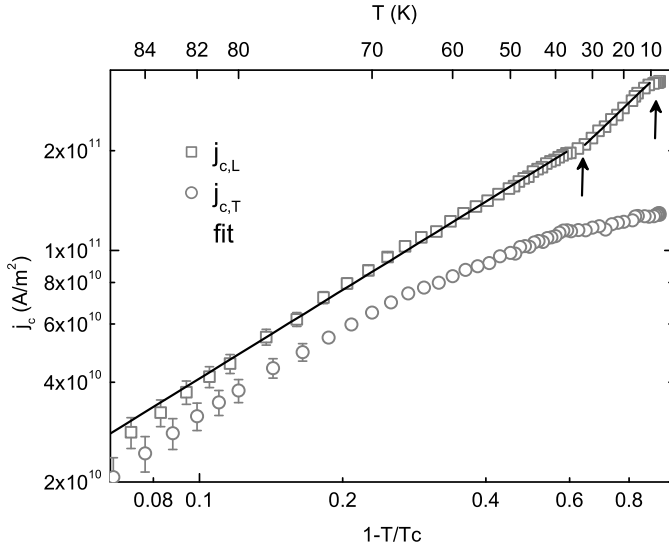
Figure 8.3: Temperature dependence of the critical currents $j_{c,L}$ and $j_{c,T}$ in the vicinal film. The stright lines are fits of Eq. (8.3).

The exponent s has not been given a fixed value since a function is wanted that is valid also at lower temperatures where the temperature dependence might change.

Assuming a power law dependence of the critical current as above, the measured data should fall onto straight lines when plotted over the reduced temperature $t = 1 - T/T_c$ in a double logarithmic scale. This is what is seen in Fig. 8.3, where $j_{c,L}$ and $j_{c,T}$ are plotted as squares and circles, respectively.

The plot shows that for the longitudinal current, flowing along the very homogeneous path along the steps, the power law can describe the data very well at least if applied step wise[131]. The transversal current direction has a completely different temperature dependence. The power law can not describe this temperature dependence which instead, as will be seen later, can be treated in a modified Ambegaokar and Baratoff tunneling model. To study the temperature dependences in more detail, each current direction and temperature regime will be treated separately, starting with the longitudinal current.

The Longitudinal Current Direction

The longitudinal current flowing along the steps is a current flowing along a nearly nondisturbed current path with strong pinning at the planar defects made up from the antiphase boundaries, see Fig. 8.4. Here, the current direction with respect to the steps of the substrate is indicated as well as the Lorenz force acting on the flux lines.

In Fig. 8.5, now only $j_{c,L}(T)$ is plotted double logarithmically with respect to the reduced temperature, following the power law ansatz of Eq. (8.3). The errors are estimated not to be greater than $3 \cdot 10^9$ A/m^2 and are shown in the diagram, at lower temperatures being smaller than the symbols. The solid black lines are fits to the power law. When applied step wise, it describes the temperature dependence of the critical current very well. Three distinct temperature regions are identified showing different temperature dependences of the critical current.

Interesting is the strong change in temperature dependence at a transition temperature of $T \approx 40$ K. At this temperature there is a change in the power law and the exponent is getting larger at lower temperatures. Further at the lowest temperatures, below a second transition temperature of $T \approx 15$ K, the data deviate from the power law description. These two temperatures, indicated with arrows in the figure, are dividing the measured data into three well defined temperature regimes each showing a distinctly different behavior of the critical current and, thus, being governed by dif-
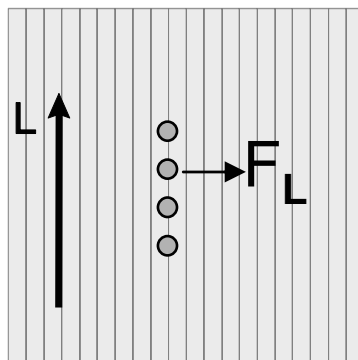
Figure 8.4: Sketch of the film, with the longitudinal current direction indicated with respect to the anti phase boundaries or the substrate steps. Also seen is the action of the Lorenz force on the flux lines.
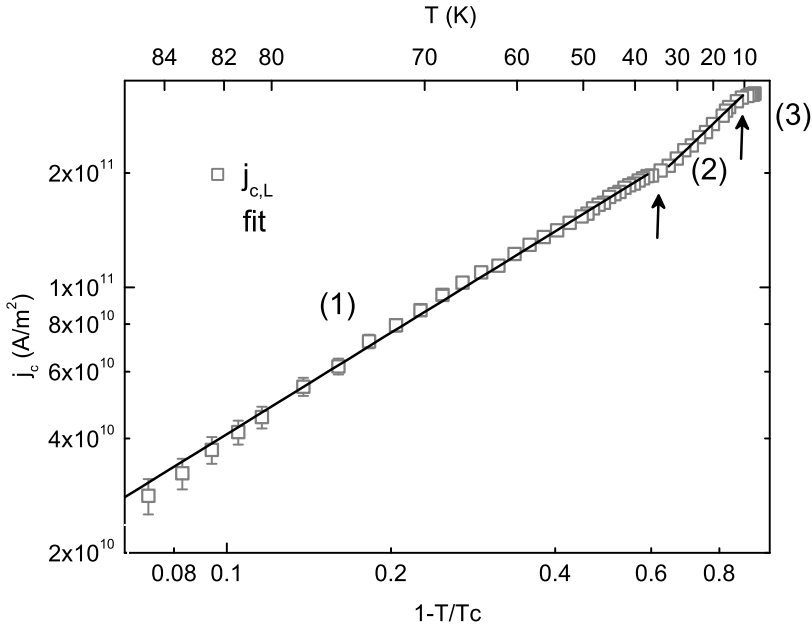
Figure 8.5: Temperature dependence of the longitudinal critical current $j_{c,L}$. The solid black lines are fits to the power law Eq. (8.3). Three distinct temperature regimes are identified, numbered 1), 2) and 3) with different current properties and separated by sharp transition temperatures.

ferent pinning mechanisms. These three temperature regimes are indicated by numbers in the figure and need to be treated separately when studying the critical current and pinning mechanisms in the film. This will be done in the following for the regimes of 1) for $T > 40$ K, 2) for $15 < T < 40$ K and 3) for $T < 15$ K.

Temperatures Above T=40 K - Thermally Activated Depinning

At high temperatures above $T = 40$ K the data can be be described very well by a power-law as seen in Fig. 8.5. The fit using Eq. (8.3) with $j_c(0)$ and s as free parameters results in the black line in the figure. The exponent is found to be $s = 0.9 \pm 0.1$ which means there is nearly a linear temperature dependence.
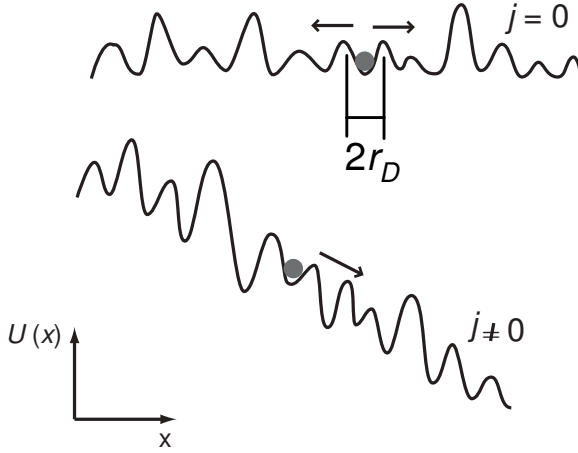
Figure 8.6: Pinning potential without and with a flowing current. The radius r_D of the potential at a certain pinning site is indicated.

Since the experimental data is obtained at low magnetic flux densities it is possible to discuss the results in the frame of individual flux line pinning. When a current is flowing in the superconductor, the depth of the pinning potential $U_0(j)$ of radius r_D will be reduced in one direction, see Fig. 8.6, and thus favor creep of flux lines in that direction. The reduced potential barrier is given by,

$$U(j) = U_0 - j_c\phi_0 r_D. \tag{8.4}$$

in one direction, and thus favoring the creep of flux lines that direction. At temperatures of 40 K and above there is a lot of thermal energy available. This energy can activate the flux lines to jump out of its pinning potential if the thermal energy $k_B T$ is in the order of $U(j)$, see Fig. 8.7. When this is fulfilled the corresponding critical current $j_c(T)$ can be determined,

$$j_c(T) \approx \frac{1}{\phi_0 r_D}(U_0 - k_B T). \tag{8.5}$$

Due to the strong pinning at the APBs in the YBCO thin film, the pinning energy $U_0 >> k_B T$ and the above expression can be simplified. As already discussed U_0 is proportional to the flux line energy, $U_0 = \alpha\epsilon_0(T)$. This finally deliver the following temperature dependence of the critical current,

$$j_c(T) \approx \frac{\alpha\epsilon_0}{\phi_0 r_D}(1 - \frac{T}{T_c}). \tag{8.6}$$
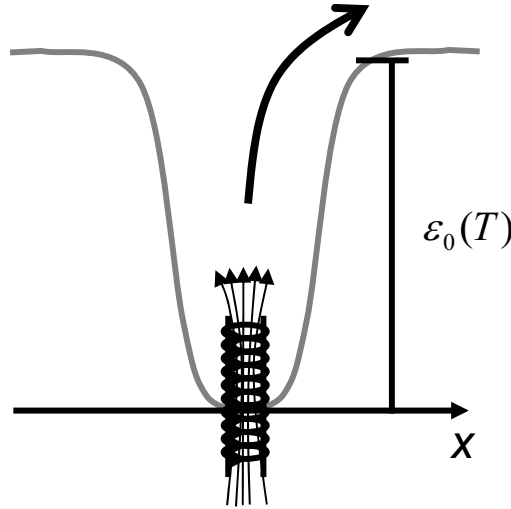
Figure 8.7: Sketch of a flux line in its pinning potential. At high enough temperatures, the flux line is thermally activated to depin and can move to the next pinning cite.

This means, that for elevated temperatures the temperature dependence of the critical current should be following,

$$j_c(T) = j_c(0)(1 - \frac{T}{T_c})^1, \tag{8.7}$$

having an exponent $s = 1$. The experimental result for temperatures $T > 40$ K is $s = 0.9$ and very close to this suggested value. This leads to the conclusion that for this temperature regime, thermally activated depinning of the flux lines could act as the major limiting factor for the critical current density.

Temperatures Below T=40 K - Strong Flux Line Core Pinning

At $T = 40$ K the power-law describing $j_{c,L}(T)$ changes and the slope is getting steeper, see Fig. 8.8. This means that the critical current is decreasing stronger with temperature than at higher temperatures. But again there there is a good fit of the power-law function Eq. (8.3), but with a different exponent. This exponent $s = 1.4 \pm 0.1$ is significantly larger than at higher temperatures indicating a categorical change of the flux pinning properties.

Figure 8.8: Temperature dependence of the longitudinal critical current $j_{c,L}$ in the temperature regime below $T = 40$ K. The solid black line is a fit of the power law function Eq. (8.3) with an exponent $s = 1.4$.

At these low temperatures the errors are estimated to be smaller than the symbols.

At lower temperatures, there is less thermal energy available and thermal depinning plays a minor role. Since the rate of thermal depinning is proportional to $e^{-\frac{U_0}{k_B T}}$ it is decreasing strongly with increasing temperature at the transition temperature of $T = 40$ K. For lower temperatures, this makes it less probable for thermally activated processes to play an important role for flux line pinning. This leads to a transition between regimes with different pinning mechanisms, where the transition occurs at the distinctive temperature of $T = 40$ K.

Since the available thermal energy is not sufficient for substantial thermally activated depinning, the maximum local pinning force governs the flux pinning mechanisms. The force required to remove a flux line from a pinning site is given by the maximum gradient of the energy landscape in
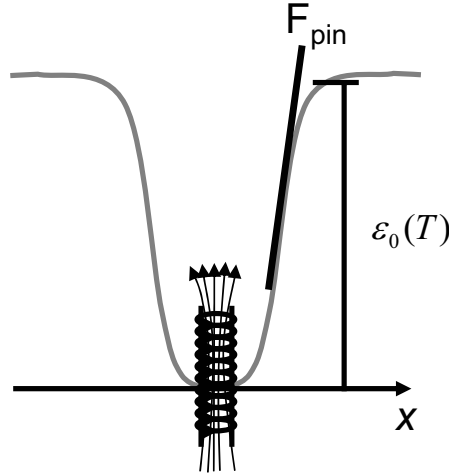
Figure 8.9: Sketch of a flux line in its pinning potential at temperatures below $T = 40$ K. There is strong flux line core pinning preventing the motion of flux lines.

the direction of the acting Lorenz force. This means that the shape of the potential at the pinning site is more important than its depth.

The maximum pinning force f_{pin}^{max} depends on the structure of the pinning sites. In vicinal films the APBs are the main pinning centers and those have a structural width $r_0 \approx 0.7$ nm which is smaller than the coherence length $\xi = 1.5$ nm. This makes it possible to discuss the pinning in terms of flux line core pinning at pinning sites with radii $r_0 < \xi_0$[148, 149].

For such a system the pinning energy of a flux-line displaced a distance u from the center of a pinning site, is given by,

$$\epsilon_{pin}(u) = -\frac{\epsilon_0}{2}\frac{r_0^2}{u^2 + 2\xi^2}. \tag{8.8}$$

The pinning force is obtained by deriving this expression with respect to u,

$$f_{pin}(u) = \epsilon_0 \frac{u r_0^2}{(u^2 + 2\xi^2)^2}. \tag{8.9}$$

having its maximum at $u = 2/3\xi$. When the width of the pinning site is smaller than the coherence length and it has a normal conducting and not insulating area, there is a proximity effect, meaning that the area of suppressed superconducting order parameter cannot be smaller than the flux

line core. The radius of this area is in the size of the coherence length and thus there is an effective width of the pinning site,

$$r_0^{eff} \approx \xi(T) = \xi(0)(1 - \frac{T}{T_c})^{-1/2}. \tag{8.10}$$

With this knowledge it is possible to determine the temperature dependence of the maximum pinning force,

$$f_{pin}^{max} = f_{pin}(u = \frac{2}{3}\xi) = \frac{9}{32}\sqrt{\frac{2}{3}}\frac{\epsilon_0}{\xi}. \tag{8.11}$$

Since the critical current is proportional to the pinning force, it has the same temperature dependence depending only on the ratio $\epsilon_0(T)/\xi(T)$,

$$j_c(T) = \frac{c}{\phi_0}f_{pin}^{max} = \frac{9}{32}\sqrt{\frac{2}{3}}\frac{c}{\phi_0}\frac{\epsilon_0}{\xi} \propto (1 - \frac{T}{T_c})^{3/2}. \tag{8.12}$$

Thus, in systems with narrow defects, smaller than ξ, the strong flux line core pinning leads to a temperature dependence of the critical current,

$$j_c(T) = j_c(0)(1 - \frac{T}{T_c})^{1.5}. \tag{8.13}$$

The experimentally found exponent of $s = 1.4$ has within errorbars exactly the same value as this theoretical value of $s = 3/2$. This agreement suggests that for temperatures $T < 40$ K there is strong flux line core pinning enabling the high critical currents.

Temperatures Below T=15 K - Quantum Creep

At very low temperatures below 15 K, as displayed in magnification in Fig. 8.10, the power-law cannot describe the experimental data. This can be explained by the onset of quantum creep of flux lines at this low temperature. This means there is a finite probability for the flux line to tunnel through the pinning potential from one pinning site to another, see Fig. 8.11. Quantum creep has been observed with different measurement methods at similar temperatures. Wen et al.[150] observed quantum creep in 100 nm thick YBCO thin films at temperatures $T < 13$ K by measuring the superconducting current by means of high-sensitivity capacitance torque magnetometers. Further, a review of magnetic relaxation measurements in HTSC by Yeshurun et al.[151] presents more results on quantum tunneling of flux lines.
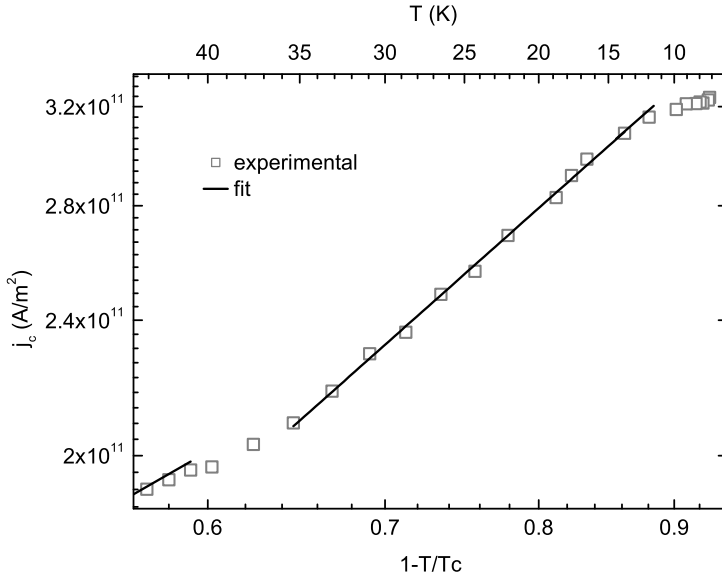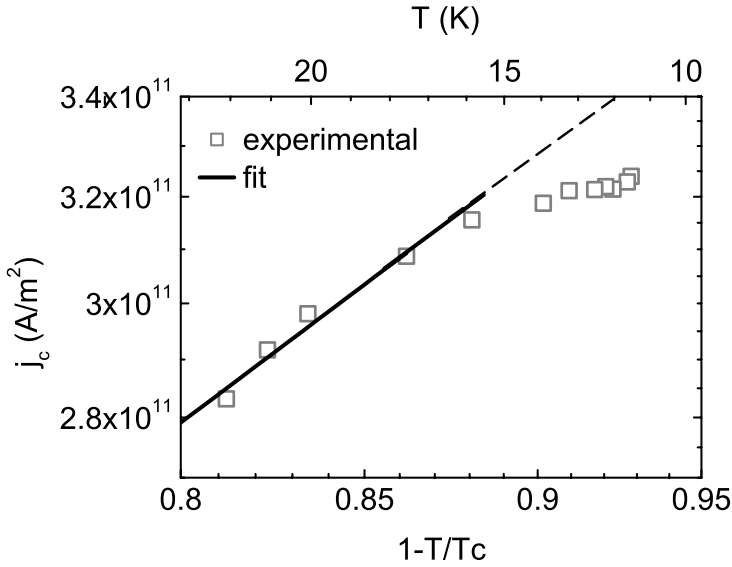
Figure 8.10: Temperature dependence of the longitudinal critical current $j_{c,L}$ in the temperature regime below $T = 23$ K. The saturation at temperatures below $T = 15$ K is explained by quantum creep of flux lines. The dashed line is showing the temperature dependence if there would be no quantum creep.
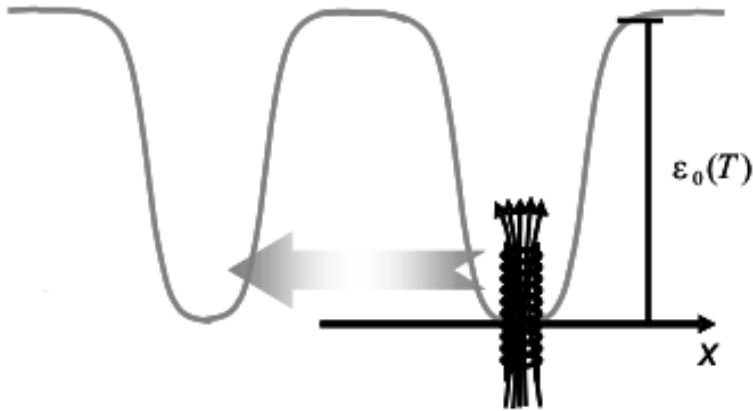
Figure 8.11: Sketch of a flux line in its pinning potential at temperatures below $T = 15$ K. Shown is how the flux line can tunnel through the potential barriers from one pinning site to the next.

Summary of the Different Pinning Mechanisms

The different current-limiting mechanisms found for the longitudinal current direction in the vicinal YBCO film can be summarized in a phase-diagram-like sketch, Fig. 8.12[152]. This mimics the situation in optimally YBCO thin films in small magnetic fields and strong pinning. In the sketch the pinning potential is seen for increasing temperatures from $T = 7$ K on the left up to $T_c = 91$ K on the right. The change in temperature is indicated by the changing contrast from left to right. Three different pinning regimes are indicated and the important influence on the flux lines depicted. The three regimes are, starting with the low temperatures seen to the left in the figure,

1. The Quantum Creep (QC) regime for temperatures below $T = 15$ K. The flux lines can tunnel through the pinning potential from one pinning site to the next limiting the maximal critical current. This results in a temperature dependence of $j_c(T)$ deviating from the power-law.

2. The Flux Line Core Pinning (FLCP) regime for temperatures from $T = 15$ K up to a transition temperature around $T = 40$ K. In this regime the very strong flux line core pinning at narrow pinning sites is responsible for the high critical currents that are observed. The temperature dependence $j_c(T)$ is in agreement with a power-law description with an exponent $s \approx 1.5$ comparable to Ginzburg-Landau theory.

3. The Thermally Activated Depinning (TAD) regime for temperatures above the transition region around $T = 40$ K. The large amount of thermal energy available provide the flux lines with enough activation energy to jump out of the pinning potential to neighboring pinning sites. This results in the linear decrease of $j_c(T)$ with temperature that is observed.

Note, that pinning sites of flux lines does not necessarily need to be the same in the different temperature regimes. It is likely that at low temperatures small and narrow defects are the most effective pinning sites but at higher temperatures their effect is smeared out if enough thermal energy is provided.
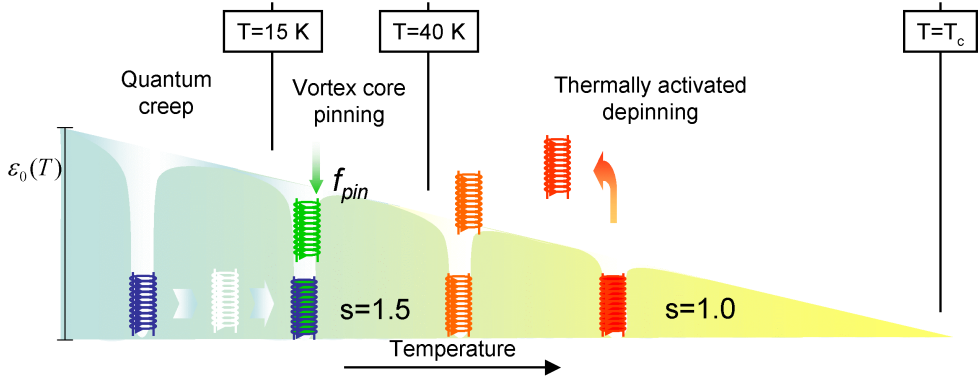
Figure 8.12: The experimental results of the pinning properties in the vicinal YBCO film can be summarized in a phase-diagram-like sketch. The increase in temperature is indicated by the changing contrast from left($T = 0$) to right($T = T_c$). The three different generic pinning regimes are indicated.

8.2 Comparison of Films with Different Microstructure

The current limiting mechanisms have been analyzed in case of a superconducting film with nearly homogeneous current path and strong pinning as is the case for the vicinal YBCO film. It is interesting to compare these results with measurements on similar films with different microstructures. In Fig. 8.13 such a comparison is made for the temperature dependence of the critical current density. All films are epitaxially grown YBCO thin films of similar thickness, but grown onto substrates with different structures. This results in films with different grain-boundary structure. The measured films are from top to bottom;

- The L-direction from the already discussed vicinal YBCO thin film, nearly without grain boundaries along the current path, squares[131, 133].

- A YBCO film grown onto an engineered substrate resulting in a film with improved connectivity between the growth island, circles[130].

- A high-quality YBCO film grown onto a flat substrate, thus containing many grain-boundaries, triangles[130].

- An individual substrate-induced low-angle tilt grain boundary having a misorientation angle of $3°$, reverse triangles[111].

Common for all samples are their high critical currents, meaning that they all must exhibit strong pinning and not contain weak links.

The power-law Eq. (8.3) can describe the temperature dependence of all samples, as seen by the solid lines[152]. In all films the transition at $T \approx$ 40 K between the TAD and FLCP regimes is observed. To identify the QC regime there are not enough datapoints available in all of the measurements. Considering the temperatures above $T = 40$ K, all films show the same linear temperature scaling of $j_c(T)$ with respect to the reduced temperature. This means that for all the films thermally activated depinning plays a major role for the limitation of the current.

Below the cross-over region around $T = 40$ K, where FLCP region was found for the grain boundary free current in the vicinal film, different slopes of the current-temperature curves are observed. For a better comparison the critical current in this regime has been plotted again in Fig. 8.14, but here the values have been normalized to its values at $T \approx 15$ K, below which the onset of quantum creep is expected and thus a deviation from the power-law occurs. The figure shows that there is a strong connection between the granularity of the film and the temperature dependence of $j_c(T)$. With increasing granularity of the film, the slope is getting steeper which means the critical current is decreasing stronger with increasing temperature. The corresponding power-law exponent is getting larger with increasing granularity, only the very homogeneous current path in the vicinal film follows the theoretical value of $s = 1.5$, indicated with the dotted line in Fig. 8.13. The other samples exhibit two-dimensional defect structures perturbing the path of the supercurrents, being the coalescence regions between the growth islands, or the individual grain boundary. The values of the exponents are also seen in Fig. 8.14, increasing up to $s = 2.5$ for the individual grain boundary.

This result states that networks of low-angle grain boundaries, like in films containing growth islands, clearly affect the temperature stability of high critical currents at low temperatures. The systematic increase of the exponent s further shows that the temperature dependence of the critical current density is strongly affected by the quality of low-angle grain boundaries in the films, even if the misorientation angle is in the order of 1° and smaller.

This is clearly different from results found by transport measurement or magnetization measurements, where a suppression of j_c only was found for grain boundary misorientation angles of $3° - 5°$ and above[153, 21, 154]. Gurevich et al. have explained this with that the flux-lines have differ-
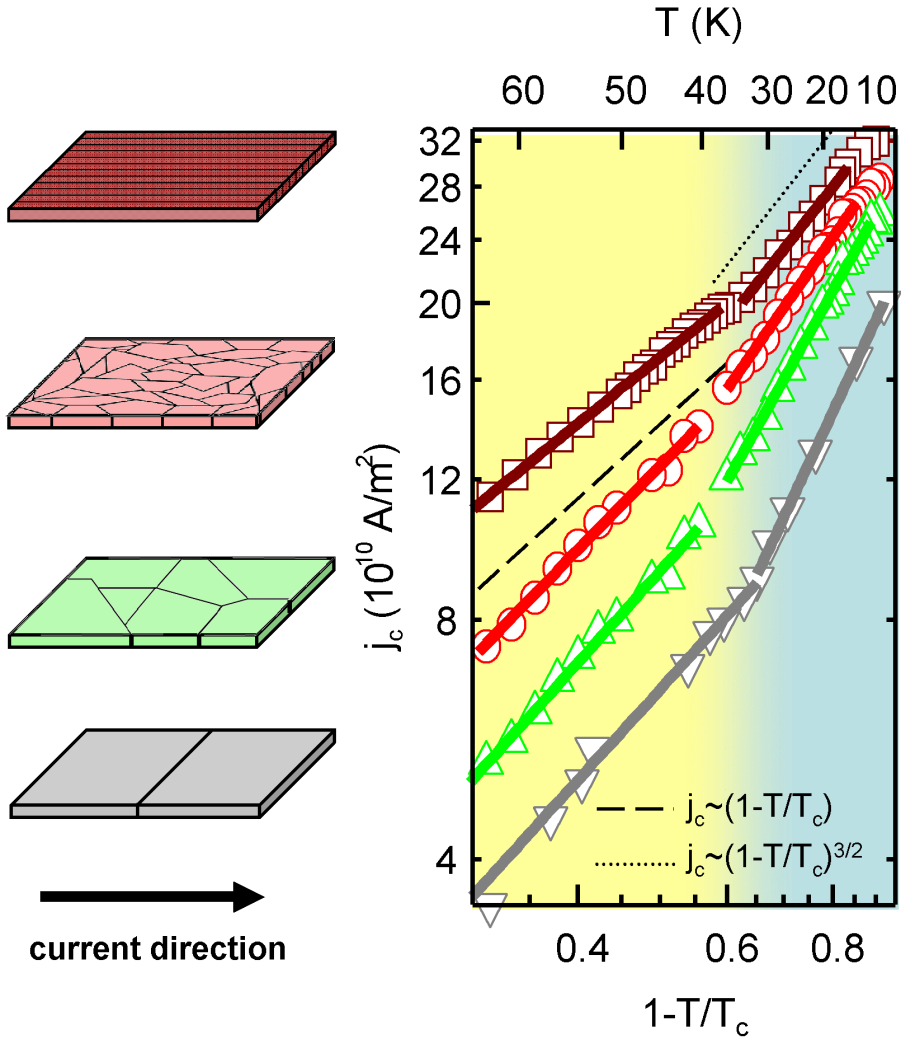
Figure 8.13: Temperature dependence of the critical currents j_c for films with different microstructure. From top to bottom the plotted data is for, the L-direction of the vicinal film having a nearly grain boundary free current path (squares), a film grown onto a pretreated flat substrate with improved grain boundary connectivity (circles), a regularly grown epitaxial film on a flat substrate (triangles), a film containing an individual 3° tilt grain boundary (reverse triangles). The dashed line represents a temperature dependence $j(T) = 1 - \frac{T}{T_c}$ and the dotted line $j(T) = (1 - \frac{T}{T_c})^{3/2}$
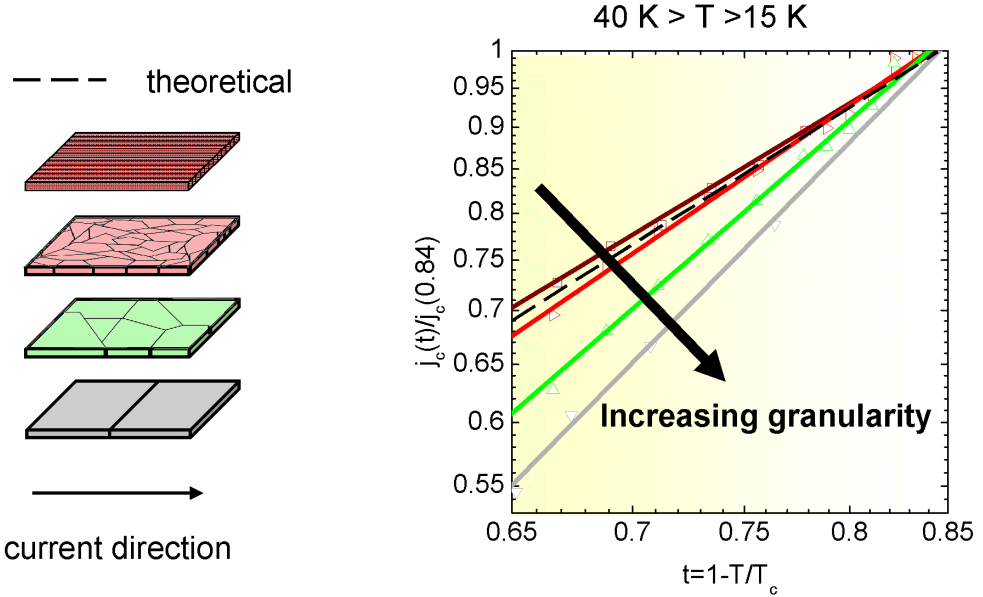
Figure 8.14: Comparison of the temperature dependence of j_c for films with different microstructure for $15 < T < 40$ K. The data is normalized to its values at $T \approx$ 15 K. The slope is getting steeper with increasing granularity of the film.

ent structure depending on the angle of the grainboundary[155, 156]. Depending on tilt angle and magnetic field Abrikosov vortices (A), Abrikosov-Josephson vortices (AJ) and Josephson vortices (J) have been observed, see Fig. 8.15, where the tilt-angle regions with different flux-line structures are defined[157]. The suppression of j_c for misorientations above the threshold angle $\theta_c > 2°$ has been explained by the transition of Abrikosov (A) vortices with normal conducting cores to Abrikosov-Josephson (AJ) vortices with a Josephson core or for even larger tilt angles to Josephson (J) vortices, see Fig. 8.16(a)[155]. In the figure, the current stream lines in the three categories are shown. The picture does not include the relative length scales, where the actual length of the J vortex is much larger than the AJ which is in turn much larger than the A core. The reason for different j_c-values depending on the tilt angle of the grain boundary can be explained by varying strength of pinning. The flux lines are expected to be pinned along the grain boundary where a chain of edge dislocations are formed which act as pinning centers[156]. As the misorientation angle is increasing this leads
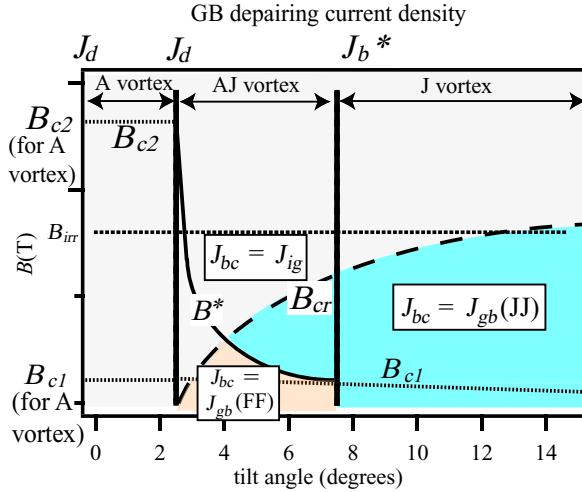
Figure 8.15: Depending on the tiltangle of the grainboundary and magnetic field, there are different types of vortices. Taken from T. Horide et al. [157]

to a smaller distance between these dislocations and for a certain threshold angle this distance will be smaller than the coherence length ξ. This lead to an overlap of the normal conducting Abrikosov cores and the consecutively transition into highly anisotropic Abrikosov-Josephson flux lines with a Josephson core of length $l \gg \xi$. Due to the larger vortex core, the pinning is weakened in the direction of the grain boundary which turns into a channel for motion of flux lines between the strongly pinned isotropic Abrikosov vortices in the grains. Since the critical current is directly dependent on the flux line pinning this also explains the strong suppression of j_c in films with low-angle grain boundaries with $\theta > 3°$.

In Fig. 8.15, different vortices are defined as depending on tilt angle and magnetic field. All of the films of Fig. 8.13 and Fig. 8.14 have misorientation angles of $3°$ and below. Following the model of Fig. 8.15, they should all contain just Abrikosov vortices apart from the $3°$ boundary itself. This is also confirmed by magneto-optical measurements of different low-angle grain boundaries[159], where no increased flux penetration could be noticed for a $2°$ tiltboundary. Nevertheless there is still a strong influence from the grainboundaries on the temperature dependence of the critical current. The systematic change in temperature dependence of j_c due to increasing grain boundary angles thus needs to have a different origin.

(a) Current lines in from left to right Abrikosov (A), Abrikosov-Josephson (AJ) and Josephson (J) vortices. The grain boundary is running along the y-axis. After[158].

(b) Current lines in the newly defined Anisotropic Abrikosov (AA) vortex found in grainboundaries with misorientation angles $< 2°$.

(c) Current densities along the x-axis of the flux lines seen in (a). The size of the cores $\xi_A << l_{AJ} << \lambda_A < l_J$ is defined.

(d) Current density along the x-axis in the AA vortex defined in (b). The length of the anisotropic normal conducting core is $\xi_{AA} > \xi_A$ along the grainboundary.

Figure 8.16: Definition of the different vortices that might exist at grainboundaries: Abrikosov vortex (A), Anisotropic Abrikosov vortex (AA), Abrikosov-Josephson vortex (AJ) and Josephson vortex (J). All images are qualitative.

Studying the pinning mechanisms again, since there are still A vortices though in the form of AA, the theory of flux line core pinning discussed in Chapter 8.1 for $T < 40$ K, should still be valid. There, the pinning force was found to be inversely proportional to the coherence length, Eq. (8.11). For the AA vortices with s larger coherence length this would result in weaker pinning along the grain boundary,

$$f_{p,GB} \propto \frac{\phi_0}{\xi_{AA}}, \qquad (8.14)$$

which will be smaller than the pinning force of isotropic A vortices. The AA are thus more easily depinned which leads to suppression of j_c which was also found experimentally. Since the anisotropy of the AA core is expected to increase with tilt angle this also explains the increased suppression of j_c

with granularity of the film. From Eq. (8.12) we have,

$$j_{c,GB} \propto \frac{c}{\phi_0} \frac{\epsilon_0}{\xi_{AA}}. \tag{8.15}$$

This means that already a very small deformation of the AA core can lead to a relatively strong suppression of the critical current, which explains the experimental results.

8.3   Influence on the Critical Current Through the Addition of a Ferromagnetic Layer

After the detailed discussion of the critical current densities in YBCO thin films and especially $j_{c,L}$ in the vicinal film, in a next step it will be discussed how the addition of a ferromagnetic layer influences the superconducting film. The interest is twofold. First, the creation of a second interface to a ferromagnetic material gives rise to new interesting phenomena due to the mutual interaction. Second, and not less interesting the ferromagnetic layer will be a tool to further test the accuracy of the developed models describing the pinning properties in YBCO thin films.

To enable such a study of high-temperature superconducting/ ferromagnetic heterostructures it is important to have a well defined system. In the previous chapters we saw how important the choice of the substrate is for the properties of the critical current. This clearly shows that in order to study the influence of the ferromagnet, the vicinal film is the most suitable starting point, since in all the other films, the granularity influences the critical current in complicated ways.

Experimental results for the temperature dependences of the critical current of a YBCO/LCMO hybrid structure were presented in Chapter 7. It has been found that the behavior is different than in the YBCO single layer. In order to find where these differences come from, it is checked if the critical current in this structure still can be described by the power-law function in Eq. (8.3). Thus the data is plotted over the reduced temperature in double-logarithmic scale, Fig. 8.17, squares denoting the longitudinal current and circles the transversal. As seen in the plot, the temperature dependence of the longitudinal current can be very well described by the power-law model, the solid black line showing a fit of Eq. (8.3). The transversal current is behaving completely different and shows also for the bilayer a tunneling like behavior. Since the critical current shows a similar temperature dependence as in the single layer YBCO films, the discussion of the longitudinal current
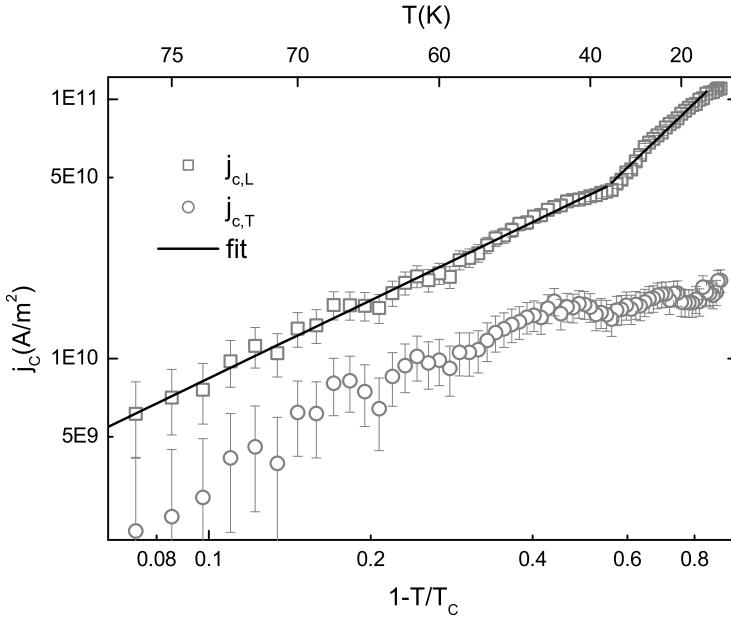
Figure 8.17: Temperature dependence of the critical currents $j_{c,L}$ and $j_{c,T}$ in the YBCO/LCMO heterostructure.

direction will continue with a discussion of the influence the ferromagnetic layer has on the critical current in this direction.

Influence of the Ferromagnetic Layer on the Longitudinal Current

In Fig. 8.18 the temperature dependence of $j_{c,L}$ in the heterostructure is depicted, together with the fit of Eq. (8.3). The power-law can describe the data very well when applied step wise. As was the case for the single layer YBCO, also here three distinct temperature regimes are found. At $T \approx 40$ K, the temperature dependence changes and the slope gets steeper for temperatures below $T = 40$ K. At the lowest temperatures below $T = 15$ K the measured data seem to deviate from the power-law description in a similar way as in the single layer. It is thus possible and necessary to discuss the influence of the ferromagnet on $j_{c,L}(T)$ for each of the temperature regimes separately. This will be done in the following, starting with what
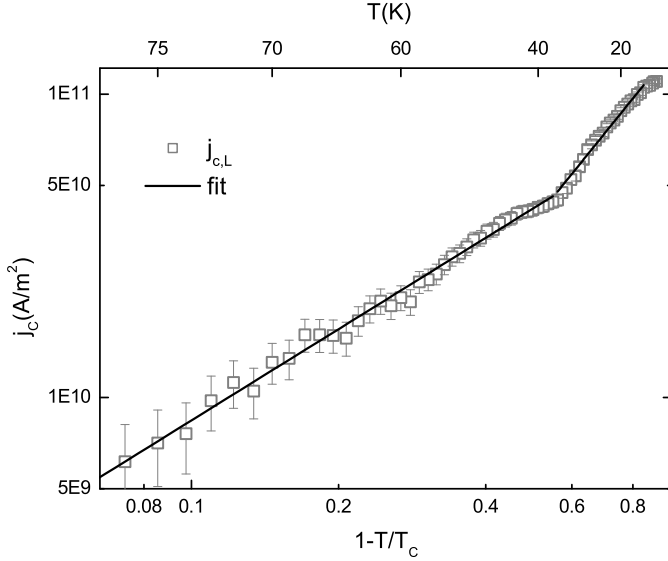
Figure 8.18: Temperature dependence of the longitudinal critical current $j_{c,L}$ in the YBCO/LCMO bilayer. The black lines are fits to the power law Eq. (8.3).

was found to be the thermally activated depinning (TAD) regime in thin films of YBCO, independent of their microstructure.

Temperatures Above T=40 K - Thermally Activated Depinning

For temperatures from $T = 40$ K and up to T_c the temperature dependence of $j_{c,L}(T)$ is described very well by the power law function. The exponent is for the bilayer found to be $s = 1.0 \pm 0.1$, see Fig. 8.19, circles. In the figure also $j_{c,L}(T)$ for the single layer YBCO is plotted as squares for comparison and the theoretical value of $s = 1$ as a dotted line. Both of the films have the same temperature dependence of the critical current with exponents close to $s = 1$. Thus, no change in the temperature dependence can be seen due to the addition of the ferromagnetic layer, which means that also in the bilayer, thermal depinning is expected to be the most important current limiting mechanism at high temperatures.

That the temperature dependence of $j_{c,L}$ is not influenced by the ferromagnet in this regime does not mean that there is no interaction between
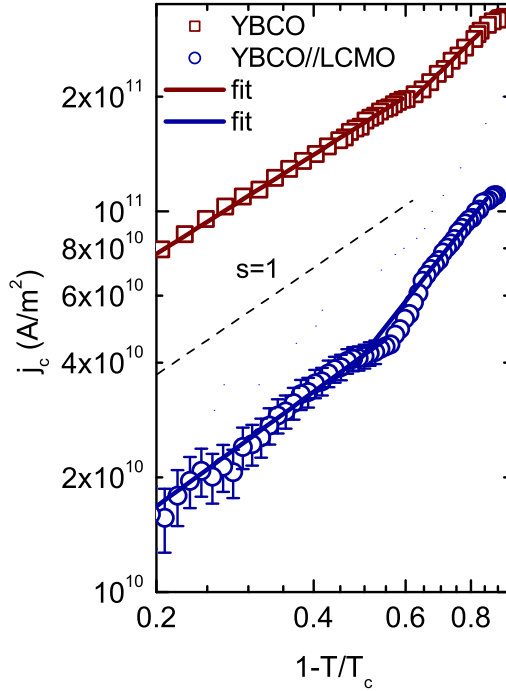
Figure 8.19: Temperature dependence of the longitudinal critical current $j_{c,L}$ in the vicinal YBCO thin film (squares) and the YBCO/LCMO bilayer (circles). The dotted line follow the theoretical values $s = 1$.

the superconducting and the ferromagnetic layers. On the contrary the superconducting properties are strongly affected as can be seen in Fig. 8.19 through the strong current suppression by a factor 3-4. Further the superconducting transition temperature is strongly reduced to $T_c = 81$ K as was found in Chapter 7.2, see especially Fig. 7.2. Strong suppression of both critical current and critical temperature[85, 86] is expected in oxide superconductor/ferromagnet hybrids and originates in different coupling effects of the counteractive ordering phenomena as discussed in detail in Chapter 4. Explanations for these effects are among others the following processes, oxygen diffusion[102], charge transfer[103], redistribution of orbital occupancy[104], spin diffusion[86, 105] and dipolar magnetic coupling via stray fields[106].

Temperatures Below T=40 K - Temperature Dependence Changes

At $T \approx 40$ K the temperature dependence changes for $j_{c,L}(T)$ in the bilayer as well as in the single layer. In the vicinal YBCO thin film an exponent $s = 1.4 \pm 0.1$ was found. In the bilayer, the exponent is larger, meaning a stronger decay of the critical current with temperature. In order to make a more detailed comparison of the two films, the currents are plotted with higher magnification and normalized to their values at $T = 13$ K, Fig. 8.20. The temperature of $T = 13$ K is chosen since below this temperature the data is deviating from the power-law behavior. The critical current of the bilayer, denoted by circles, is decreasing more steeply with increasing temperature than does $j_{c,L(T)}$ in the YBCO single layer, denoted by squares. An exponent $s = 1.8 \pm 0.1$ is found for the bilayer, significantly larger than $s = 1.4 \pm 0.1$ found in the YBCO thin film. This is remarkable because the microstructure of the YBCO constituent of the bilayer should be the same as for the compared individual layer, since the only difference between the two films is the ferromagnet which has been grown on top. The difference in exponent s must therefore originate in an influence of the ferromagnet on the properties of the critical current.
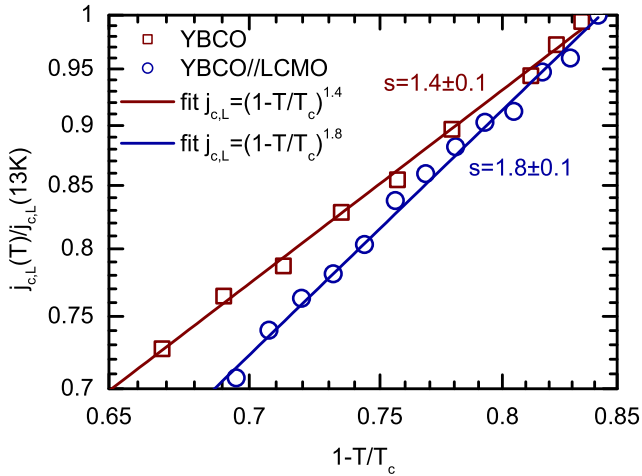
Figure 8.20: Temperature dependence for $T < 40$ K of the longitudinal critical current $j_{c,L}$ normalized to the values at $T = 13$ K in the YBCO thin film (squuares) and the YBCO/LCMO bilayer (circles). The lines are fits to the power law Eq. (8.3).

Temperatures Below T=15 K - Quantum Creep

At the lowest temperatures below $T = 15$ K it was seen that the critical current in the YBCO film is deviating from the power-law behavior. That this is also the case for the bilayer is clearly seen when looking at a magnification of this temperature regime in Fig. 8.21. At $T = 13$ K the temperature dependence changes and the strong increase with decreasing temperature suddenly stops and there is a saturation of $j_{c,L}(T)$.
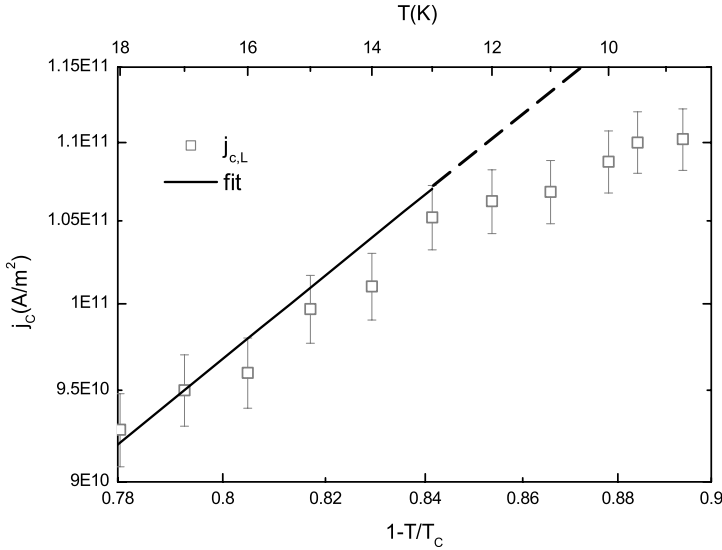
Figure 8.21: Temperature dependence of the longitudinal critical current $j_{c,L}$ in the YBCO/LCMO bilayer for temperatures below $T = 18$ K. There is a saturation of $j_{c,L}$ for temperatures below $T = 13$ K.

Comparison of the Bilayer and Films with Different Microstructure

In Chapter 8.2 a comparison of the critical current in YBCO thin films with different microstructure was made. Temperature dependences for the critical currents was plotted for all temperatures in Fig. 8.13. This comparison will now be extended to include the YBCO/LCMO hybrid structure. Thus the temperature dependence of $j_{c,L}$ for the bilayer has been added in Fig. 8.22 as black open circles. It is seen that for $j_{c,L}(T)$, the bilayer shows the lowest values of all the compared films for all temperatures.
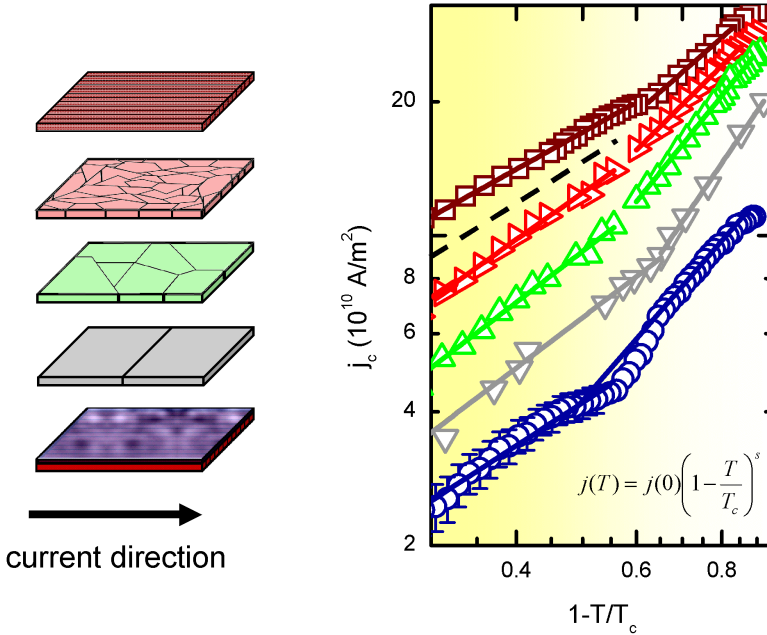
Figure 8.22: Temperature dependence of the critical currents j_c for films with different microstructure. From top to bottom the plotted data is for, the L-direction of the vicinal film having a nearly grain boundary free current path (squares), a film grown onto a pretreated flat substrate with improved grain boundary connectivity (tilted triangles), a regularly grown epitaxial film on a flat substrate (triangles), a film containing an individual $3°$ tilt grain boundary (reverse triangles) and the YBCO/LCMO bilayer (circles). The dashed line represents a temperature dependence $j(T) = 1 - \frac{T}{T_c}$ and the dotted line $j(T) = (1 - \frac{T}{T_c})^{3/2}$

At temperatures above $T \approx 40$ K all the films show the same temperature dependence $j_c = 1 - T/T_c$, with $s = 1$ as foreseen by theory. This means that the TAD regime is universal and is not influenced by the ferromagnet. In all studied samples, independent of microstructure and ferromagnetic interaction the major current limiting mechanism at temperatures above $T = 40$ K is found to be the thermally activated depinning of flux lines.

For the temperatures below $T \approx 40$ K the FLCP regime was found for the very homogeneous current path in the vicinal YBCO thin film. In this temperature regime, $j_c(T)$ strongly depends on the microstructure of the film as was seen in Fig. 8.14. With increasing granularity of the current path, the
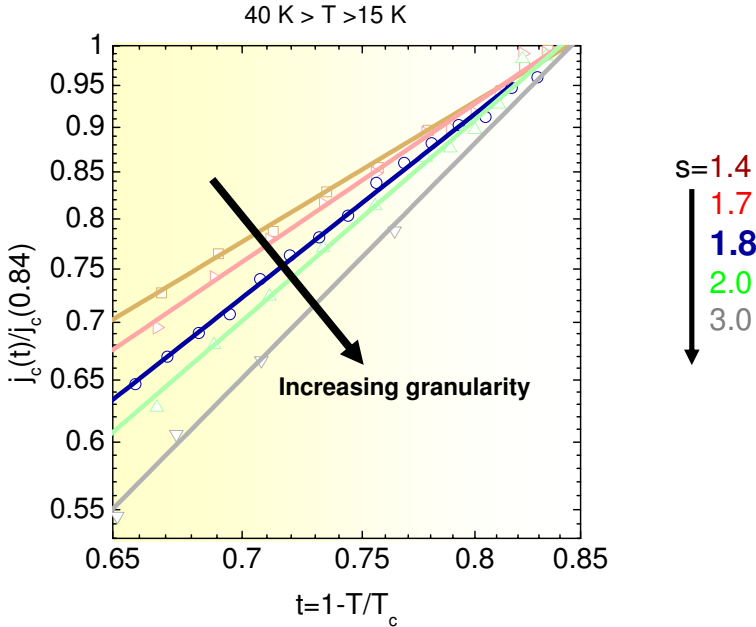
Figure 8.23: Comparison of the temperature dependence of j_c for films with different microstructure for $15 < T < 40$ K. The data is normalized to its values at $T \approx 15$ K. The slope is getting steeper with increasing granularity of the film. j_c for the YBCO/LCMO bilayer is added as the black line with circular symbols.

exponent s is getting larger, meaning stronger decrease of j_c with increasing temperature. In the bilayer the exponent was found to be $s = 1.8$, which is significantly larger than $s = 1.4$ in the vicinal YBCO film, having the same microstructure of the YBCO layer. This value is compared with the values for s in films with increasing granularity in the current path, see Fig. 8.24. The figure is equivalent to Fig. 8.13, only now $j_{c,L}(T)$ for the bilayer is added as black open circles. Astonishingly the temperature dependence of the bilayer shows a behavior typical for films with high granularity in the current path. If an increase of the exponent s refers to an increased inhomogeneity of the current path, this result could mean that there is a magnetically induced inhomogeneity in the YBCO layer of the hybrid structure.

Similar behavior of superconducting systems with granular character and superconducting/ferromagnet heterostructures have already been observed. By measuring the field dependent magnetization in a YBCO film with artifi-
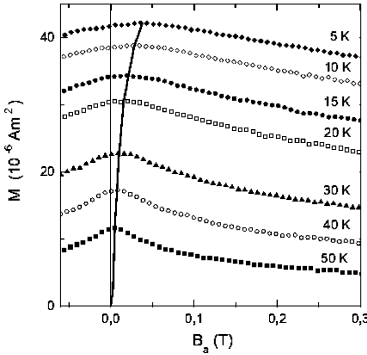
(a) Central part of the magnetization loop of an artificially granular YBCO ample. Taken from D.V. Shantsev et al. [113].
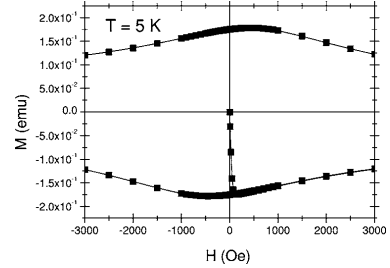
(b) LCMO/YBCO bilayer decoupled by a thin layer of STO. Taken from J. Albrecht et al. [112].

Figure 8.24: Magnetic hysteresis loops showing shifts of the magnetization peaks.

cial granularity, D.V. Shantsev et al.[113] found a shift of the magnetization maximum to finite fields. This can be observed in Fig. 8.24(a), where the central part of the magnetic hysteresis loop is seen. The same effect has been found by J. Albrecht et al.[112] in hybrid structures of LCMO and YBCO where the layers have been electronically decoupled by a thin insulating barriers, Fig. 8.24(b).

Further the Scanning Hall Probe Microscopy (SHPM) measurements of YBCO films grown on top of LCMO discussed in Chapter 4.2 shows that an inhomogeneous magnetic stray field from the ferromagnetic layer penetrates the superconductor over its whole thickness of 100 nm and above[152]. This holds for both flat and vicinal bilayers[160].

Due to the ferromagnet there are spontaneously created flux lines in the superconductor which will not be equally distributed due to the domain structure of the ferromagnet. The magnetic domains of the LCMO layer are expected to be oriented mainly in-plane, since it is grown under tensile strain, while the components of magnetization seen in the SHPM measurement are out-of-plane. This means what is seen is the magnetization at the domain walls, separating the areas of in-plane magnetization, where the magnetic moments are tilted out of the film plane. This means that only at the magnetic domain walls in the ferromagnet there will exist out-of-plane components of the magnetization. So the flux lines are expected to be spontaneously created only along the domain walls. This results in a

density of flux lines along the domain walls, while the inner of the domains will remain flux free. This make the domain walls contain similar flux line distributions as a grain boundary. This can explain the similarity in behavior between films with granular microstructure and the bilayer, where the superconductor can be described as containing a magnetic granularity.

The results of the three experiments discussed above combined with the increase of the power-law exponent s observed in this work all lead to the following conclusion. The transport of supercurrents in all-oxide superconductor-ferromagnet hybrids has to be described as inhomogeneous transport. The inhomogeneity is created by the local magnetic field of the ferromagnet which penetrates into the superconducting film where it creates magnetic obstacles for the current flow.

8.4   The Transversal Current Flowing Across the Steps

In this chapter finally, the transversal current density $j_{c,T}(T)$ both of the YBCO thin film and the bilayer will be discussed. It is the current direction perpendicular to the substrate steps, see Fig. 8.25 which means it has to flow across the anti phase boundaries. The image shows the current direction with respect to the steps of the substrate as well as the Lorenz force acting on the flux lines.

The temperature dependence of the transversal critical current is plotted double logarithmically with respect to the reduced temperature, see
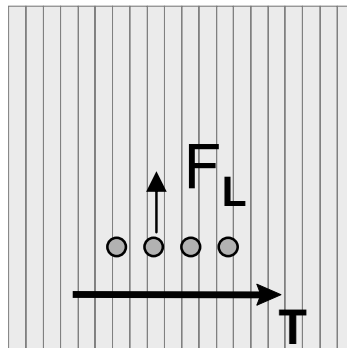
Figure 8.25: Sketch of the film, with the transversal current direction indicated with respect to the anti phase boundaries at the substrate steps. Also seen is the action of the Lorenz force on the flux lines.
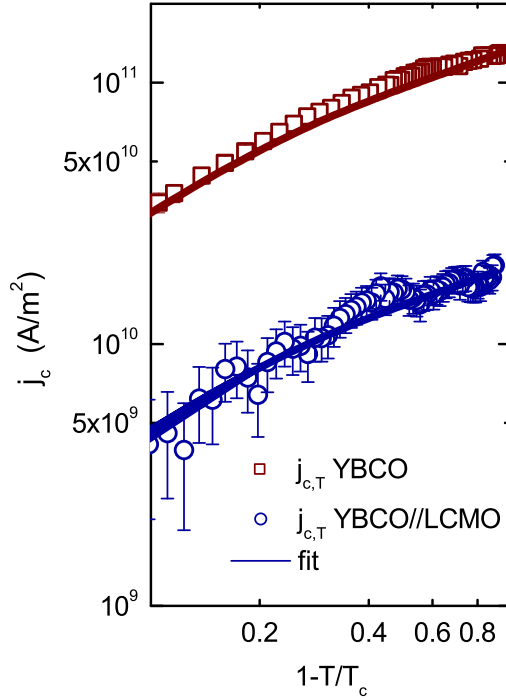
Figure 8.26: Temperature dependence of the transversal critical currents $j_{c,T}$ in the vicinal YBCO film (squares) and the bilayer (circles). The solid lines represent fits to the model of Ambegaokar and Baratoff.

Fig. 8.26, with squares denoting the YBCO thin film and circles the bilayer. The errors are estimated not to be larger than $3 \cdot 10^9$ A/m^2 and are shown in the plot, though for $j_{c,T}$ in the YBCO thin film they are smaller than the symbols. The meaning of the solid lines will be discussed in detail in the following. The temperature dependence is completely different to that found for longitudinal current direction and can not be described by the models developed in the previous chapters. Here a completely new approach is needed.

The APBs are planar defects with a width in the order of the coherence length ξ separating the highly superconducting regions. This makes it

possible to describe the transversal current as a current flowing through an array of superconducting islands with excellent transport properties (as seen in the previous chapters) which are separated by regions of high scattering rates and poor transport properties.

Already in 1987 G. Deutscher and K.A. Müller[161, 162] suggested that such narrow planar defects can be treated as Josephson junctions with depressed order parameter. A model for the Josephson coupling current is the model of Ambegaokar and Baratoff[41], originally describing the temperature dependence of the superconducting-isolator-superconducting tunneling in classical BCS superconductors, see Eq. (1.11). This model needs to be adjusted in order to be applied to high-temperature superconductors. Due to the short coherence length of the oxide superconductors, the value of the superconducting order parameter Δ is much more sensitive to crystallographic defects than is the case for conventional superconductors with their long coherence lengths. Usually this lead to a depression of the order parameter at the defect Δ_i compared to the values in bulk, Δ.

Taking the depression on the order parameter into account the following modified Ambegaokar-Baratoff function is proposed,

$$j(T) = j(0)\sqrt{1 - \frac{T}{T_c}} \tanh(\frac{A\sqrt{1 - \frac{T}{T_c}}}{\frac{T}{T_c}}). \qquad (8.16)$$

Here the depression of the orderparameter is included in $j(0)$ and A that will be used as fitting parameters when applying Eq. (8.16) to measured data.

This modified Ambegaokar-Baratoff function will now be applied to the measured temperature dependences of the transversal critical current $j_{c,T}(T)$ seen in Fig. 8.26 for both the YBCO thin film and the bilayer. The result of the fits, are seen as the solid lines. Though being a very simple model it can describe the measured data surprisingly well. The ratio of $j_{c,T}(0)/j_{c,L}(0) \approx 0.42$ for the YBCO thin film agrees well with the depression of the order parameter $\Delta_i(0)/\Delta(0) = 0.7$.

Now comparing $j_{c,T}(T)$ in the two measured films as seen in Fig. 8.5 there is a strong suppression of $j_{c,T}$ in the bilayer by a factor of about 7 compared to the single layer. This is about twice as strong as the suppression found for the longitudinal current direction. This of course directly explains the different anisotropy values found for the YBCO film and the bilayer, see Fig. 8.1. Further it is highly interesting that no change in temperature dependence due to the general suppression of j_c can be seen.

Assuming Josephson coupling over the APBs, a modulation of the critical current by magnetic fields should also be expected. For a single Josephson junction at zero voltage the magnetic field dependence of the tunneling current is given by the second Josephson equation,

$$j(B) = j(0) \cdot \left| \frac{sin(\frac{\pi \Phi}{\Phi_0})}{\frac{\pi \Phi}{\Phi_0}} \right|, \tag{8.17}$$

with $\Phi = 2\lambda_L l B$ and l the size of the contact perpendicular to the magnetic field. This leads to a the Fraunhofer pattern of the current across the junction as seen in Fig. 1.9. Already a small magnetic field will suppress the critical current substantially.

The structure of a APB though, is not expected to be that of one single clean planar defect. Instead it is expected that they contain numerous defects with a size in of ξ and smaller. Possible defects can correspond to atomic displacements, due to the creation and annihilation of stacking faults. Locally the defects can be large enough with respect to ξ, to cause disruptions of the tunneling current. Such defects can split the APBs into rows of Josephson weak links separated by superconducting material, see Fig. 8.27. Here the transversal current path is depicted as consisting of highly superconducting islands separated by the APBs. Those can be thought of as built up of superconducting and nonsuperconducting regions.

P. Bernstein et al.[163] suggest that planar defects split up in structures that locally behave as Josephson weak links or SQUID-like structure. Such modulation of the critical current by magnetic fields could also be observed experimentally for twin boundaries in YBCO thin films patterned as microbridges. The experiments showed clear evidence of Fraunhofer or SQUID
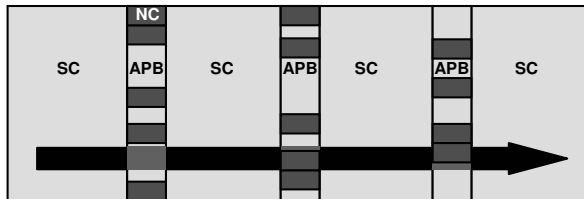
Figure 8.27: The transversal current is flowing across the anti-phase boundaries. Thereby it has to cross regions with reduces superconductivity (APB) separating the highly superconducting islands (SC). The APBs consists of superconducting (SC) and non-superconducting (NC) regions.

like behavior which agreed with the models of current flow across SQUID structures or several neighboring Josephson junctions. For the whole length of the APB there is of course all kind of structures expected, making an exact description very difficult. This description combines the simultaneously observed tunneling characteristic and high critical currents found in measurements.

Nevertheless the above discussion explains why the temperature dependence of the transversal current flowing across the steps is so fundamentally different to the longitudinal current. The current along the two directions are governed by completely different mechanisms, namely by flux line depinning for $j_{c,L}$ and by partial Josephson tunneling for $j_{c,T}$. This results in different magnetic field dependences that directly explain the larger anisotropy of the bilayer.

This chapter contains a discussion of the temperature dependence of the critical current in thin films of YBCO. Though many questions could be answered, there are still many problems to be solved. To further prove the validity of the used models, direct imaging of the flux lines would be helpful. This would especially help to shed light on the physical processes taking place at the transition between different pinning mechanisms at $T = 40$ K.

Chapter 9

Summary

The properties of thin high-temperature superconducting films depend strongly on their microstructure. For applications especially high critical currents and transition temperatures are desirable. Both properties can be controlled by the creation and modification of interfaces to neighboring materials which directly influences microstructural and electronical properties of the superconducting film.

In this work especially the critical current has been investigated in films where systematical modifications have been done in two steps. First, the choice of substrate used for growing the films strongly influences their microstructure. In the next step, a second interface to a ferromagnet was created leading to further implications on the superconducting properties.

Optimally doped YBCO thin films were grown epitaxially on vicinal cut STO substrates. Such films are characterized by a particular well-defined microstructure. This makes the vicinal films an ideal model system for investigating the complex behavior of critical currents found in HTSC. The special step and terrace structure of the vicinal substrate results in YBCO films where the current paths along and across the steps exhibit completely different microstructures. While along the steps of the substrate, the film forms a nearly defect free current path, between the steps an array of extended planar defects are formed called Anti Phase Boundaries, strongly disturbing the current flow.

To get access to the local relation between defect structure and critical current density, a magneto-optical technique is used which enables direct imaging of magnetic flux and current distributions. The combination of a local measurement method which is both quantitative and fast makes the magneto-optic an ideal choice for studying the physics of critical currents in

thin superconducting films.

A detailed analysis of the temperature dependence of the local critical currents yields universal features for YBCO thin films with different microstructure. All films show a power-law relation,

$$j_c(T) = j_c(0)(1 - \frac{T}{T_c})^s, \qquad\qquad (9.1)$$

where the value of the exponent s depends directly on microstructure but also on temperature regimes. The systematic study of the longitudinal critical current flowing along the steps in the vicinal film made it possible to identify three distinct temperature regimes where different pinning mechanisms limit the maximal current.

1. The Quantum Creep (QC) regime, for temperatures up to $T = 15$ K.

2. The Flux Line Core Pinning (FLCP) regime for temperatures from $T = 15$ K up to a transition temperature around $T = 40$ K.

3. The Thermally Activated Depinning (TAD) regime for temperatures above the transition temperature $T = 40$ K.

This result was compared with measurements of the temperature dependent critical current in films with different microstructure stating the universality of the model. While above $T = 40$ K all compared films show the same temperature dependence, below this temperature a strong dependence of the exponent s on microstructure was seen. In the FLCP regime the value of s was found to increase systematically with increasing granularity of the film.

The universal description of the behavior of critical currents in YBCO thin films makes it possible to extend the investigations to more complicated systems. The vicinal film with its well defined microstructure makes an ideal starting point for adding a second interface to a ferromagnet. Superconducting/ferromagnetic heterostructures were created by growing a layer of LCMO on top of a vicinal YBCO thin film. In the resulting bilayer no change of the microstructure in the superconducting film is expected.

The strong influence of the ferromagnet on the superconducting properties was seen in both reduced critical current and transition temperature. Further the current anisotropy present in superconducting vicinal films was found to be enhanced. This represents different influence of the ferromagnet on each of the two current directions.

Analysis of the temperature dependence of the longitudinal critical current in the bilayer showed the same universal behavior as the single layer YBCO films. At temperatures above $T = 40$ K no change in the temperature dependence was found. This means that all the compared films, with different microstructure or added ferromagnetic layer, are expected to have a current limited by thermally activated depinning of flux lines. This is different for the FLCP regime below $T = 40$ K. Here, a strong influence of the ferromagnet on the temperature dependence of j_c was found. This resulted in an increase of the exponent s to values comparable with those found in granular YBCO single layers. This could be explained by the transfer of inhomogeneous stray fields from the ferromagnet to the YBCO layer leading to similar consequences for the current flow as structural inhomogeneities. It could also be shown that this influences the superconducting film through its whole thickness and is not only an interface phenomenon.

The transversal current flowing across the APBs in the vicinal films was undergoing an equally detailed analysis of its temperature dependence. It was found to have a completely different temperature dependence than $j_{c,L}$. A modified Ambegaokar-Baratoff function with depressed order parameter could be used to describe the measured data of both the vicinal YBCO film and the bilayer. In this model, the APBs are treated as Josephson junctions with depressed order parameter.

Further, the transversal critical current was found to be suppressed by the ferromagnet by a factor of 7 which is about twice compared to the longitudinal current. Assuming Josephson coupling over the APBs this could be explained by the strong magnetic field dependence of the tunneling current.

The combination of a superconducting thin film with two current directions with different but well defined microstructure and the addition of an interface to a ferromagnet enabled and was necessary for finding a deeper understanding of the properties limiting the critical current in YBCO thin films.

In the YBCO single layer it was necessary to introduce a new anisotropic Abrikosov vortex with elongated normal core in order to explain the dependence of $j_c(T)$ on the granularity of the film. These anisotropic Abrikosov vortices are expected to be situated on the low angle grainboundaries present in the discussed films. With increasing tilt angle the anisotropy is increasing leading to reduced pinning force directly causing the observed suppression of critical current.

In the bilayer the domain structure of the ferromagnet is expected to

spontaneously create vortices in the superconductor. Since the magnetization of the LCMO is mainly oriented in-plane, these vortices are expected to sit only at the domain walls which are separating domains with differently oriented in-plane magnetization. Only along the domain walls components of out-of-plane magnetization is expected to exist. This creates a flux line distribution similar to that of a grain boundary. This explains the similar behavior found in films with granular microstructure and the bilayer which can be described as containing a magnetic granularity.

The APBs in the single layer could be described as tunneling junctions with reduced order parameter. By the addition of the ferromagnetic layer this model could be further approved. The current flowing across the APBs could be described as a current that needs to cross regions with reduced superconductivity separating highly superconducting islands. The APBs are modeled as being built up of superconducting and nonsuperconducting regions. This results in complex tunneling junctions which can locally be described as Josephson junctions or SQUID-like structures. This description combines the simultaneously observed tunneling characteristic and high critical currents found in measurements.

In conclusion, in this work the following important results have been found. The critical current density of thin YBCO films is governed by the flux-line properties. Three temperature regimes with different current limiting mechanisms were identified. The defect structure of the superconducting film plays an important role for temperatures from 15 K to 40 K. In superconductor/ferromagnet bilayers the ferromagnet affects the critical current by a suppression of T_c and by creation of vortices at positions which are normally not occupied.

The detailed analysis of the local critical currents in YBCO thin films and heterostructures shows that it is possible to control the current carrying properties through the modification of the interfaces. The close connection between microstructure, interfaces and critical currents was proved for YBCO thin films. By a purposeful choice of substrate it is possible to manipulate the microstructure of the superconducting film towards enhancement of critical currents. Further the addition of a ferromagnetic layer shows the possibility of external control of the critical current density in films through the application of external magnetic fields. These results represent an important contribution to the understanding of the mechanisms controlling the high critical current densities found in HTSC films. It is an important step for a controlled application of these materials in sophisticated devices.

Bibliography

[1] H. Kammerlingh-Onnes. *Leiden Comm.*, 120b, 1911.

[2] G. Blatter, M.V. Feigelman, V.B. Geshkenbein, A.I. Larkin, and V.M. Vinkour. *Rev. Mod. Phys.*, 66:1125, 1994.

[3] A. Steppke, C. Becker, V. Grosse, L. Dörrer, F. Schmidl, P. Seidel, M. Djupmyr, and J. Albrecht. *Appl. Phys. Lett.*, 92:122504, 2008.

[4] M.P. Ross and B. Kehrli. Secure super grid: A new solution for secure power in critical urban centers. *Transmission and Distribution Conference and Exposition, 2008. T&D. IEEE/PES*, pages 1–7, 2008.

[5] K. M. Wu, J. R. Ashburn, C. J. Torng, P. H. Hor, C. Meng, L. Gao, Z. H. Huang, Y. Q. Wang, and C. W. Chu. *Phys. Rev. Lett.*, 58:908, 1987.

[6] B. Dam, J.M. Huijbregtse, F.C. Klaassen, R.C.F. van der Geest, G. Doornbos, J.H. Rector, A.M. Testa, S. Freisem, J.C. Martinez, B. Stäuble-Pümpin, and R. Griessen. *Nature (London)*, 399:439, 1999.

[7] J. L. MacManus-Driscoll, S. R. Foltyn, Q. X. Jia, H. Wang, A. Serquis, L. Civale, B. Maiorov, M. E. Hawley, M. P. Maley, and D. E. Peterson. *Nat. Mater.*, 3:439, 2004.

[8] Ch. Jooss, J. Albrecht, H. Kuhn, S. Leonhardt, and H. Kronmüller. *Rep. Prog. Phys.*, 65:651, 2002.

[9] C.H. Lowndes, D.K. Christen, C.E. Klabunde, Z.L. Wang, D.M. Kroeger, J.D. Budai, S. Zhu, and D.P. Norton. *Phys. Rev. Lett.*, 73:2355, 1995.

[10] W. Meissner and W. Ochsenfeld. *Naturwissenschaft*, 21:787, 1933.

[11] F. London and H. London. *Z. Phys.*, 96:359, 1935.

[12] V. Ginzburg and L. Landau. *Zh. Eksp. Teor. Fiz.*, 20:1064, 1950.

[13] J. Bardeen, L.N. Cooper, and J.R. Schrieffer. *Phys. Rev.*, 1064:162, 1957.

[14] J. Bardeen, L.N. Cooper, and J.R. Schrieffer. *Phys. Rev.*, 108:1175, 1957.

[15] H. Fröhlich. *Phys. Rev.*, 79:845, 1950.

[16] J. G. Bednorz and K. A. Müller. *Z. Phys. B*, 64:189, 1986.

[17] U. Zimmermann, S. Abens, D. Dikin, K. Keck, and T. Wolf. *Z. Phys. B*, 101:547, 1996.

[18] T. Egami, J.-H. Chung, R.J. McQueeney, M. Yethiraj, H.A. Mook, C. Frost, Y. Petrov, F. Dogan, Y. Inamura, M. Arai, S. Tajima, and Y. Endoh. *Physica B*, 316-317:62, 2002.

[19] A.S. Alexandrov and P.E. Kornilovitch. *J. Supercond.*, 15:927, 2002.

[20] S.C. Zhang. *Science*, 275:1089, 1997.

[21] H. Hilgenkamp and J. Mannhart. *Rev. Mod. Phys.*, 74:485, 2002.

[22] D. J. Van Harlingen. *Rev. Mod. Phys.*, 67:515, 1995.

[23] C.C. Tsuei and J.R. Kirtley. *Rev. Mod. Phys.*, 72:969, 2000.

[24] D.A. Wollmann, D.J. Van Harlingen, W.C. Lee, D.M. Ginsberg, and A.J. Leggert. *Phys. Rev. Lett.*, 71:2134, 1993.

[25] C.C. Tsuei and J.R. Kirtley. *Physica C*, 282-287:4, 1997.

[26] K.A. Müller. *Physica C*, 387:57, 2003.

[27] L.V. Shubnikov, V.I. Khotkenich, and Yu.D. Shepelev. *Zh. Eksp. Teor. Fiz.*, 7:787, 1933.

[28] U. Essmann and H. Träuble. *Phys. Lett. A*, 24:526, 1966.

[29] A.A. Abrikosov. *Zh. Eksp. Teor. Fiz.*, 52:1442, 1957.

[30] J.R. Clem. *Low. Temp. Phys.*, 18:427, 1975.

[31] H. Douwes and P. Kes. *Cryogenics*, 55:486, 1993.

[32] A. Díaz, L. Mechin, P. Berghuis, and J. E. Evetts. *Phys. Rev. Lett.*, 80:3855, 1998.

[33] H. Safar, J. Y. Coulter, M. P. Maley, S. Foltyn, P. Arendt, X. D. Wu, and J. O. Willis. *Phys. Rev. B*, 52:R9875, 1995.

[34] H. Kronmüller and R. Schmucker. *Phys. Stat. Sol. (b)*, 57:667, 1973.

[35] R. Labusch. *Phys. Rev.*, 170:470, 1968.

[36] I. A. Larkin and Y. N. Ovchinnikov. *Zh. Eksp. Teor. Fiz.*, 65:1704, 1973.

[37] I. A. Larkin and Y. N. Ovchinnikov. *J. Low. Temp. Phys.*, 73:109, 1979.

[38] T. Schuster, H. Kuhn, M. Indenbom, M. Leghissa, M. Kraus, and M. Konczykowski. *Phys. Rev. B*, 51:16358, 1995.

[39] R. Schmucker and H. Kronmüller. *Phys. Stat. Sol.*, 61:181, 1974.

[40] B.D. Josephson. *Phys. Lett.*, 1:251, 1962.

[41] V. Ambegaokar and A. Baratoff. *Phys. Rev. Lett.*, 10:486, 1963.

[42] K.K. Likharev. *Rev. Mod. Phys.*, 51:101, 1979.

[43] P.N. Mikheenko and Y.E. Kuzovlev. *Physica C*, 204:229, 1993.

[44] E.H. Brandt, M.V. Idenbom, and A. Forkl. *Europhys. Lett.*, 22:735, 1993.

[45] C.P. Bean and J.B. Livingstone. *Phys. Rev. Lett.*, 12:14, 1964.

[46] H.F. Hess, R.B. Robinson, R.C. Dynes, J.M. Valles jr., and J.V. Waszack. *Phys. Rev. Lett.*, 62:314, 1988.

[47] E.H. Brandt. *Phys. Rev. B*, 46:8628, 1992.

[48] L. Progozhin. *J. Comp. Phys.*, 144:180, 1998.

[49] Th. Schuster, M.V. Indenbom, M.R. Koblischka, H. Kuhn, and H. Kronmüller. *Phys. Rev. B*, 49:3443, 1994.

[50] A. Forkl and H. Kronmüller. *Phys. Rev. B*, 52:16130, 1995.

[51] J. Pearl. *App. Phys. Lett.*, 5:65, 1964.

[52] R.J. Cava, A.W. Hewat, B.Batlogg, M. Marezio, K.M. Rabe, J.J. Krajewski, W.W. Peck jr., and L.W. Rupp jr. *Physica C*, 165:419, 1990.

[53] A.G. Khachaturyan and J.W. Morris. *Phys. Rev. Lett.*, 64:76, 1990.

[54] P.H. Kes, J. Aarts, V.M. Vinokur, and C.J. van der Beek. *Phys. Rev. Lett.*, 64:1063, 1990.

[55] R. Kleiner, F. Steinmeyer, G. Kunkel, and P. Müller. *Phys. Rev. Lett.*, 68:2394, 1992.

[56] A. Goyal, D. P. Norton, J. D. Budai, M. Paranthaman, E. D. Specht, D. M. Kroeger, D. K. Christen, Q. He, B. Saffian, F. A. List, D. F. Lee, P. M. Martin, C. E. Klabunde, E. Hartfield, and V. K. Sikka. *Appl. Phys. Lett.*, 69:1795, 1996.

[57] R. Wördenweber. *Supercond. Sci. Technol.*, 12:R86, 1999.

[58] T. Araki and I. Hirabayashi. *Supercond. Sci. Technol.*, 16:R71, 2003.

[59] D. Shi, Y. Shu, S.X. Wang, J. Lian, L.M. Wang, S.M. McClellan, R. Buchanan, and K.C. Goretta. *Physica C*, 371:97, 2002.

[60] T. Venkatesan, X.D. Wu, A. Inam, and J.B. Wachtmann. *Appl. Phys. Lett.*, 52:1193, 1988.

[61] H.-U. Habermeier. *Eur. J. Solid State Inorg. Chem.*, 28:619, 1991.

[62] R. Borman and J. Nölting. *J. Appl. Lett.*, 54:2148, 1989.

[63] M. Schieber. *J. Crystal Growth*, 109:401, 1991.

[64] F.C. Frank and J.H. van der Merwe. *Proc. Roy. Soc. London A*, 198:205, 1949.

[65] M.G. Norton and C.B. Carter. *from Interfaces in High-T_c Superconducting Systems, Springer*, 1993.

[66] X.W. Zheng, C.H Lowndes, S. Zhu, J.D. Budai, and R.J. Warmack. *Phys. Rev. B*, 45:7584, 1992.

[67] R.D. Lang, R. Sum, H. Haefke, and H.J. Günterodt. *J. All. Comp.*, 195:97, 1993.

[68] G.H. Gilmer, H. Huang, and Ch. Roland. *Comp. Mat. Sci.*, 12:354, 1998.

[69] I.D. Raistrick and M. Hawley. *from Interfaces in High-T$_c$ Superconducting Systems, Springer*, 1993.

[70] J. Mannhart, D. Anselmetti, J.G. Bednorz, A. Cantana, C. Gerber, K.A. Müller, and D.G. Schlom. *Z. Phys. B*, 86:177, 1992.

[71] H. Douwes, P. Kes, C. Gerber, and J. Mannhart. *J. All. Comp.*, 195:451, 1993.

[72] C. Rossel, A. Cantana, R.R. Schulz, E.J. Williams, A. Perrin, M. Guilloux-Viry, and C. Thivet. *Physica C*, 223:370, 1994.

[73] V.M. Pan. *J. All. Comp.*, 195:387, 1993.

[74] T. Haage, J. Zegenhagen, J. Q. Li, H.-U. Habermeier, M. Cardona, Ch. Jooss, R. Warthmann, A. Forkl, and H. Kronmüller. *Phys. Rev. B*, 56:8404, 1997.

[75] J.Y. Laval and W. Swiatnicki. *Physica C*, 221:11, 1994.

[76] J. Albrecht, Ch. Jooss, R. Warthmann, A. Forkl, and H. Kronmüller. *Phys. Rev. B*, 57:10332, 1998.

[77] D. Dimos, P. Chaudhari, J. Mannhart, and F. K. LeGoues. *Phys. Rev. Lett.*, 61:219, 1988.

[78] S.E. Babcock and J.L. Vargas. *Annu. Rev. Mater. Sci.*, 25:193, 1995.

[79] T. Haage, J.Q. Li, B. Leibold, M.Cardona, J. Zegenhagen, H.-U. Habermeier, A. Forkl, Ch. Jooss, R. Warthmann, and H. Kronmüller. *Solid State Commun.*, 99:553, 1996.

[80] F. Wellhöfer, P. Woodall, D.J. Norris, S. Johnson, D. Vassiloyannis, M. Aindow, M. Slaski, and C.M. Muirhead. *Appl. Surf. Sci.*, 127-129:525, 1998.

[81] J. Zegenhagen, T. Siegrist, E. Fontes, L.E. Berman, and J.R. Patel. *Solid State Comm.*, 99:763, 1995.

[82] Ch. Jooss, R. Warthmann, and H. Kronmüller. *Phys. Rev. B*, 61:12433, 2000.

[83] J.H. Durrell, G. Burnell, V.N. Tsaneva, Z.H. Barber, M.G. Blamire, and J.E. Evetts. *Phys. Rev. B*, 70:214508, 2004.

[84] C.A.R. Sá de Melo. *Phys. Rev. Lett.*, 79:1933, 1997.

[85] Z. Sefrioui, V. Peña, J. E. Villegas, M. Varela, P. Prieto, C. León, J. L. Matrinez, and J. Santamaria. *Phys. Rev. B*, 67:214511, 2003.

[86] S. Soltan, J. Albrecht, and H.-U. Habermeier. *Phys. Rev. B*, 70:144517, 2004.

[87] W. Prellier, Ph. Lecoeour, and B. Mercey. *J. Phys.: Condens. Matter*, 13:R915, 2001.

[88] R. von Helmolt, J. Wecker, B. Holzapfel, L. Schultz, and K. Samwer. *Phys. Rev. Lett.*, 71:2331, 1993.

[89] T. Venkatesan and R.P. Sharma. *Mater. Sci. Eng. B*, 41:30, 1996.

[90] T. Venkatesan, R. P. Sharma, Y. G. Zhao, Z. Y. Chen, C. H. Lee, W. L. Cao, J. J. Li, H. D. Drew, S. B. Ogale, R. Ramesh, M. Rajeswari, T. Wu, I. Jin, S. Choopun, M. Johnson, W. K. Chu, and G. Baskaran. *Mater. Sci. Eng. B*, 63:36, 1999.

[91] S.-W. Cheong and H.Y. Hwang. Ferromagnetism vs charge/orbital ordering in mixed-valent manganites. *Colossal Magnetoresistance Oxides, Editor: Y. Tokura, Gordon and Breach, Monographs in Condensed Matter Science, London*, 2000.

[92] C. Kwon, M. C. Robson, K. C. Kim, J. Y. Gu, S. E. Lofland, S. M. Bhagat, Z. Trajanovic, M. Rajeswari, T. Venkatesan, A. R. Kratz, R. D. Gomez, and R. Ramesh. *J. Magn. Magn. Mater.*, 172:229, 1997.

[93] A. M. Haghiri-Gosnet, J. Wolfman, B. Mercey, Ch. Simon, P. Lecoeur, M. Korzenski, M. Hervieu, R. Desfeux, and G. Baldinozzi. *J. Appl. Phys.*, 88:4257, 2000.

[94] M. Liebmann, U. Kaiser, A. Schwarz, R. Wiesendanger, U. H. Pi, T. W. Noh, Z. G. Khim, and D.-W. Kim. *J. Appl. Phys.*, 93:8319, 2003.

[95] Q. Lu, C.-C. Chen, and A. de Lozanne. *Science.*, 276:2006, 1997.

[96] Z.-H. Wang, G. Cristiani, and H.-U. Habermeier. *Appl. Phys. Lett.*, 82:3731, 2003.

[97] S. Chikazumi. Physics of ferromagnetism. 1997.

[98]   N. F. Mott. *Adv. Phys.*, 13:325, 1964.

[99]   I.I. Mazin. *Phys. Rev. Lett.*, 83:1427, 1999.

[100] H.-U. Habermeier, G. Cristiani, R.K. Kremer, O. Lebedev, and G. Van Tendeloo. *Physica C*, 364-365:298, 2001.

[101] Soltan Soltan. Interaction of superconductivity and ferromagnetism in ybco/lcmo heterostructures, universität stuttgart, http://elib.uni-stuttgart.de/opus/volltexte/2005/2194/. *Dissertation*, 2005.

[102] R. A. Chakalov, G. Passerieux, I. P. Jones, P. Mikheenko, J. Ireland, R. I. Chakalova, M. S. Colclough, and C. M. Muirhead. *J. Appl. Phys.*, 98:123908, 2005.

[103] S.J. Pennycook Z. Sefrioui J. Santamaria M. Varela, A.R. Lupini. *Solid-State Electron.*, 47, 2003.

[104] J. Chakhalian, J. W. Freeland, G. Srajer, J. Strempfer, G. Khaliullin, J. C. Cezar, T. Charlton, R. Dalgliesh, C. Bernhard, G. Cristiani, H.-U. Habermeier, and B. Keimer. *Nat. Phys.*, 47:2245, 2006.

[105] H.-U. Habermeier, S. Soltan, and J. Albrecht. *Physica C*, 460:32, 2007.

[106] J. Albrecht, M. Djupmyr, S. Soltan, H.-U. Habermeier, M.R. Connolly, and S.J. Bending. *New J. Phys.*, 9:379, 2007.

[107] Y. Jaccard, J. I. Martín, M.-C. Cyrille, M. Vélez, J. L. Vicent, and Ivan K. Schuller. *Phys. Rev. B*, 58:8232, 1998.

[108] M. J. Van Bael, K. Temst, V. V. Moshchalkov, and Y. Bruynseraede. *Phys. Rev. B*, 59:14674, 1999.

[109] S. J. Bending, G. D. Howells, A. N. Grigorenko, M. J. Van Bael, J. Bekaert, K. Temst, L. Van Look, V. V. Moshchalkov, Y. Bruynseraede, G. Borghs, and R. G. Humphreysr. *Physica C*, 332:20, 2000.

[110] M. Lange, M. J. Van Bael, V. V. Moshchalkov, and Y. Bruynseraede. *Appl. Phys. Lett.*, 81:322, 2002.

[111] J. Albrecht, S. Soltan, and H.-U. Habermeier. *Europhys. Lett.*, 63:881, 2003.

[112] J. Albrecht, S. Soltan, and H.-U. Habermeier. *Phys. Rev. B*, 72:092502, 2005.

[113] D. V. Shantsev, M. R. Koblischka, Y. M. Galperin, T. H. Johansen, L. Půst, and M.Jirsa. *Phys. Rev. Lett.*, 82:2947, 1999.

[114] Yu.N. Proshin and M.G. Khusainov. *JETP*, 86:930, 1998.

[115] Yu.A. Izyumov, Yu.N. Proshin, and M.G. Khusainov. *Phys. Usp.*, 45:109, 2002.

[116] M. Quijada, J. Černe, J. R. Simpson, H. D. Drew, K. H. Ahn, A. J. Millis, R. Shreekala, R. Ramesh, M. Rajeswari, and T. Venkatesan. *Phys. Rev. B*, 58:16093, 1998.

[117] F. S. Bergeret and N. Garcia. *Phys. Rev. B*, 70:052507, 2004.

[118] K.E. Gray. Nonequilibrium superconductivity, phonons and kapitza boundaries, edited by k.e. gray, plenum, new york. 1981.

[119] P.B. Alers. *Phys. Rev.*, 105:104, 1957.

[120] W. De Sorbo. *Phys. Rev. Lett.*, 4:406, 1960.

[121] Ch. Jooss, R. Warthmann, A. Forkl, and H. Kronmüller. *Physica C*, 299:215, 1998.

[122] T. Schuster, M.R. Koblischka, B. Ludescher, N. Moser, and H. Kronmüller. *Cryogenics*, 31:811, 1991.

[123] L.A. Dorosinskii, M.V. Indenbom, V.I. Nikitenko, Yu.A. Ossip'yan, A.A. Polyanskii, and V.K. Vlasko-Vlasov. *Physica C*, 203:149, 1992.

[124] R. Warthmann, J. Albrecht, H. Kronmüller, and Ch. Jooss. *Phys. Rev. B*, 62:15226, 2000.

[125] F. Laviano, D. Botta, A. Chiodoni, R. Gerbaldo, G. Ghigo, L. Gozzelino, S. Zannella, and E. Mezzetti. *Supercond. Sci. Technol.*, 16:71, 2003.

[126] H. Yan, M. M. Abdelhadi, J. A. Jung, B. A. Willemsen, and K. E. Kihlstrom. *Phys. Rev. B*, 72:064522, 2005.

[127] Ch. Jooss, R. Warthmann, H. Kronmüller, T. Haage, H.-U. Habermeier, and J. Zegenhagen. *Phys. Rev. Lett.*, 82:632, 1999.

[128] J. Gutiérrez, A. Llordés, J. Gázquez, M. Gibert, N. Romà, S. Ricart, A. Pomar, F. Sandiumenge, N. Mestres, T. Puig, and X. Obradors. *Nat. Mat.*, 6:367, 2007.

[129] H. Darhmaoui and J. Jung. *Phys. Rev. B*, 53:14621, 1996.

[130] S. Brück and J. Albrecht. *Phys. Rev. B*, 71:174508, 2005.

[131] M. Djupmyr, G. Cristiani, H.-U. Habermeier, and J. Albrecht. *Phys. Rev. B*, 72:220507(R), 2005.

[132] J. Mannhart, P. Chaudhari, D. Dimos, C. C. Tsuei, and T. R. McGuire. *Phys. Rev. Lett.*, 61:2476, 1988.

[133] M. Djupmyr and J. Albrecht. *Physica C*, 460-462:1190, 2007.

[134] T. Schuster, M.R. Koblischka, H. Kuhn, B. Ludescher, M. Leghissa, M. Lippert, and H. Kronmüller. *Physica C*, 196:373, 1992.

[135] A. Gurevich and M. Friesen. *Phys. Rev. B*, 62:4004, 2000.

[136] K. Matsumoto, T. Horide, K. Osamura, M. Mukaida, Y. Yoshida, A. Ichinose, and S. Horii. *Physica C*, 412-414:1267, 2004.

[137] T. Aytug. *J. Appl. Phys.*, 98:114309, 2005.

[138] A. N. Grigorenko, S.J. Bending, G. D. Howells, and R. G. Humphreys. *Phys. Rev. B*, 62:721, 2000.

[139] B. Roas, B. Hensel, G. Endres, L. Schultz, and G. Saemann-Ischenko. *Thin Solid Films.*, 174:179, 1989.

[140] L. Civale. *Supercond. Sci. Technol.*, 10:A11, 1997.

[141] C. Cai, B. Holzapfel, J. Hänisch, L. Fernández, and L. Schultz. *Phys. Rev. B*, 69:104531, 2004.

[142] J. Hänisch, C. Cai, R. Hühne, L. Schultz, and B. Holzapfel. *Appl. Phys. Lett.*, 86:122508, 2005.

[143] S. Engel, T. Thersleff, R. Hühne, L. Schultz, B. Holzapfel, S. Engel, T. Thersleff, L. Schultz, B. Holzapfel, and L. Schultz. *Appl. Phys. Lett.*, 90:102505, 2007.

[144] A. A. Gapud, D. Kumar, S. K. Viswanathan, C. Cantoni, M. Varela, J. Abiade, S. J. Pennycook, and D. K. Christen. *Supercond. Sci. Technolo.*, 18:1502, 2007.

[145] C. Cai, B. Holzapfel, J. Hänisch, and L. Schultz. *Phys. Rev. B*, 70:212501, 2004.

[146] M. Djupmyr, S. Soltan, H.-U. Habermeier, and J. Albrecht. *Submitted to Phys. Rev. B*, 2009.

[147] P.W. Anderson and Y.B. Kim. *Rev. Mod. Phys.*, 36:39, 1964.

[148] E.H. Brandt. *Rep. Prog. Phys.*, 58:1465, 1995.

[149] V. Pan, Y. Cherpak, V. Komashko, S. Pozigun, C. Tretiatchenko, A. Semenov, E. Pashitskii, and A.V. Pan. *Phys. Rev. B*, 73:054508, 2006.

[150] H.H. Wen, H.G. Schnack, R. Griessen, B. Dam, and J. Rector. *Physica C*, 241:353, 1995.

[151] Y. Yeshurun, A. P. Malozemoff, and A. Shaulov. *Rev. Mod. Phys.*, 68:911, 1996.

[152] J. Albrecht, M. Djupmyr, and S. Brück. *J. Phys.: Condens. Matter*, 19:216211, 2007.

[153] J. Albrecht, S. Leonhardt, and H. Kronmüller. *Phys. Rev. B*, 63:014507, 2001.

[154] A. A. Polyanskii, A. Gurevich, A. E. Pashitski, N. F. Heinig, R. D. Redwing, J. E. Nordman, and D. C. Larbalestier. *Phys. Rev. B*, 53:8687, 1996.

[155] A. Gurevich. *Phys. Rev. B*, 46:3187, 1992.

[156] A. Gurevich. *Phys. Rev. B*, 65:214531, 2002.

[157] T. Horide, K. Matsumoto, Y. Yoshida, M. Mukaida, A. Ichinose, and S. Horii. *Phys. Rev. B*, 77:132502, 2008.

[158] A. Gurevich. *Phys. Rev. B*, 48:12857, 1993.

[159] J. Albrecht. *NATO Science Series II*, 142:159–165, 2004.

[160] J. Albrecht. private communications. 2008.

[161] G. Deutscher and K.A. Müller. *Phys. Rev. Lett.*, 59:1745, 1987.

[162] G. Deutscher. *IBM J. Res. Dev.*, 33:293, 1989.

[163] P. Bernstein, Y. Bougherira, J.F. Hamet, Y. Thimont, and L. Me´chin. *Phys. Rev. B*, 78:0545171, 2008.

Acknowledgment

My deepest gratitude to the people who have over the years in various ways contributed to the success of this work.

I want to thank Prof. Dr. Gisela Schütz, for welcoming me in her department and thus making it possible for me to carry out this work. Further I want to thank Prof. Dr. Fritz Aldinger for reviewing this thesis.

More than anyone I would like to thank my supervisor Prof. Dr. Joachim Albrecht for all his help, support, encouragement and close collaboration.

I would also like to thank my present and former colleges in department Schütz, especially mentioning Sebastian Macke, Sebastian Treiber, Philipp Rudo and Patrick Audehm. Gratitude to Dr. Brigitte Baretzky for her support and huge help in solving practical problems.

Much appreciation to Georg Christiani who has provided me with the best samples I could wish for. Gratitude to Prof. Dr. Hanns-Ulrich Habermeier and Dr. Soltan Soltan for the close collaboration, and thanks to other members of the technology group.

Deepest thanks to Max Planck Research School for the funding and to Dr. Hans-Georg Libuda for his support.

Special thanks to Christoph Schlegel my close friend who also helped me a lot in the final writing process of this thesis.

I also would like to thank my family, Roman for his love and support and my dear son Jarek for not arriving too early...

Finally I would like to thank my parents and grand parents from whom I have learnt that everything is possible.

List of Publications

- *Critical Currents in $YBa_2Cu_3O_{7-\delta}/La_{2/3}Ca_{1/3}MnO_3$ hybrid structures*

  M. Djupmyr, S. Soltan, H.-U. Habermeier and J. Albrecht
  submitted to Phys. Rev. B

- *Chaotic vortex dynamics and low current phases in the remanent state of MgB_2 thin films*

  J. Albrecht, P. Audehm, M. Djupmyr
  Supercond. Sci. Techn. **21**, 045016 (2008)

- *Planar high-T_c superconducting quantum interference device gradiometer for simultaneous measurements of two magnetic field gradients*

  A. Steppke, C. Becker, V. Grosse, L. Dorrer, F. Schmidl, P. Seidel, M. Djupmyr, and J. Albrecht
  Appl. Phys. Lett. **92**, 122504 (2008)

- *Substrate-induced current anisotropy in $YBa_2Cu_3O_{7-\delta}$ thin films*

  M. Djupmyr and J. Albrecht
  Physica C **460**, 1190 (2007)

- *Universal temperature scaling of flux line pinning in high-temperature superconducting thin films*

  J. Albrecht, M. Djupmyr and S. Brück
  J. Phys.: Condens. Matter **19**, 216211 (2007)

- *Inhomogeneous vortex distribution and magnetic coupling in oxide superconductor-ferromagnet hybrids*

  J. Albrecht, M. Djupmyr, S. Soltan, H.-U. Habermeier, M. Connolly and S. Bending
  New Journal of Physics **9**, 379 (2007)

- *Anisotropic temperature-dependent current densities in vicinal $YBa_2Cu_3O_{7-\delta}$*
  M. Djupmyr, G. Cristiani, H.-U. Habermeier and J. Albrecht
  Phys. Rev. B **72**, 220507 (2005)

- *Bending of magnetic avalanches in MgB_2 thin films*
  J. Albrecht, A. T. Matveev, M. Djupmyr, G. Schütz, B. Stuhlhofer and
  H.-U. Habermeier
  Appl. Phys. Lett. **87**, 182501 (2005)

Curriculum Vitae

Märit Djupmyr

Date of birth: 24th of April, 1979
Place of birth: Föllinge, Sweden

Education

Since 01/2005 Member of the International Max Planck Research School for Advanced Materials, IMPRS

Ph.D. student at the Max-Planck-Institute for Metal Research in Stuttgart, department of Prof. G. Schütz.

Project title: *The role of temperature for the critical current density in high-temperature superconductors and hetero-stuctures*;

09/1998–06/2004 Studies in Physics at the Royal Institute of Technology, KTH, Stockholm, Sweden

Civilingenjörsexamen 180 poäng inom Teknisk Fysik
Master of Science in Engineering, Degree Programme in Engineering Physics, 4.5 years fulltime studies

Specialization: Solid state physics

Thesis: *Scaling of the B-dependent resistivity for different orientations in $YBa_2Cu_3O_{7-\delta}$*;

10/2000–04/2002 Studies in Physics at RWTH, Aachen

Focus: Condensed matter theory